学位論文

Measurement of the Neutron Lifetime by Counting the Beta Decay at J-PARC

(J-PARCにおけるベータ崩壊の計数による中性子寿命の測定)

平成29年12月博士（理学）申請

東京大学大学院理学系研究科
物理学専攻

家城 斉

Measurement of the Neutron Lifetime by Counting the Beta Decay at J-PARC

Ph.D dissertation

Sei Ieki

Department of Physics,
School of Science, The University of Tokyo
7-3-1, Hongo, Bunkyo-ku, 113-0033, Tokyo, Japan

December, 2017

Abstract

The neutron decays into the proton, the electron and the neutrino with lifetime of about 15 minutes. The neutron decay is simple picture of semi-leptonic process mediating W boson and the neutron lifetime is studied as a tool to probe the theory of weak interaction, cosmology and production of light nuclei in the early universe.

For the precise measurement of the neutron lifetime, key issues arise from statistics and accurate measurement of absolute flux and that of neutron decay. The lifetime experiments are classified into two methods, depend on the way to count neutron decay. In the in-flight method, neutron decay in-flight is counted by detecting the decay products, while the bottle method store neutrons and count the remaining after a certain storage time. There have been recent interests in improving the uncertainty on the neutron lifetime to below 0.1 %, because there are $3.8\,\sigma$ deviation between two methods, although the reported values are consistent within each method.

In order to achieve high precision, we perform the measurement with intense neutron beam at Japan Proton Accelerator Research Complex (J-PARC), Materials and Life Science Experimental Facility (MLF), beamline 05. While most of the lifetime experiments were conducted with reactor based sources, we have an advantage to increase the beam flux based on the high intensity proton beam at J-PARC. A distinguishing feature of our setup is that the source of backgrounds are reduced by material selection of the time projection chamber (TPC). The neutron beam is formed into bunches by originally developed spin flip chopper, that also contribute to improve the signal-to-noise ratio. Our experiment is conceptually based on the in-flight method with a He-filled TPC proposed by ILL-ISL-LAPP collaboration [6], which have an advantage to cancel the uncertainties in the different beam flux and neutron velocity since neutron decay and beam flux are measured by the same detector, simultaneously.

We carried out engineering data taking in 2014 and 2015, that correspond to two measurement series with a new gas mixture for each run, and established the procedure of analysis. In 2016, the first physics data set was obtained at 170 kW operation. The neutrons with the velocity range of $500 \sim 1200\,\mathrm{m/s}$ are provided and 6.37×10^4 events of neutron decay have been detected in about 1 m of decay volume. Combined with the engineering data, the accumulated data correspond to 12 days of the beam time, and we present our first result of the neutron lifetime as

$$\tau_n = 899 \pm 10\,(\mathrm{stat.}) \pm^{9}_{11}\,(\mathrm{syst.})\,\mathrm{sec.}$$

Major systematical uncertainties are originated from the process to evaluate the number of neutron decays and detection efficiencies. In this thesis, the investigation of backgrounds and the analytic methods are explained in detail.

Contents

Part I

Neutron lifetime

Chapter 1

Introduction

1.1 Discovery of neutron

In 1932, the neutron is discovered by J. Chardwick [1]. The discovery leads to deeper understanding of nuclear structure and neutron correlated parameters. So far, atomic nuclei were considered as a composition of protons and electrons. In 1930, Walther Bothe and Herbert Becker reported the observation of non-ionizing radiation with strong penetrating power. In Bothe's experiment, ^{9}Be was exposed to α particles from polonium, resulted in the following reaction.

$$^9\text{Be} +^4 \text{He} \rightarrow^{12} \text{C} + n$$

In the previous assumption, the observed electric neutral radiation was considered as a high energy γ ray. However, the energy of the radiation was estimated to be about 50 MeV by Curie-Joliot and M. Joliot and by Webster, that was difficult to account for the interaction of a beryllium nucleus and an α particle.

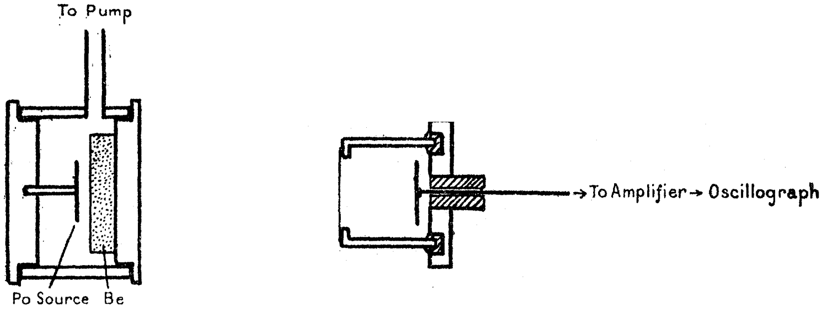

Figure 1.1: Illustration of experimental setup of Chadwick's experiment [1].

The contradictions were resolved by Chadwick. In Chadwick's experiment, beryllium was irradiated by α ray which were emitted from polonium source and mysterious neutral radiations were generated (Fig. 1.1). By putting a target in the path of the radiations, charged particles were recoiled from the target. Then, charged particles were detected via ionization in a gas chamber to reconstruct the velocity. The velocity reached at least $3 \times 10^7\,\mathrm{m/s}$, that could not be explained by γ rays while if the recoil particle is assumed as the proton, it satisfies the conservation law.

The mass of mysterious radiation was also calculated by conducting the measurements with several target materials. The estimated value was 1.0081 u and that was very close to the proton mass. Combined with its penetrating power, the mysterious radiation must be neutral and it was concluded as a new particle, the neutron.

1.2 Neutron lifetime physics

Some motivations arise to measure the neutron lifetime since it has important implications in particle physics and in cosmology.

- Big Bang nucleosynthesis
- CKM matrix unitarity
- Solar burning

Dominant decay mode of neutron is

$$n \to p + e^- + \bar{\nu_e} + 782\,\mathrm{keV}. \tag{1.1}$$

Neutron decay relates to parameters such as the mass difference between neutron and

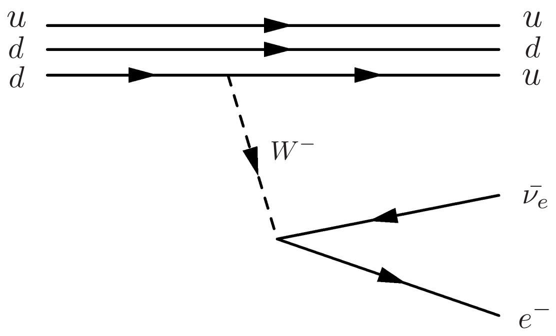

Figure 1.2: Dominant decay mode of neutron.

proton. They differ only 1293 keV, result in about 15 minutes of long lifetime of neutron. The energy of neutron is mainly shared with the electron and the antineutrino, where the end point of electron is 782 keV and the energy of proton is only 0.75 keV at maximum.

On the other hand, radiative beta decay and two-body decay are known as the other decay modes of the neutron [3, 15].

$$n \;\rightarrow\; p + e^- + \bar{\nu}_e + \gamma \quad (BR \sim 3 \times 10^{-3}) \tag{1.2}$$
$$n \;\rightarrow\; H^o + \bar{\nu}_e \quad (BR \sim 4 \times 10^{-6}) \tag{1.3}$$

They have little contribution to neutron lifetime measurements because of the small branching ratio. In this thesis, the uncertainty derived from these decay are not taken into consideration.

1.2.1 Probablity of neutron decay

As the neutrino is included into the theory, the neutron decay is explained by Enrico Fermi in 1934. It successfully demonstrates the probability of transition and that is now referred to as Fermi's Golden Rule. The neutron lifetime is equal to the inverse of the probability of transition.

$$\begin{aligned} W = \tau_n^{-1} &= \frac{2\pi}{\hbar}|\mathcal{M}_{if}|^2\rho_f \\ &= \frac{2\pi}{\hbar}g^2|\langle\psi_f|H|\psi_i\rangle|^2\rho_f, \end{aligned} \tag{1.4}$$

where W is the transition probability, $\mathcal{M}_{if}$ is matrix element for the interaction, g is strength of coupling and ρ_f is density of final states. The final state wavefunctions are given as follows:

$$\begin{cases} \psi_e(r) = \frac{1}{\sqrt{V}}e^{-ip_e\cdot r/\hbar} \\ \psi_\nu(r) = \frac{1}{\sqrt{V}}e^{-ip_\nu\cdot r/\hbar} \end{cases},$$

it is assumed that $\psi_e(r=0) = \psi_\nu(r=0) = \frac{1}{\sqrt{V}}$. Then, Eq. (1.4) is modified with

$$\tau_n^{-1} = \frac{2\pi}{\hbar}\frac{g^2}{V^2}|M_{if}|^2\rho_f. \tag{1.5}$$

To focus on the density states, it is proportional to the number of unit cells in phase space occupied. We define dN as the number of ways that the total energy can be divided between the electron and the neutrino.

$$dN = \frac{dn_e}{dp_e}\frac{dn_\nu}{dp_\nu} \tag{1.6}$$
$$= \Big(4\pi p_e^2 dp_e \frac{V}{h^3}\Big)\Big(4\pi p_\nu^2 dp_\nu \frac{V}{h^3}\Big). \tag{1.7}$$

According to the conservation law,

$$\begin{aligned} p_\nu &= \frac{E_\nu}{c} = \frac{E_0 - E_e}{c}, && (1.8) \\ \frac{dN}{dE_0} &= \frac{16\pi^2 V^2}{h^6 c^3}(E_0 - E_e)^2 p_e^2 dp_e, && (1.9) \end{aligned}$$

where E_0 is equal to the Q-value. By introducing Fermi function $F(Z_d, p_e)$ which is account for the nuclear coulomb interaction with the emitted particle, ρ_f is given as follows.

$$\begin{aligned} \rho_f &= \frac{V^2}{4\pi^4 \hbar^6 c^3} \int F(Z_d, p_e)(E_0 - E_e)^2 p_e^2 dp_e \\ &= \frac{m_e^5 c^4 V^2}{4\pi^4 \hbar^6} f(Z_d, Q), && (1.10) \end{aligned}$$

here d represents the daughter particle and f is called f function. Finally, Eq. (1.5) is combined with Eq. (1.10), we obtain the probability of transition expressed as the proportional function of vector and axial-vector couplings, g_V and g_A.

$$\begin{aligned} \tau_n^{-1} &= \frac{m_e^5 c^4}{2\pi^3 \hbar^7} g^2 |M_{if}|^2 f(Z_d, Q) && (1.11) \\ &= \frac{g_V^2 + 3g_A^2}{K} f(Z_d, Q), && (1.12) \end{aligned}$$

where K is equal to $2\pi^3\hbar^7/m_e^5 c^4$. When radiative correction and nucleus independent correction are taken into account, one obtains,

$$\tau_n^{-1} = \frac{g_V^2(1 + \Delta_R^V)(1 + 3\lambda^2)}{K} f(1 + \delta_R), \tag{1.13}$$

where λ that is the ratio of g_V to g_A.

Correlation coefficients

The neutron decay is related with some coefficients appear in Eq. (1.14),

$$dW \propto (g_V^2 + 3g_A^2)F(E_e)\Big\{1 + a\frac{\vec{p_e}\cdot\vec{p_\nu}}{E_e E_\nu} + \vec{\sigma_n}\cdot(A\frac{\vec{p_e}}{E_e} + B\frac{\vec{p_\nu}}{E_\nu} + D\frac{\vec{p_e}\times\vec{p_\nu}}{E_e E_\nu})\Big\}. \tag{1.14}$$

- Electron-antineutrino asymmetry:

$$a = \frac{1 - |\lambda|^2}{1 + 3|\lambda|^2}.$$

- Spin-electron asymmetry:

$$A = -2\frac{|\lambda|^2 + |\lambda|\cos\phi}{1+3|\lambda|^2}.$$

- Spin-antineutrino asymmetry:

$$B = -2\frac{|\lambda|^2 - |\lambda|\cos\phi}{1+3|\lambda|^2}.$$

- Triple correlation:

$$D = 2\frac{|\lambda|\sin\phi}{1+3|\lambda|^2}.$$

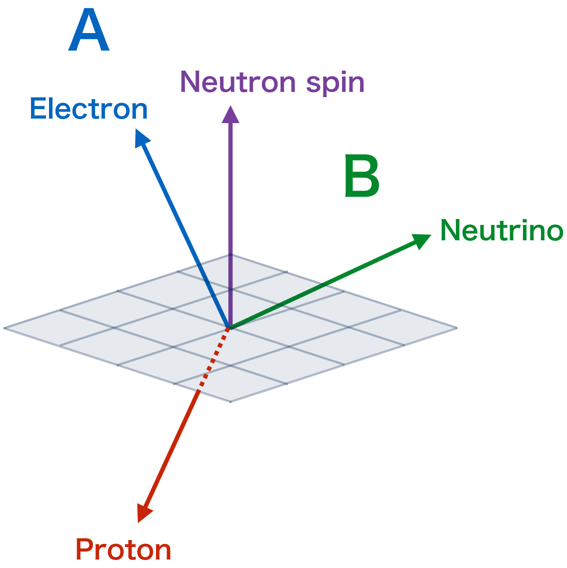

Figure 1.3: Drawing of the neutron decay correlation coefficients.

1.2.2 Big Bang nucleosynthesis

A motivation to improve the precision of the neutron lifetime is that it is one of important input parameters for Big Bang nucleosynthesis (BBN). BBN theory describes the formation of light elements, and the uncertainty of the prediction is limited by the precision of neutron lifetime. After 1 sec of the Big Ban, the universe expands and cools down. Depending on the temperature variation, the thermodynamics condition which decides the ratio of the number of neutrons to that of protons is changed. Because the reaction rates are expressed as the function of neutron abundance, the neutron lifetime determines primordial ^{4}He abundance. The time after the Big Ban is roughly divided according to the temperature, as follows.

1. Thermal equilibrium ($T > 1\,\mathrm{MeV}$)
   In the high temperature universe, the expansion rate superior to cooling, and following thermal equilibrium are satisfied.

   - $p + e^- \leftrightarrow n + \nu$
   - $n + e^+ \leftrightarrow p + \nu$
   - $n \leftrightarrow p + e^- + \bar{\nu}$

   The n/p ratio is given as Boltzmann distribution.

   $$n/p = e^{-\Delta m/k_B T},$$

   here Δm is the mass difference between the neutron and the proton, k_B is the Boltzmann constant and T is temperature. The n/p ratio is estimated to be 1/6.

2. Freeze-out ($T \sim 0.1\,\mathrm{MeV}$)
   The thermal equilibrium is no longer hold when the Hubble expansion rate exceed the weak reaction rate. The n/p ratio is fixed before the freeze-out and it is reduced to 1/7 due to neutron decay. The temperature of freeze-out T_F depends on the neutron lifetime, for example, if the neutron has longer lifetime, the freeze-out would occur at higher temperature and it also affects the equilibrium of the n/p ratio.

3. Nucleosynthesis ($T < 0.1\,\mathrm{MeV}$)
   As the number of photons are reduced, it allows to proceed the exothermic reactions as below, then deutron and ^{4}He formations are started.

   - $p + n \rightarrow d + \gamma$
   - $d + n \rightarrow {}^{3}\mathrm{H} + \gamma$
   - ${}^{3}\mathrm{H} + p \rightarrow {}^{4}\mathrm{He} + \gamma$
   - $d + p \rightarrow {}^{3}\mathrm{He} + \gamma$
   - ${}^{3}\mathrm{He} + n \rightarrow {}^{4}\mathrm{He} + \gamma$
   - $d + d \rightarrow {}^{3}\mathrm{He} + n$
   - ${}^{3}\mathrm{He} + d \rightarrow {}^{4}\mathrm{He} + p$
   - $d + d \rightarrow {}^{3}\mathrm{H} + p$
   - ${}^{3}\mathrm{H} + d \rightarrow {}^{4}\mathrm{He} + n$
   - $d + d \rightarrow {}^{4}\mathrm{He} + \gamma$

1.2.3 CKM matrix unitarity

The Cabbibo-Kobayashi-Maskawa (CKM) matrix represents the coupling constant of weak interaction that change one flavor of quark into another.

$$\begin{pmatrix} d' \\ s' \\ b' \end{pmatrix} = \begin{pmatrix} V_{ud} & V_{us} & V_{ub} \\ V_{cd} & V_{cs} & V_{cb} \\ V_{td} & V_{ts} & V_{tb} \end{pmatrix} \begin{pmatrix} d \\ s \\ b \end{pmatrix} \tag{1.15}$$

Previously, the CKM matrix unitarity have been tested by nuclear superallowed beta decays, neutron decay and pion beta decay. Neutron decay have an advantage in the independence of nuclear structure, while it has to be taken into account the contributions from not only vector but also axial-vector. Since V_{ud} and the weak coupling constant from purely leptonic muon decay G_F are connected with $g_V(= G_F V_{ud})$, V_{ud} is derived from Eq. (1.13),

$$V_{ud}^2 = \frac{K}{G_F^2(1+\Delta_R^V)(1+3\lambda^2)f(1+\delta_R)\tau_n}. \tag{1.16}$$

The CKM unitarity can be tested by the conjunction of three matrix elements and the unitarity is established if the condition of Eq. (1.17) is satisfied.

$$V_{ud}^2 + V_{us}^2 + V_{ub}^2 = 1 \tag{1.17}$$

V_{us} is obtained by the measurement of semi-leptonic kaon decays, while V_{ub} has little contribution to the unitarity test because of its small value.

$$|V_{us}| = 0.2196 \pm 0.0023$$
$$|V_{ub}| = 0.0036 \pm 0.0010$$

V_{ud} is responsible for the accuracy of the test, and therefore precise measurement of the neutron lifetime is important. However, currently uncertainty is governed by the precision of Δ_R^V.

The results from three methods are shown in Tab. 1.1. The most precise value is given by nuclear superallowed beta decays and it is consistent with the neutron decay method despite of its large error. When the measurement of supperallowed beta decay is referred to, the unitarity is not satisfied by 2.3 standard deviations. On the other hand, the neutron decay method do not have enough precision to give the conclusion of unitarity. For that reasons, improvement of uncertainties in both experiment and theory are needed.

Method	$\lvert V_{ud}\rvert$	$\Sigma_i V_{ui}^2$
Nuclear	0.9740(5)	0.9968(14)
Neutron decay	0.9745(16)	0.9978(33)
Pion decay	0.9670(16)	0.9833(311)

Table 1.1: Reported values of V_{ud} [14].

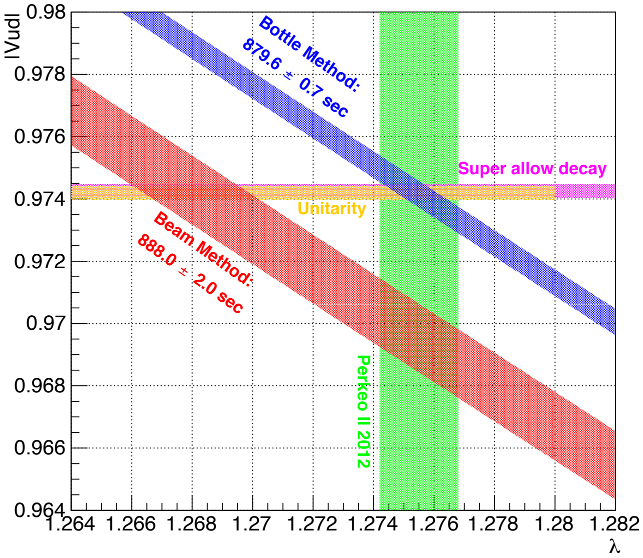

Figure 1.4: V_{ud} vs. λ.

1.3 Previous neutron lifetime experiments

The neutron lifetime is measured by the ratio of neutron flux to number of neutron decay. In order to achieve precise measurement, key issues arise as following.

- High statistics of neutron.
- Precise measurement of the absolute neutron flux.
- Low background condition for counting the neutron decay.

There are two possible directions to count the neutron decay. One is called in-flight method, where neutron decay is identified by detecting the decay products. The in-flight method have an advantage in statistics, but some difficulties arise in the measurement of beam flux and identification of the decay products. The other is bottle method, the neutron lifetime is measured by counting the remaining neutrons which have been stored in a bottle. Signal-to-noise ratio is much preferable in bottle method, while possibilities of non-beta decay losses are pointed out.

We will introduce both methods in the following section, and our experiment is conceptually based on the in-flight method with a He-filled TPC proposed by ILL-ISL-LAPP collaboration [6], that is also explained in the following.

Method	Features	Issues
In-flight	Proton counting	Absolute flux
	Electron counting	High background rate
Bottle	Material bottle	Wall loss and energy spectrum of UCN
	Magnetic trap	Complicated orbits and spin flips

Table 1.2: Methods and issues.

1.3.1 In-flight method

For the measurement of neutron lifetime, beam flux and neutron decay have to be evaluated. The transition of neutron density is given by exponential expression.

$$N(t) = N(0)\ e^{-t/\tau_n}, \tag{1.18}$$

where $N(t)$ is the number of neutron at a certain time t and τ_n is the neutron lifetime. The number of neutron decay N_β is calculated with beam flux ϕ and it is well approximated as the function proportional to t/τ_n because τ_n is much longer than t.

$$N_\beta \sim \frac{\phi\ t}{\tau_n}. \tag{1.19}$$

In the measurement of neutron flux, there are difficulties arise from its electric neutrality. Generally, neutron flux is measured by detecting neutron capture reaction, for example, $^3\mathrm{He}(n,p)^3\mathrm{H}$ reaction is used for on-line counting.

$$N_n = \phi\ e^{-\rho\sigma v_n t} \sim \phi\rho\sigma v_n t, \tag{1.20}$$

where N_n is number of $^3\mathrm{He}(n,p)^3\mathrm{H}$ reactions, ρ is $^3\mathrm{He}$ density, σ is the capture cross section and v_n is the velocity of neutron. The cross section of $^3\mathrm{He}(n,p)^3\mathrm{H}$ reaction with the neutron velocity at 2200 m/s is well known as 5333(7) barn [4]. Since the cross section of capture reaction for slow neutron is proportional to the inverse neutron velocity, σv_n is expected to be constant value.

$$\sigma v_n = \sigma_0 v_0 = const.$$

Including the detection efficiencies ϵ_β and ϵ_n, N_n is divided by N_β to obtain the neutron lifetime,

$$\tau_n = \frac{1}{\rho\sigma_0 v_0}\frac{N_n/\epsilon_n}{N_\beta/\epsilon_\beta}. \tag{1.21}$$

Neutron capture reactions in ^{3}He and ^{10}B are widely used in on-line beam flux measurements, while Au and Co are applied for off-line measurements. Neutron decay measurements have been performed by three kinds of approaches in the previous beam experiments. One is to detect the decay electron and a serious problem arise from high background condition. For the reduction of backgrounds, chopped neutron beam is generally used. The other ways are detection of decay proton, and coincidence measurement of electrons and protons. In these approaches, signal-to-noise ratio is much improved but there are uncertainties originated from separate measurement of beam flux and the neutron decay. In the following, we will focus on two experiments, one detected the decay protons and the other measured the electrons with a He-filled TPC.

Measurement by counting the trapped protons

Precise measurement with a quasi-Penning trap was performed by J. S. Nico *et al.* in 1980 at ILL reactor [18]. The cold neutrons were provided by the research reactor and the decay protons were counted. The setup is shown in Fig. 1.5. There are three steps to detect the decay protons, trapping the protons, counting the protons, and cleaning the trap. Firstly, potential well with depth of 0.8 keV was formed by 4.6 T magnetic field and 16 electrodes. The maximum cyclotron radius of the proton was small enough for the confinement. After the trapping time, decay protons were accelerated toward Si detector and collected. The

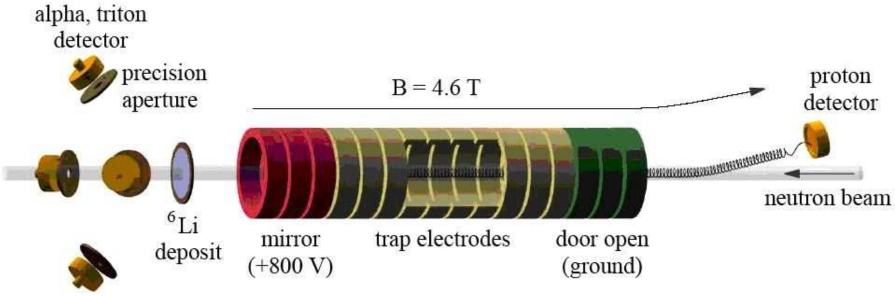

Figure 1.5: Illustration of the quasi-Penning trap and Si detectors [18].

technique of detecting the proton is bit complicated due to low energy of protons which have end point of 0.75 keV, so that acceleration is needed to increase the energy.

The backgrounds condition is favorable to count the neutron decay, however the precision of the measurement was limited by the evaluation of neutron flux. Neutrons were counted by using a target which is surrounded by four Si semiconductor detectors. The reaction products of $^6\text{Li}(n,\alpha)^3\text{H}$ were detected and flux was calculated based on the $1/v$ law. As the result, the neutron lifetime was presented as $\tau_n = 886.6 \pm 1.2\,(\text{stat.}) \pm 3.2\,(\text{syst.})\,\text{sec}$. The systematics errors includes ones derived from neutron counting, beam halo, proton trapping and proton counting. Ones of the most responsible are areal density of ^{6}LiF deposit and the capture cross section of $^6\text{Li}(n,\alpha)^3\text{H}$.

Electron counting measurement with a He-filled TPC

The electron counting experiment was performed by ILL-ISN-LAPP collaboration, which proposed the neutron lifetime measurement with He-filled time projection chamber (TPC) [6]. Characteristic approach in this experiment is that beam flux and neutron decay were measured in the same volume of detector simultaneously.

The experiment was carried out at the research reactor at ILL (H14-PN7) and the setup is illustrated in Fig. 1.6. In the upstream, monochromatic neutron packets were formed by chopper drum and they were delivered to TPC that contained small amount of ^{3}He. Beam flux was determined by counting $^3\text{He}(n,p)^3\text{H}$ reaction. The measured neutron velocity was

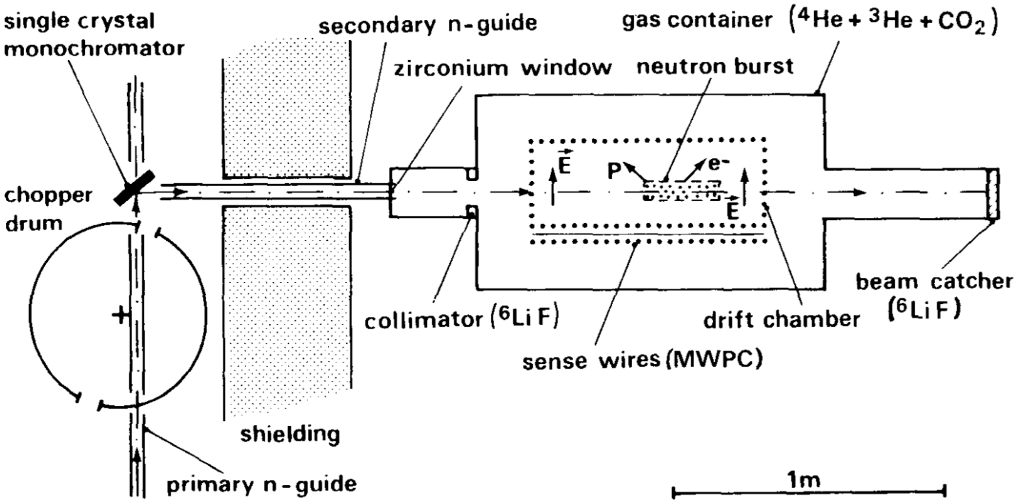

Figure 1.6: Experimental setup of the neutron lifetime experiment by ILL-ISL-LAPP collaboration [6].

837 m/s, that the probability of neutron decay in flight length of 70 cm correspond to order of 10^{-6}. The intensity was 2000 neutrons per packet of 20 cm length and 4 cm^2 cross section. Long track of ionized particles were generated by the decay electrons and the ionized particles drift toward multi wire proportional chamber which enable to detect in a 4π geometry.

The final result is $\tau_n = 878 \pm 27\,(\text{stat.}) \pm 14\,(\text{syst.})\,\text{sec}$. Statistical error dominates the uncertainty because of the shortage of beam time. As for the systematical errors, the significant backgrounds were derived from neutron scattering followed by capture reactions. Although chamber was coated with ^{6}LiF, further suppression of γ rays was necessary. It was also pointed out that major part of backgrounds were originated from point-like ionization events that limited the efficiency of neutron decay. Possible sources of the backgrounds would be the neutron capture reaction in CO_2 gas and the decay electron from ^{3}H that could be provided by $^6\text{Li}(n, \alpha)^3\text{H}$ and $^3\text{He}(n, p)^3\text{H}$.

1.3.2 Bottle method

The other concept of the neutron lifetime measurement is to obtain the exponential decay curve. In the bottle method, techniques to store ultra cold neutron (UCN) in a bottle have been developed and the surviving neutrons are counted. Equation (1.18) can be expressed as following.

$$\tau_n^{-1} = \frac{\ln\left(N(t_1)/N(t_2)\right)}{t_2 - t_1}, \tag{1.22}$$

where $N(t)$ is the number of neutrons in the bottle at a storage time t $(t_1 < t_2)$. There is no need for worry about the efficiency of neutron detector and the neutron loss rate during transportation, because the lifetime in Eq. (1.22) concern only the ratio of the number of neutrons. Besides, recent improvements of storage techniques are remarkable and statistical disadvantage have being overcome.

Important systematical uncertainties are caused by losses of neutrons which are not related to the decay. The measured neutron lifetime τ_m is given by

$$\tau_m^{-1} = \tau_n + \Sigma\ \tau_{loss}^{-1}. \tag{1.23}$$

Therefore, the precision of measurement is determined by the treatment of undesired losses.

Measurement using gravitationally trapped UCN

The most precise neutron lifetime measurement was performed by PNPI group at ILL in Grenoble, France [20]. The distinguishing features of the experiment are that the UCN is gravitationally trapped and the energy spectrum of UCN is measurable. The measurement proceeds as follows. The first process is to fill the UCN into the trap which is illustrated with dashed line in Fig. 1.7. In the filling process, the trap window was set at the down position and UCN is guided from inlet valve (2). During the storage time, trap window was positioned to up, and then rotated to the UCN detector (12) in the counting process. Since the maximum energy of storable UCN is determined by the height of the trap window respect to the bottom of the trap, it can work as a spectrometer.

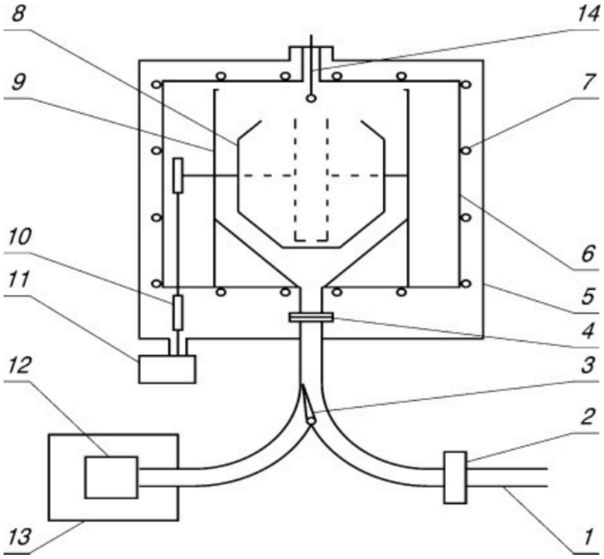

Figure 1.7: Schematic view of the gravitational UCN storage system [20]. 1: input neutron guide, 2: inlet valve, 3: selector valve, 4: aluminum foil, 5: "dirty" vacuum volume, 6: "clean" vacuum volume, 7: cooling coils for the thermal shields, 8: UCN storage trap, 9: cryostat, 10: mechanics for trap rotation, 11: stepping motor, 12: UCN detector, 13: detector shield, and 14: vaporizer.

A problem concerning the uncertainty in the bottle method is neutron losses caused by interactions of wall. In order to achieve an ideally homogeneous surface, the trap surface was coated with a material named perfluoropolyether (PFPE), which is also known as fomblin oil. Because it contains only carbon, oxygen and fluorine, the probability of neutron capture is lowered. PFPE was deposited on the surface by evaporation in vacuum and the uncovered part of the surface was less than 10^{-6}. On the other hand, studies reported that unexpected neutron loss due to quasi-elastic scattering emerged. When neutrons were scattered by the wall, neutrons were escaped from the trap according to the momentum transfer. And also it was investigated that the neutron losses were insignificant under -120 °C and the experiment was performed at -160 °C.

The result of the measurement is $\tau_n = 878.5 \pm 0.7\,(\text{stat.}) \pm 0.3\,(\text{syst.})$ sec. Still statistical error dominates the uncertainty of the measurement, while the probability of neutron losses from the trap accounted for only 1 % of the probability of neutron decay. In detail, the largest systematical error was derived from the calculation of effective frequency of collision which depends on the size of the trap and the energy of UCN. Next one was the shape of the function responsible for the UCN losses from reflection, and small uncertainty was given by the energy spectrum of UCN.

Experiments using magnetic storage ring

The lifetime measurement with NEutron STOrage Ring (NESTOR) was performed again at ILL reactor [21, 22]. A strong point of the measurement is that since neutrons were confined by magnetic barriers, they were free from wall loss. If the magnetic field $\boldsymbol{B}$ hold the following condition, neutrons are harmonically confined in a sextupole.

$$\begin{aligned} U &= -\boldsymbol{\mu_n} \cdot \boldsymbol{B} \propto r^2, && (1.24) \\ \boldsymbol{F} &= -\nabla U = \mu_n \frac{\partial \boldsymbol{B}}{\partial r} = c\boldsymbol{r}, && (1.25) \end{aligned}$$

where U is potential of magnetic field, F is the corresponding force and μ_n is the magnetic moment of the neutron. The setup and magnetic field are illustrated in Figs. 1.8 and 1.9.

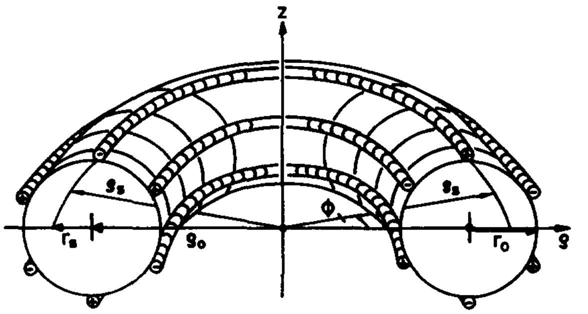

Figure 1.8: Schematic view of the magnetic sextupole trap [22].

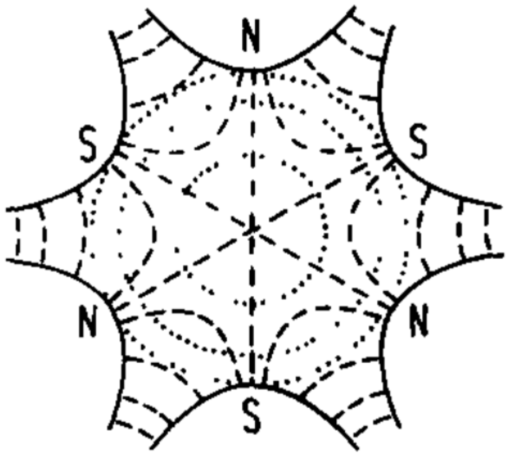

Figure 1.9: Cross section of an ideal sextupole [22]. Dashed line: magnetic field, dotted line: equal magnetic potential.

In this method, we should take the effect of the Lamor precession into consideration because there is a possibility of neutron loss arise from the change of the magnetic moment orientation respect to the magnetic field. The problem would be avoided if the frequency of magnetic field ω_B is small enough compared to the Lamor frequency ω_L.

$$\omega_L = -\frac{2\mu_n B}{\hbar} >> \frac{|\dot{\boldsymbol{B}}|}{B} = \omega_B \qquad (1.26)$$

The obtained neutron lifetime is $\tau_n = 876.7 \pm 10\,\mathrm{sec}$. Because of the possible neutron loss due to dynamics, an exponential fit was applied except the beginning of storage. The main component of error comes from low statistics.

1.3.3 Reported values of the neutron lifetime

As it is detailed in the previous sections, the neutron lifetime have been measured with two methods. The individual neutron lifetime values are shown in Fig. 1.10 and the averaged values are

$$\begin{aligned} \text{In-flight method :}\ \tau_\mathrm{n} &= 888.0 \pm 2.0\,\mathrm{sec} \\ \text{Bottle method :}\ \tau_\mathrm{n} &= 879.6 \pm 0.7\,\mathrm{sec} \end{aligned}$$

7 values in the Fig. 1.10 are averaged and one obtains [5],

$$\text{PDG2017 :}\quad \tau_\mathrm{n} = 880.2 \pm 1.0\,\mathrm{sec}$$

The results within each method showing good agreement but differ between in-flight method and bottle method. Therefore, there have been recent interest in improving the uncertainty on the neutron lifetime to below 0.1 %. The main sources of systematical uncertainties in in-flight method are derived from the measurement of beam flux and high background condition. While unexpected neutron losses are severe problem in bottle method. The measurement reached closer to the lifetime was carried out with gravitational trap and increasing number of measurements with gravitational trap and magnetic trap have been performed.

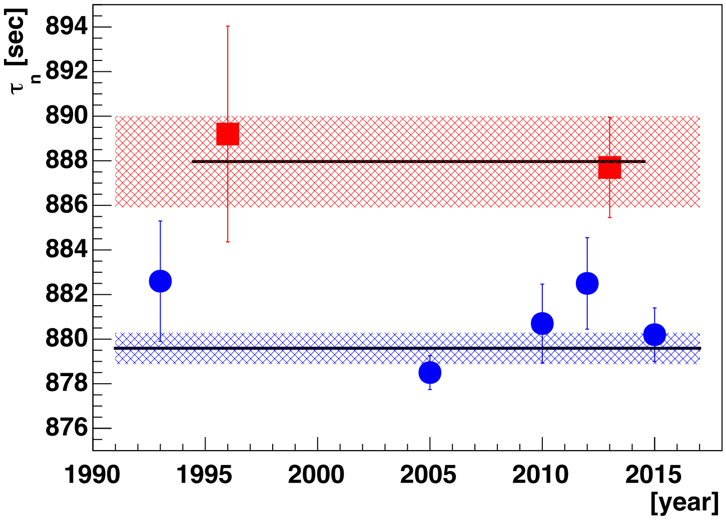

Figure 1.10: Previous results of the neutron lifetime measured by in-flight method (red) and by bottle method (blue) [23–29].

Part II

NOP experiment

Chapter 2

Neutron lifetime measurement at J-PARC

In this thesis, we report the neutron lifetime with accelerator based intense neutron beam at Japan Proton Accelerator Research Complex (J-PARC). We approach precise measurement with statistical advantage and the achievement of low background condition.

First, the experimental setup is described in chapter 2 and 3. The performance of neutron beam is descried in this chapter, and the construction of TPC and optical devices are explained in chapter 3.

In chapter 4, we focus on important neutron interactions, and categorize signals and backgrounds. The development of Monte Carlo (MC) simulation is described in chapter 5.

Then, analytic approach is detailed in chapter 6 and 7. These are the main topics in this thesis. Engineering data was taken in 2014 and 2015 (series 1, 2), and we confirmed the performance of apparatuses and established the method of analysis. Our first physics data have been taken in 2016 (series 3∼6). In total, we have 6 series of measurements with a new gas mixture for each measurement. The evaluation of the number of signal events are described in chapter 6, and efficiency of measurement are given in chapter 7. Finally, conclusions are given in chapter 8.

2.1 J-PARC

At J-PARC, a series of three accelerators provide world-class high energy proton beam to the experimental facilities (Fig. 2.1). A proton beam is accelerated by a 400 MeV linear accelerator (LINAC), a 3 GeV rapid cycling synchrotron (RCS) and a main ring (MR) which currently running at 30 GeV. The proton beam is extracted from MR and deliver to a mercury target at Materials and Life Science Experimental Facility (MLF). As the result of spallation reaction, high intensity pulsed neutron beam is produced with a repetition rate of 25 Hz.

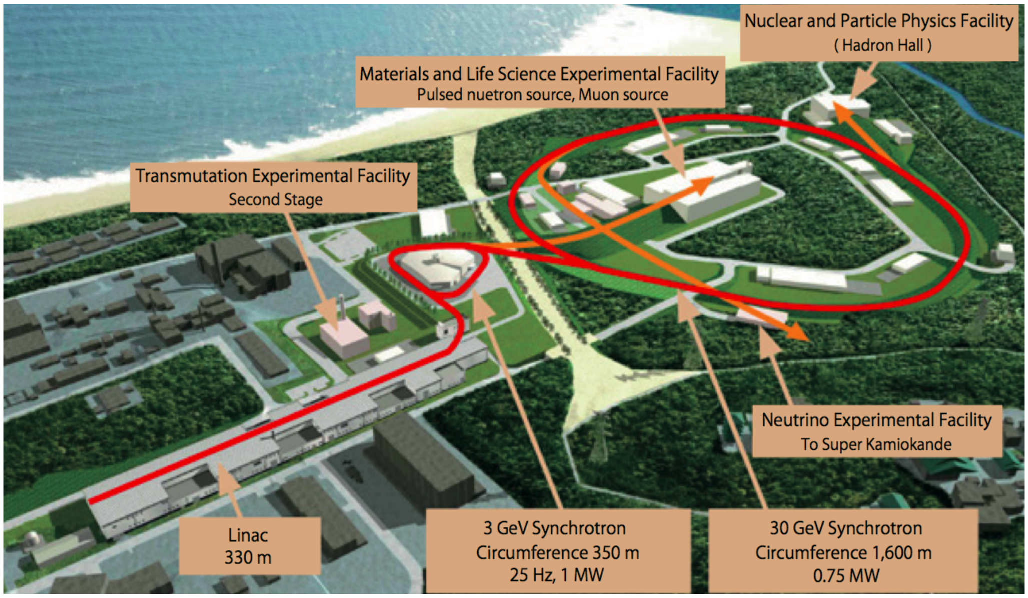

Figure 2.1: Bird's eye view of J-PARC [30].

Moderator

The neutrons are decelerated to cold region by a coupled hydrogen moderator and delivered to BL05, "Neutron Optics and Physics (NOP)" beamline. The coupled moderator have strong point in neutron flux, while time structure is broader than ones provided by a decoupled moderator. The neutron velocity is in the range between 500 m/s to 1200 m/s with a maxwellian distribution.

Time-integrated thermal neutron flux [n/s·cm^2]	4.6×10^8
Peak neutron flux at 10 meV [n/eV·s·cm^2]	6.0×10^{12}
Pulse width in FWHM at 10 meV [µs]	92

Table 2.1: Performance of neutron beam at 10 m from the coupled moderator at the 1 MW operation [30].

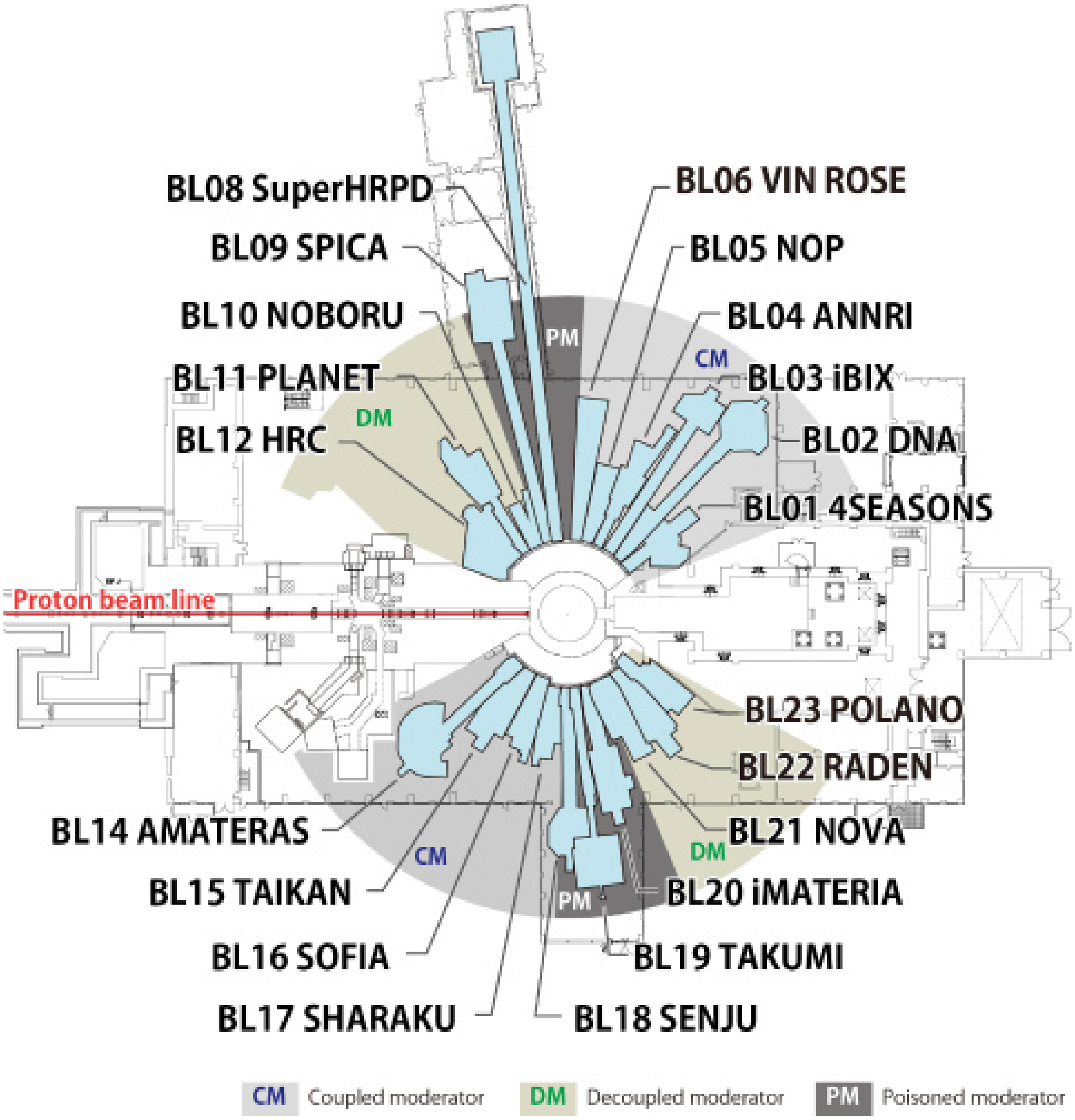

Figure 2.2: Neutron instruments at MLF [30].

2.2 NOP beamline

Figure 2.3 is the picture of NOP beamline. Supermirror guides and benders are aligned in 7.2 ∼ 12.0 m downstream of the exit of moderator and neutrons with different spin polarization and velocity are divided into three branches, the polarized beam branch, the unpolarized beam branch, the low-divergence beam branch (Figs. 2.4 and 2.5). Each beam branch is used according to the experimental requirement. The neutron lifetime experiment is carried out at the polarized beam branch. On the other hand, the experiments approaching fundamental physics of slow neutron such as electric dipole moment and T-violation are conducted at the other beam branches. Also, a doppler shifter for UCN production is developed.

A beam shutter which is made of 2 m thick iron is in 2.5 ∼ 4.5 m downstream of the moderator. When the beam shutter is closed, neutron beam is completely shut out. At usual operation, beam shutter is open during the data acquisition while the passage of neutron into detector is controlled by LiF shutter as described in Sec. 3.3. The beam performance at the 1 MW operation is shown in Tab. 2.2.

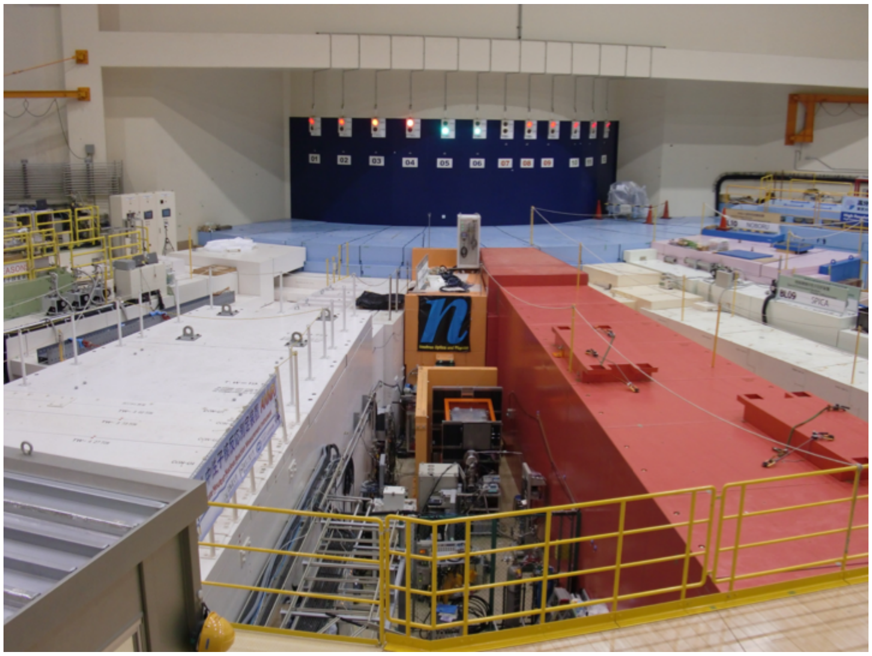

Figure 2.3: BL05 NOP beamline.

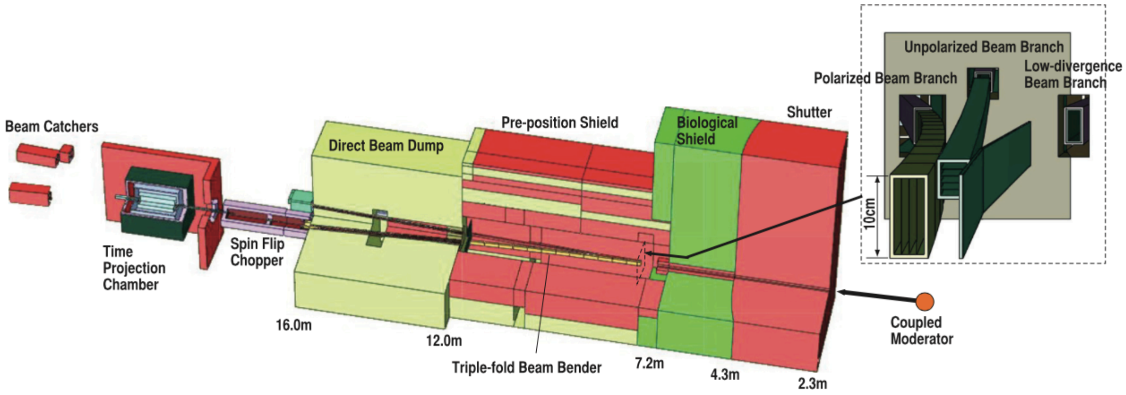

Figure 2.4: Overview of the NOP beamline [31].

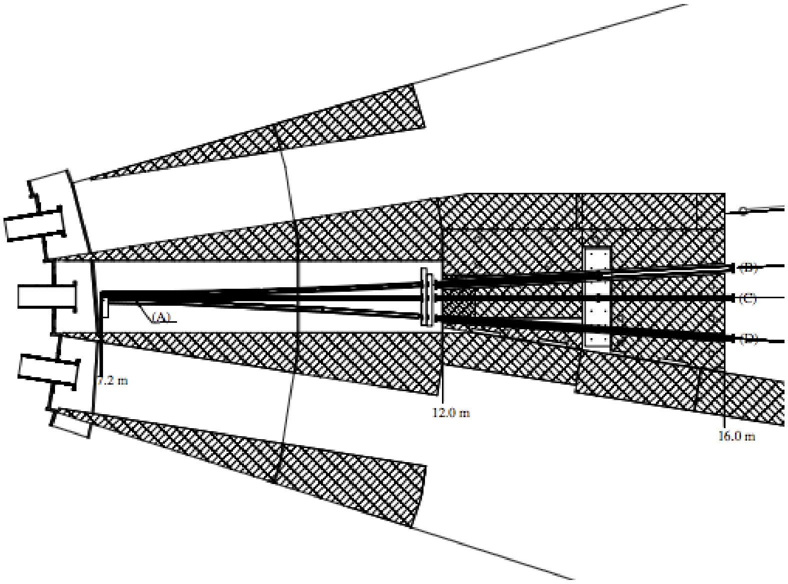

Figure 2.5: Illustration of the beam branches. (A) entrance of the beam benders, (B) exit of the polarized beam branch, (C) exit of the unpolarized beam branch, and (D) exit of the low-divergence beam branch.

Polarized beam branch

Polarized neutron beam is produced by using mirrors whose reflectivity depend on the neutron spin. Then, the polarized neutron beam is delivered to the experimental setup of the lifetime measurement. We have achieved the polarization efficiency of 96 % [33].

Unpolarized beam branch

This beam branch provide most intense neutron beam and is adopted for an experiment search for unknown medium range force, but it is currently used for the development of doppler shifter.

Low-divergence beam branch

An experiment for neutron interferometer is assigned to this beam branch. There is an interest in gravitational phase shift and Ahoronov-Casher effect. Successive performance of multilayer interferometer with spatially separated paths for the steady beam have been demonstrated [34].

	Polarized beam	Unpolarized beam	Low-divergence beam
Cross section [mm^2]	80×50	55×45	80×20
Neutron intensity [$\mathrm{n/s{\cdot}cm}^2$]	3.9×10^7	9.4×10^7	5.4×10^4
Beam divergence [μstr]	1.9×10^2	1.0×10^2	5.4×10^{-2}

Table 2.2: Beam performance at 16 m position (see Fig. 2.4) at the 1 MW operation [30].

Chapter 3

Experimental setup

Low background condition have been achieved by employing low radiative material for TPC and also large contribution from the development of spin flip chopper (SFC). The detail of our experimental setup including the formation of bunched neutron, TPC and trigger system are described in this chapter. The comparison of key features between NOP experiment and the experiment described in [6] is summarized in the end.

3.1 Overview of the setup

The overview of the setup is shown in Fig. 3.1. In the polarized beam branch, neutron beam pass through SFC to form neutron bunches. By making the time structure of neutron intensity, prompt γ rays are effectively discriminated. Then, bunched neutrons are transported to TPC which have been originally developed to suppress (n, γ) reactions. TPC is surrounded by lead shields and veto scintillators are installed outside of the lead shield. Further, the outermost is covered with iron shields in order to prevent environmental backgrounds.

3.2 Spin flip chopper

The polarized neutrons are delivered to SFC which consist of two radio frequency flipper coils and three magnetic supper mirrors. A single unit of SFC consist of a coil and two mirrors, and two sets of SFCs are used to provide outstanding performance. The spin of neutron is flipped by the flipper coils, and then neutrons are selectively reflected by the mirrors depends on the polarization. By the combination of coils and mirrors, neutrons are guided to TPC or beam dump and the time structure of neutron intensity is constructed.

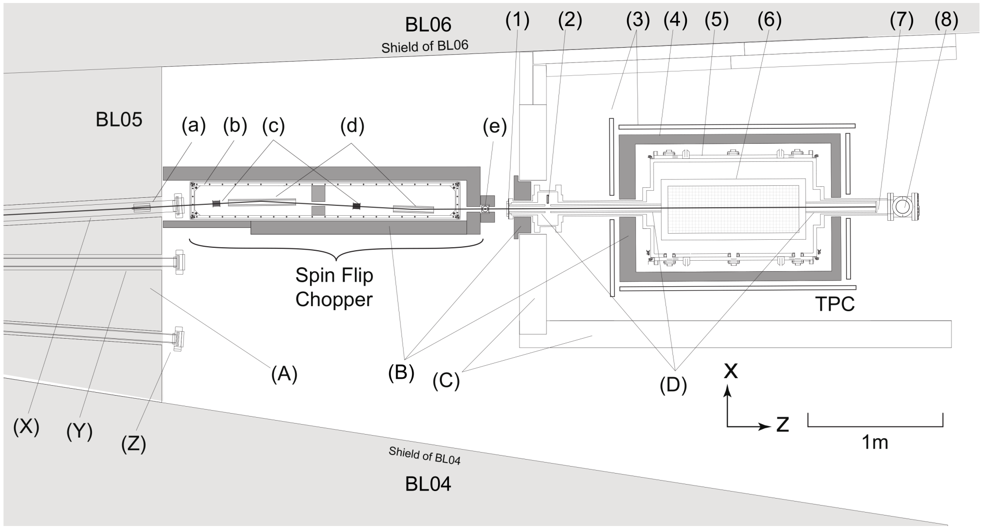

Figure 3.1: Overview of SFC and TPC. (X) polarized beam branch, (Y) unpolarized beam branch, and (Z) low-divergence beam branch. (a) short-pass wavelength neutron filter, (b) a guid coil, (c) first and second RFF coils, (d) magnetic supper mirrors, and (e) a neutron beam monitor. (A) beam dump, (B) lead shields, (C) iron shields, and (D) LiF beam collimators. (1) a Zr foil, (2) a LiF shutter, (3) cosmic veto counters, (4) lead shields, (5) a vacuum chamber, (6) a TPC, (7) a LiF beam catcher, and (8) a turbo molecular pump.

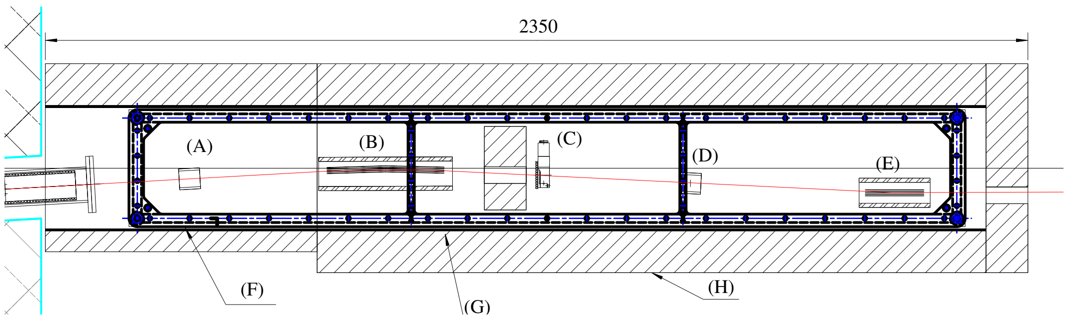

Figure 3.2: Illustration of SFC, viewed in xz plane. Polarized neutron is provided from the left side. (A) first RFF coil, (B) first and second mirrors, (C) a LiF shutter, (D) second RFF coil, (E) third mirror, (F) a guide coil, (G) boron gum, and (H) lead shields.

3.2.1 Radio frequency flipper coil

The radio frequency flipper (RFF) coil is nuclear magnetic resonance device which includes a solenoid coil and a guide coil (Fig. 3.3). The spin of neutron is rotated on the basis of Larmor precession. When the external magnetic field is applied perpendicular to the spin of neutron, a torque is exerted on the spin angular momentum. The flipping probability, P is given by Eq. (3.1).

$$P = \frac{B_{xz}^2}{B_{xz}^2 + (B_y - \frac{\hbar\omega}{2|\mu_n|})^2} \sin^2\left(\frac{|\mu_n| l}{\hbar v}\sqrt{B_{xz}^2 + (B_y - \frac{\hbar\omega}{2|\mu_n|})^2}\right), \tag{3.1}$$

where B_{xz} and B_y are the magnitude of the magnetic field applied by the solenoid coil and the guide coil, respectively. μ_n denotes the magnetic momentum of the neutron, ω is the frequency of the oscillation of B_{xz}, l is the length of RFF and v is the neutron velocity. The magnitude of the magnetic field applied by the guid coil is 1 mT.

When a current is supplied to RFF, the solenoid coil makes oscillating magnetic filed. If B_{xz} and ω satisfy the following conditions, P takes the maximum value.

$$\begin{aligned} B_y &= \frac{\hbar\omega}{2|\mu_n|} && (3.2) \\ \frac{|\mu_n| B_{xz} l}{\hbar v} &= (n + \frac{1}{2}\pi), && (3.3) \end{aligned}$$

here n is positive integers. By turning the current on and off, the length of the bunch is adjusted to be about a half the length of TPC. The specification of RFF is given in Tab. 3.1.

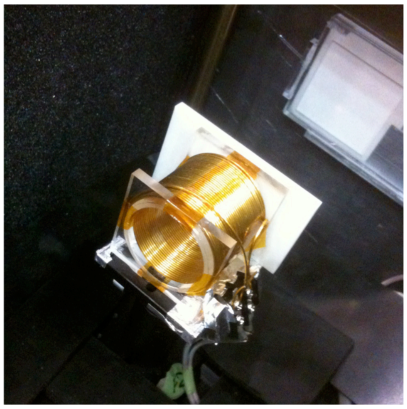

Figure 3.3: Radio frequency flipper coil.

Diameter [mm]	50
Length [mm]	40
Frequency of the magnetic field [kHz]	29
Magnitude of the magnetic field [mT]	0.3

Table 3.1: Specifications of the solenoid coil.

3.2.2 Magnetic supper mirror

The magnetic supper mirror have two kinds of layers, one consist of ferromagnetic material and another is made of non-magnetic material. The mirrors are placed in the magnetic field which is strong enough to magnetize the ferromagnetic material. In the slow neutron physics, neutron have wave properties and it can be reflected by making use of Bragg's law.

$$2d_n \sin\theta = m\lambda, \tag{3.4}$$

where d_n is the thickness of nth layer, θ is the incident angle, λ is the wavelength of the neutron and m is positive integers. As it is indicated in Eq. (3.4), the reflectivity depends on the thickness of layers. It means that neutrons with continuous distribution of wavelength can be reflected by changing the thickness gradually (Fig. 3.4).

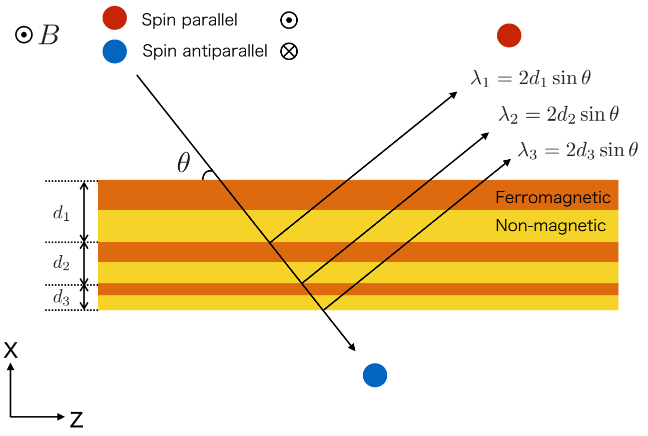

Figure 3.4: Basis of Bragg diffraction. The magnetic supper mirror is viewed in xz plane and the magnetic field is applied vertical to the paper surface. The neutron with spin parallel to the magnetic field (red) is reflected, while one with spin antiparallel (blue) penetrates the mirror.

Further, the reflectivity also depends on the neutron spin. Here we define the neutron with spin parallel (antiparallel) to the magnetic field as $n_{\parallel}$ ($n_{\perp}$). The magnetic potential of neutron is written as following.

$$V_{mag} = \begin{cases} V_{nucl} + |\mu_n| B & (n_{\parallel}) \\ V_{nucl} - |\mu_n| B & (n_{\perp}) \end{cases}, \tag{3.5}$$

where V_{mag} represents the magnetic potential, V_{nucl} is the nuclear potential, μ_n is the magnetic momentum of neutron and B is the magnitude of the magnetic field. While $n_{\parallel}$ is reflected toward TPC because it satisfies the Bragg condition, $n_{\perp}$ just go through the mirrors. Note that the neutron beam is inclined from the direction of the exit of SFC and that prevents γ rays to be detected. The specification of mirror is summarized in Tab. 3.2.

Figure 3.5: Magnetic supper mirror. A case is surrounded by magnets and five mirrors are aligned inside.

Ferromagnetic material	Fe
Non-magnetic material	$SiGe_3$
Thickness of layers [nm]	$1.9 \sim 60$
m-value	5
Mirror size [mm^3]	140 × 35 × 0.7
Number of mirrors	5
Magnetic field [mT]	35

Table 3.2: Specification of the magnetic super mirror.

Figure 3.6 shows the performance of SFC. The neutron intensity difference is defined as the signal-to-noise ratio of SFC and we have achieved the signal-to-noise ratio to be about

400. At 300 kW operation, we obtained 2.9×10^7 neutron/sec at the exit of the polarized beam branch. When neutron beam is formed into five bunches with a length of 40 cm, beam flux was measured to be 1.7×10^5 neutron/sec inside TPC.

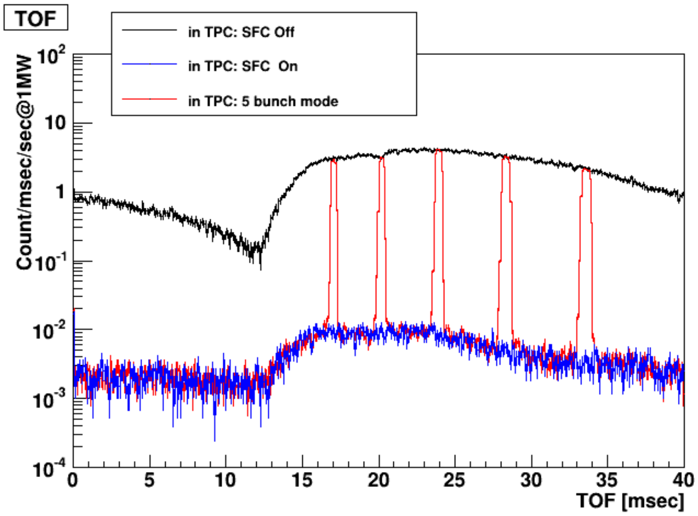

Figure 3.6: Neutron flux measured by TPC vs. TOF. The ratio of flux measured with SFC switched on and off is 1 to 400.

3.3 Beam entrance

The passage of neutron from the exit of SFC to the beam entrance of vacuum vessel is described in this section. Beam flux is monitored at the exit of SFC as it is shown in Fig. 3.1 (e). The beam monitor is used to compensate the fluctuation of beam flux and that have to be measured with an accuracy of 0.1 %. The beam monitor contains small amount of ^{3}He gas and is operated on the basis of proportional counter (Fig. 3.7). The gas gain have dependence on the high voltage, the temperature, beam flux and detection efficiency. The details were studied in [32] and an important problem was pointed out that there are more than 10 % of position dependence on detection efficiency. To avoid ambiguities in neutron flux measurement, the monitor is fixed to the incident neutron beam during the data acquisition. While the fluctuation derived from other factors were measured to be small enough and required stability of measurement is satisfied. The specification of the beam monitor is shown in Tab. 3.3.

Material	A5 aluminum
Active volume [mm^3]	$100 \times 42 \times 40$
Gas mixture	Ar (1.3 bar) + CH$_4$ (10 %) + ^{3}He
Thermal neutron detection efficiency	$\sim 4 \times 10^{-5}$

Table 3.3: Specification of beam monitor manufactured by Canberra Industries Inc. [32]

Neutrons enter to the vacuum chamber from a 50 µm thick Zr foil. Zr is adopted as entrance window because of the high mechanical strength and low neutron capture cross section. The passage to TPC is controlled by operating LiF shutter which consist of a LiF tile and stepping motor (Fig. 3.8). Two kinds of data, "Beam ON" and "Beam OFF", was taken by changing the shutter position and that is detailed in chapter 6. Note that when LiF shutter is closed, SFC is still irradiated and γ rays are continuously detected by TPC.

Figure 3.7: Neutron beam monitor MNH10/4.2F, product by Canberra Industries Inc.

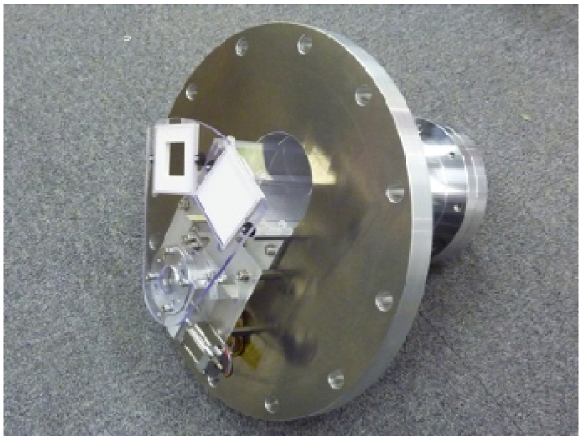

Figure 3.8: LiF shutter on the stepping motor.

3.4 Time projection chamber

In order to measure the neutron lifetime with high precision, it is very important to reduce the source of backgrounds, especially γ rays. The material of TPC was selected with great care, and also the materials placed inside of the vacuum vessel are selected to prevent radioactive contamination. The schematic view of TPC is shown in Figs. 3.9 and 3.10. The vacuum vessel contains drift cage, LiF tiles, MWPC and calibration source.

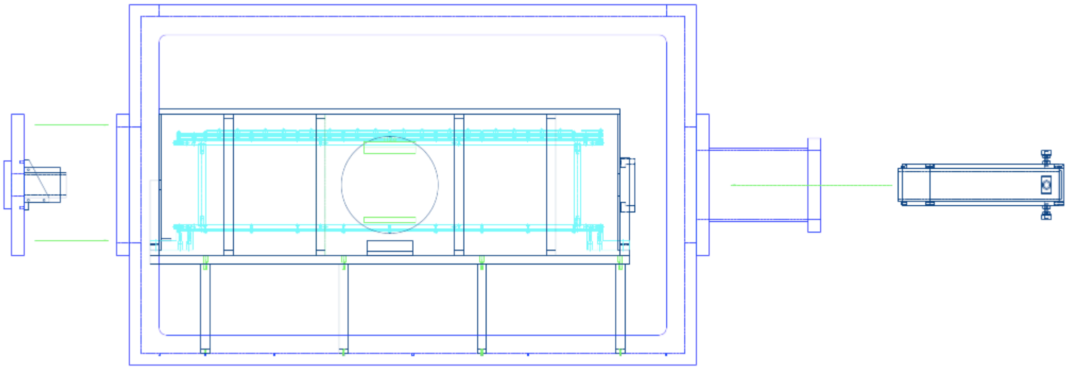

Figure 3.9: Schematic view of TPC in yz plane.

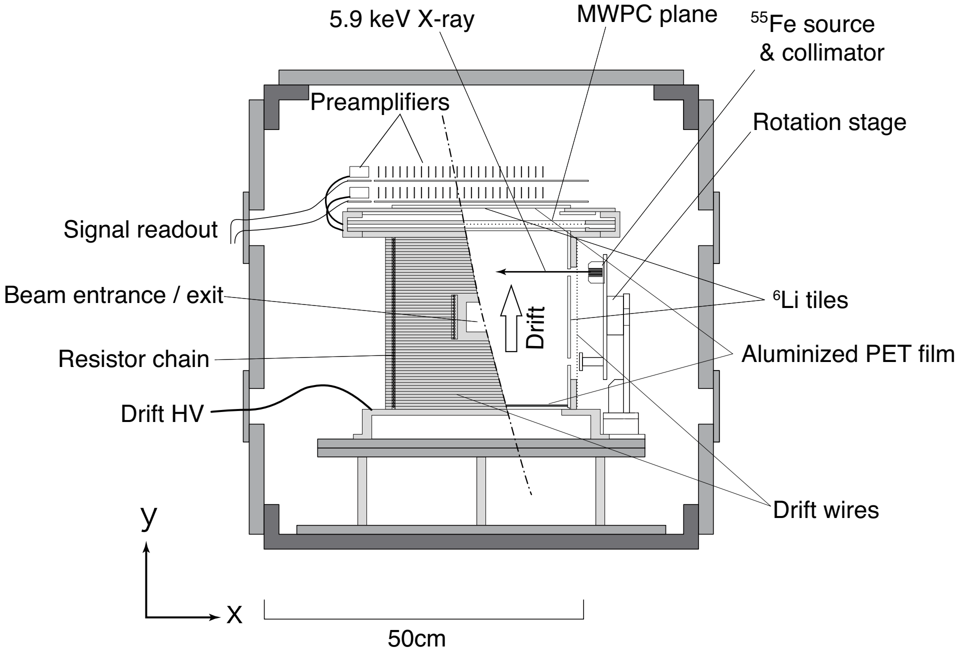

Figure 3.10: Schematic view of TPC in xy plane, viewed from downstream [36].

3.4.1 Drift cage

The schematic view of drift cage is shown in Fig. 3.11. We had five candidates for the TPC material as below [44].

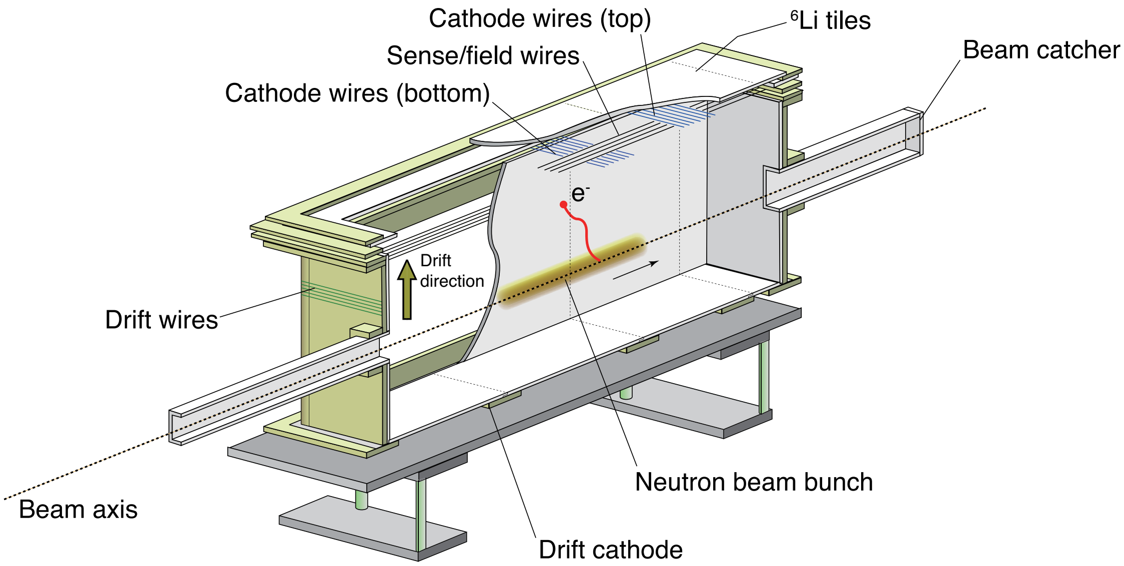

Figure 3.11: Schematic view of the drift cage [36].

- G10
- Poly ethel ethel ketone (PEEK)
- Poly phenylene sulfide (PPS)
- Phenol formaldehyde resin (PF)
- Alumina

Generally, G10 is used as a gas detector material. It is made of continuous glass woven fabric base impregnated with an epoxy resin binder. The radioisotope contamination have been tested by making a trial production and γ ray spectrum was measured by using a germanium detector. As the result, it was found that G10 includes the Uranium-Thorium series radioisotopes. Although G10 was removed from the candidates, significant isotope peak was not detected from PEEK. The γ ray spectra are shown in Fig. 3.12 and note that backgrounds were already subtracted.

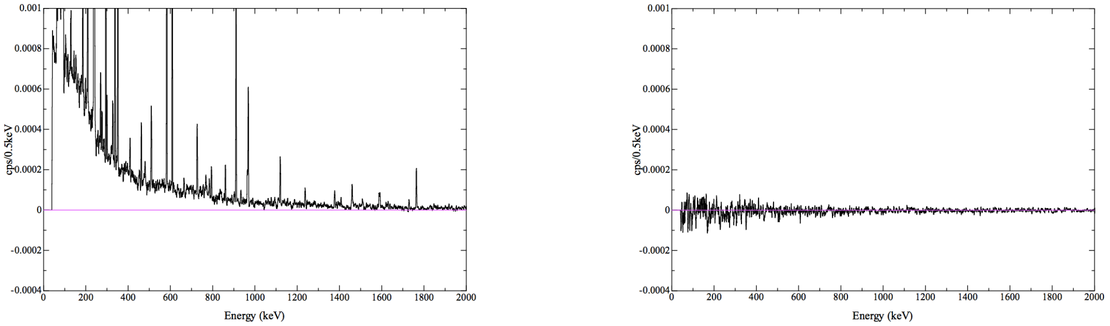

Figure 3.12: γ ray spectra of G10 (left) and PEEK (right), normalized by the measurement time and size of the samples [44].

PEEK is the product of a thermoplastic resin by Yasojima Proceed Co. Ltd. There are little possibility of radioactive contamination in the manufacturing process because the main components of PEEK are carbon, hydrogen and oxygen. Followings are the characteristics of PEEK whose product name is called PEEK450G [50]. As it satisfies our demand for construction and low background level, PEEK was selected as the material for our TPC. This is the first attempt to use PEEK as the material for a gas chamber.

- Low level of radioactivity
- Low outgassing and metal ion elution
- Machinable, weldable and bendable
- Mechanical strength for wire tension
- High insulation capacity
- Heat tolerance for soldering

LiF tiles

LiF tiles are fitted into the drift cage from inside and also they are used for beam catcher and shutter. The LiF tile is made by baking the ^{6}Li-enriched LiF powder (2.6 g/cm^3) with polytetrafluoroethylene (PTFE, 2.2 g/cm^3) at weight ratio of 3:7. The specification of the LiF tile is indicated in Tabs. 3.5 and 3.6. Each tile is covered with 100 µm thick PTFE sheets to absorb the α ray emitted from $^6\mathrm{Li}(n,\alpha)^3\mathrm{H}$ reaction. Since LiF tiles are installed to the place visible from the inside of TPC, neutrons scattered only once or less will certainly hit the LiF tiles (Fig. 3.14). The neutron absorption length of the LiF tile is about 0.5 mm and 99.95 % of neutrons are absorbed in 5 mm thick LiF tile.

	G10	PEEK	PPS	PF	Alumina
Density [g/cc]	1.8	1.3	1.4	1.4	3.9
Bending elastic modulus [GPa]	20	3.6	3.9	0.15	350
Melt point [°C]	-	334	278	130	1500
Water absorbing ratio [%]	0.10	0.14	0.04	0.3	0
Volume resistance [Ω·m]	10^{11}	10^{14}	10^{14}	10^{12}	10^{15}
Cost [1000JPY/kg]	3.3	45	8	5	100

Table 3.4: Physical properties of the materials [50].

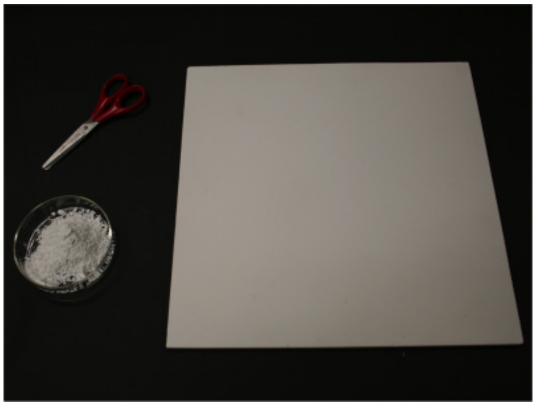

Figure 3.13: LiF tile.

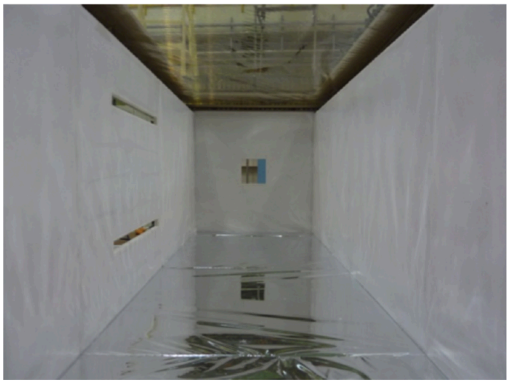

Figure 3.14: Inside of TPC viewed from upstream.

Size [mm^3]	300 × 300 × 5
Density [g/cm^3]	2.3
Relative permittivity	3.0

Table 3.5: Specification of the LiF tile.

	Mole fraction [%]
^{6}Li	17.3
^{7}Li	0.9
C	21.2
F	60.6

Table 3.6: Mole fraction of the LiF tile.

3.4.2 Multi wire proportional chamber

In this section, the properties of multi wire proportional chamber (MWPC) includes wires and preamplifiers are detailed.

Wires

There are four kinds of wires aligned in three xz planes with different y positions. As it is shown in Fig. 3.15, anode wires and field wires are arranged in parallel with the z axis and alternately aligned in the same xz plane. In the upward and downward of anode wires, there are cathode wires arranged in the x direction. While anode wires and downward cathode wires are connected to high gain preamplifiers, field wires and upward cathode wires are operated with low gain preamplifiers as it is described in the next section.

There are 28 anode wires and 27 field wires, but only 24 wires of each in the central region are read out. Four consecutive cathode wires are connected to single readout channel and there are 40 channels in each cathode plane. Totally, 128 channels are read out and recored as waveforms. The properties of wires are summarized in Tab. 3.7. One of the important difference between [6] and our experiment is that field wires are read out in our system. High voltage (1720 V) is applied to anode wires, while field wires with 0 V are supportive of the electric field to prevent distortion.

	Anode	Field	Cathode high	Cathode low
Number of wires	28	27	160	160
Number of channels	24	24	40	40
Pitch [mm]	12	12	6	6
Diameter [µm]	20	50	50	50
Material	W-Au	Be-Cu	Be-Cu	Be-Cu
Preamplifier	High gain	Low gain	High gain	Low gain

Table 3.7: Properties of wires

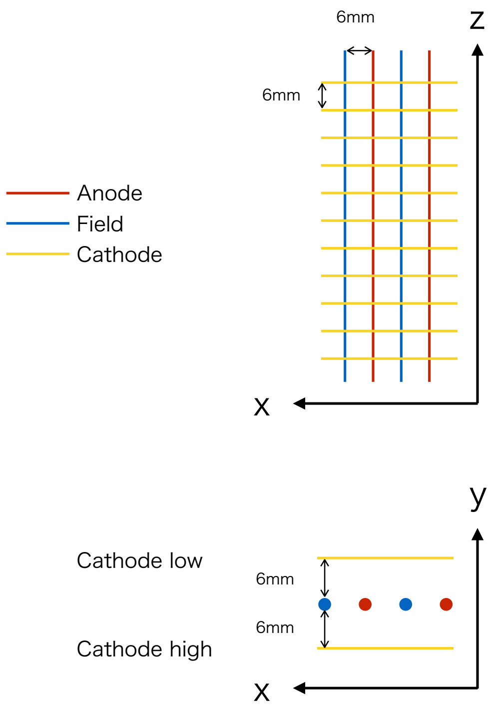

Figure 3.15: Wire geometry of MWPC.

Preamplifiers

The charge pulses from wires are integrated by preamplifiers and converted into a voltage. Figure 3.17 shows the circuit diagram of preamplifier. By adjusting the resistance of R0 and R1, it is possible to operate the preamplifier with different gain. In the low gain operation, R0 and R1 are set to $300\,\Omega$ and $1\,\mathrm{k}\Omega$, and about a quarter of the original charge is amplified. On the other hand, R0 and R1 are set to $0\,\Omega$ in the high gain operation so as to amplify total amount of the original charge.

In the design of preamplifier, high gain and low gain differ by a factor of approximately 4. However, it is found that the difference of gain was 5.5 in the measurement. That is because the operational amplifier in the circuit was operated without satisfying the condition of virtual grounding, due to insufficient resistance of R0.

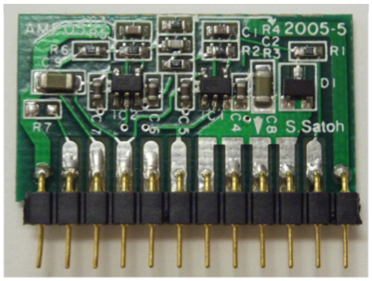

Figure 3.16: Preamplifier.

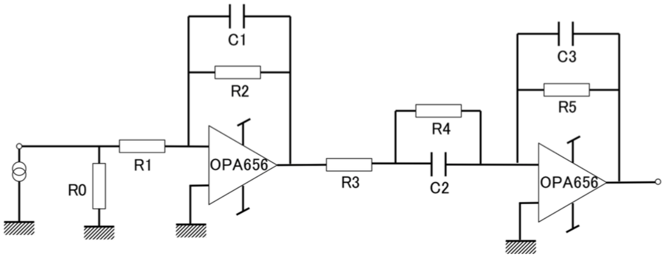

Figure 3.17: Circuit diagram of the preamplifier.

Electric field

The ionized particles drift toward MWPC in the applied electric field. In the region of increasingly high electric field, multiplication starts and charges are collected by anode wires. The electric field is formed as following. At the bottom of TPC, LiF tiles are covered with 12 µm thick aluminized PET film which is applied -9000 V, while MWPC plane is connected to the ground. As shown in Fig. 3.11, drift wires are coiled around the corners of drift cage, that help to make uniform field. Another PET film covers the top of TPC that the electric field prevents to trigger cosmic rays generated in the upward of TPC. Besides, it works to avoid charge up.

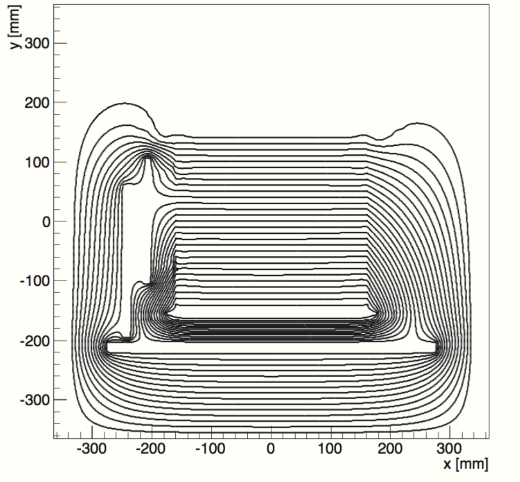

Figure 3.18: Electric field of the drift region in xy plane, viewed from upstream.

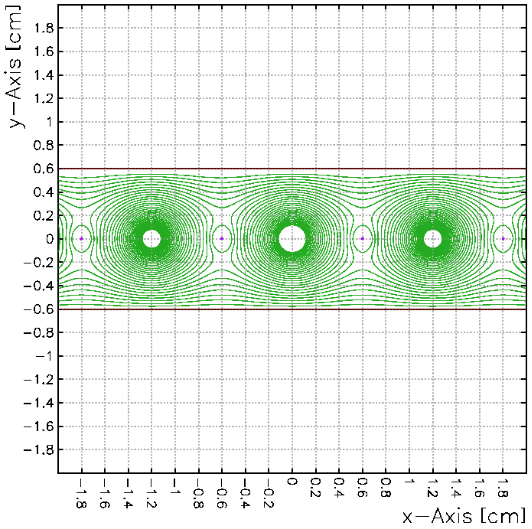

Figure 3.19: Electric field around the anode wires.

Figure 3.19 shows the electric field calculated by using Garfield, under the condition of 100 kPa and 300 V/cm. In designing, the position dependence of electric field was estimated to be less than 1 %. However, we observed that the drift velocity depends on the position in y direction. A possible reason of the electric field distortion is dielectric material contained in PEEK and LiF tile. The measured relative permittivity of PEEK and LiF tile result in 3.2 and 3.0, respectively. The non-uniformity of the electric field is estimated to be not more than 10 % and that is explained in Sec. 7.2.

3.5 Chamber gas

In general, argon and isobutane are widely used as the fill gas of a MWPC because of its high gain and lower cost. For the requirement of our experiment, the fill gas should have low neutron scattering cross section. Therefore argon and hydrogen were removed from the candidates and we employed a mixture of ^{4}He 85 % + CO_2 15 %. ^{4}He have a low neutron scattering cross section of 1.34 barn and do not absorb neutron. Although the quenching gas, CO_2, have about 4 times larger neutron scattering cross section, this is comparatively low probability of scattering. The components of commercial product of ^{4}He gas named G1He, and that of CO_2 gas named G1CO2 are summarized in Tabs. 3.8 and 3.9. According to the mass spectrometry, about 0.1 ppm of ^{3}He is contained in the ^{4}He gas and that will be corrected in the evaluation of number density of ^{3}He (see appendix D).

Component	Quality standard
He [%]	99.9995
O_2 [ppm]	< 0.5
N_2 [ppm]	< 5
CO [ppm]	< 0.5
CO_2 [ppm]	< 0.5
THC [ppm]	< 0.5

Table 3.8: Component of ^{4}He gas, commercial product by Tomoe shokai Co., Ltd.

Component	Quality standard
Purity [vol. %]	> 99.9990
Moisture [vol. %]	< 0.0010
Sulfide [wt. ppm]	< 0.03
Carbonhydrate [vol. ppm]	< 1
H_2, N_2, O_2, Ar [vol. %]	< 0.0010

Table 3.9: Component of CO_2 gas, commercial product by Tomoe shokai Co., Ltd.

3.5.1 Measurement of ^{3}He density

We introduce about 1 ppm of ^{3}He gas into TPC by making use of thermometers and three kinds of pressure gauges with different measurable range (Tab. 3.10). Because ^{3}He density is very small and such a small pressure can not be measured directory, the gas mixture is introduced by a slightly elaborate procedure as described below.

To prevent the possibility of biasing in the evaluation of signal events, we employ blind analysis and ^{3}He density is disclosed after these analysis have been fixed.

Pressure gauge	Full scale [kPa]	Accuracy [%]
A	120.	0.01
B	35.	0.01
C	1.333	0.05

Table 3.10: Specification of pressure gauges.

Basis of the measurement

Number density of ^{3}He is measured by introducing the gas into vessels with different volume V_1 and V_2. Assume that V_1 is small and V_2 as TPC, and they are connected by a valve (Fig. 3.20). Firstly, ^{3}He is introduced into V_1 with high pressure and we measure the pressure P_1 and temperature T_1. Equation (3.6) is obtained on the basis on ideal gas law:

$$P_1 V_1 = nRT_1. \tag{3.6}$$

P_1 can be measured precisely since the precision of pressure gauge is proportional to the pressure. Subsequently, the valve is opened to diffuse the gas into V_2, then pressure P_2 and temperature T_2 are measured. ^{3}He density ρ is calculated as following.

$$P_2(V_1 + V_2) = nRT_2, \tag{3.7}$$

$$\rho = \frac{P_1}{RT_1}\frac{V_1}{V_1 + V_2}, \tag{3.8}$$

where n is the amount of ^{3}He and R is the gas constant. Thus, ρ is derived from three parameters, P_1, T_1, and ratio of V_1 and V_2. The volume ratio have been measured ahead of the neutron lifetime measurement.

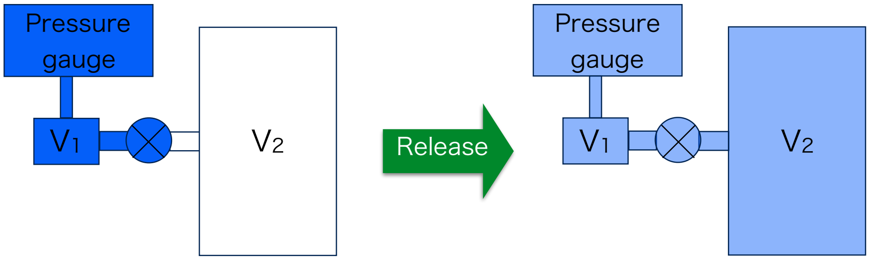

Figure 3.20: Basis of gas introduction. ^{3}He gas is introduced to small volume (V_1) and expanded to larger volume (V_2).

Procedure of gas introduction

In the procedure of gas introduction, ^{3}He is introduced at first and then ^{4}He and CO_2 follows. Figure 3.21 shows the gas introduction system, where pipes and valves are indicated with “I” and “V”. Pipes are connected with each other and hermetically sealed by valves. Pressure gauges A and B are connected with V_8 and, gauge C is connected with V_5. ^{3}He gas is introduced from I_6 and diluted by diffusing many times as below.

1. $I_6 \rightarrow I_6 + I_5$
2. $I_6 + I_5 \rightarrow I_5$
3. $I_5 \rightarrow I_5 + I_4 + I_1 + I_m$
4. $I_5 + I_4 + I_1 + I_m \rightarrow I_m$
5. $I_m \rightarrow I_m + I_1 + I_7 + I_8 + I_{TPC}$

Series	^{4}He [$\times 10^{25}$ atom/m^3]	CO_2 [$\times 10^{24}$ atom/m^3]	^{3}He [$\times 10^{19}$ atom/m^3]
1	2.0124(7)	3.55(2)	2.24(1)
2	1.9880(7)	3.50(2)	1.867(5)
3	2.0292(7)	3.59(2)	2.127(7)
4	2.0137(7)	3.56(2)	3.96(1)
5	2.0106(7)	3.53(2)	0.993(4)
6	2.0009(7)	3.50(2)	2.089(7)

Table 3.11: Number density of injected gases.

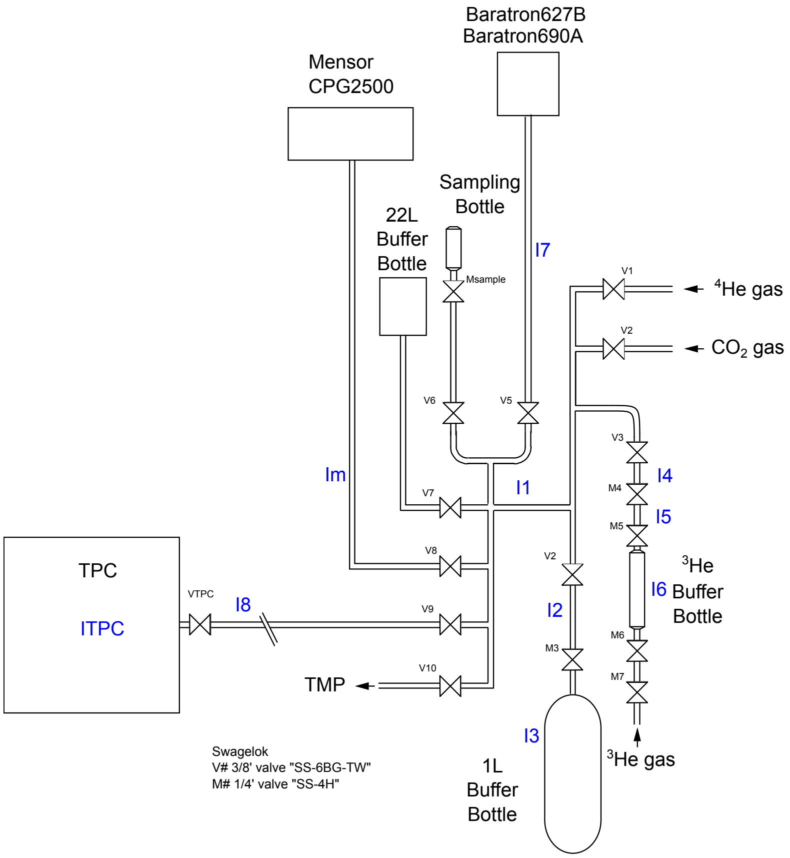

Figure 3.21: Illustration of the gas introduction system. The pressure gauges A and B correspond to two channels of Mensor CPG2500, and the gauge C is Baratron690A.

Systematical uncertainties of ^{3}He density

The systematical uncertainties in the measurement of ^{3}He density are mainly derived from the precision of instruments and deformation of vessel. Besides, the deviation from ideal gas law slightly affect the measurement and these are summarized in Tab. 3.12.

Series	1	2	3	4	5	6
Volume expansion	0.46	0.28	0.31	0.27	0.41	0.31
Heat generation by preamplifier	0.35	0.29	0.27	0.33	0.30	0.30
Contamination from G1He	0.18	0.18	0.16	0.086	0.61	0.28
Deformation of vessel	0.16	0.15	0.15	0.15	0.15	0.15
Impurity of pure ^{3}He	0.066	0.066	0.066	0.066	0.066	0.066
Virial coefficient	0.0004	0.0005	0.0005	0.0005	0.0005	0.0005
Thermal transpiration	0.0001	0.0001	0.0001	0.0001	0.0001	0.0001
Total	0.6	0.5	0.4	0.5	0.7	0.5

Table 3.12: Systematical errors of ^{3}He density in percentage.

3.6 Cosmic ray veto counter

The aluminum vessel is surrounded by scintillation counters to veto cosmic ray backgrounds as shown in Fig. 3.22. Single counter consists of a few number of plastic scintillators and a photo multiplier. Scintillators are covered with reflectors and light shielding, and wavelength shift fiber are inserted. Each side of the TPC is covered with two counters and veto signal is generated by taking the coincidence. Figure 3.23 shows a counter which is put in the front and back of the TPC. It has a trench with 20 mm pitch to pass the beam. From the outside, the trench is covered with a couple of small square counter.

Figure 3.22: Cosmic ray veto counters.

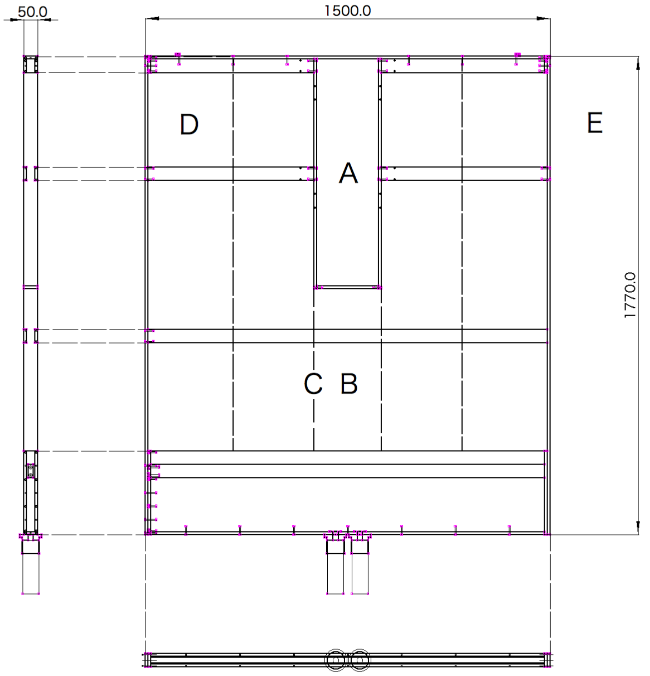

Figure 3.23: Drawing of the cosmic ray veto counter (Front and Back).

Position	A	B	C	D	E
Top	99.52 ±0.06	99.57 ± 0.02	99.19 ± 0.04	99.73 ± 0.04	99.12 ±0.04
Front	-	99.60 ± 0.02	98.83 ± 0.04	99.64 ± 0.04	-
Back	-	99.76 ± 0.02	98.92 ± 0.04	99.73 ± 0.04	-
Right	100.00 ±0.06	99.65 ± 0.02	98.74 ± 0.04	99.73 ± 0.04	98.34 ±0.04
Left	99.69 ±0.06	99.46 ± 0.02	97.66 ± 0.04	99.82 ± 0.04	98.93 ±0.04
XFront	97.95 ±0.06	-	-	-	-
XBack	98.58 ±0.06	-	-	-	-

Table 3.13: Detection efficiency of veto counters [44]. Position A∼E are shown in Fig. 3.23.

Usually veto counters are used to remove cosmic ray events, while cosmic ray measurements are included in the data acquisition cycles in order to evaluate the wire efficiency and to estimate the accuracy of energy calibration. In that case, veto counters are used to generate trigger signal.

3.7 Calibration source

Energy deposit is calibrated by using ^{55}Fe checking source which emit X-ray (5.9 keV). The checking source is set on the rotating table and different y position, $y = 75$, 0, and -75 mm, can be selected (Figs. 3.24 and 3.25). Here, center of TPC is defined as standard y position. As it is shown in Fig. 3.14, there are windows in the side wall.


Figure 3.24: Checking source on the rotating table.

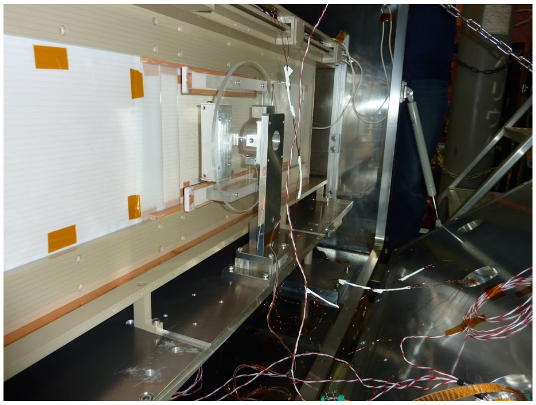
Figure 3.25: Side view of TPC. The source is fixed to $y = 0$ mm.

When checking source is fixed to $y = 0$ mm (Fig. 3.25), windows are covered with LiF tiles. While rotating table is set to $y = 75$ or -75 mm, the X-ray is emitted from the window and energy deposit caused by photoelectric effect is detected. The obtained energy resolution was 22.9 % FWHM at 5.9 keV, under 100 kPa operation.

The transition of pulse height is shown in Fig. 3.26. Comparing the measurement with different y position, the effect of attenuation appears as it is proportional to the drift length. The energy deposit from $y = 75$ or -75 mm at a certain time can be obtained by fitting the transition. The fit function is given as

$$f = A\ (1 - Be^{-\frac{t-t_0}{\tau}})\ e^{-l(t-t_0)}, \tag{3.9}$$

where t is a certain time of the measurement, t_0 is the time when gas have been filled and l is the drift length which is equal to 75 mm (225 mm) when the calibration source is positioned at $y = 75$ mm (-75 mm). A, B and τ are constants in charge of the effect of outgas and recombination.

Since magnetic field is not applied to the TPC, the important point of our experiment is that what is indicated in y direction is only relative position of energy deposit. For that reason, we assume that all ionized particles are generated at the standard y position and energy calibration have been performed by interpolating these two fits in Fig. 3.26.

The uncertainty of energy calibration would be maximized when ionized particles are generated near the MWPC or bottom of the TPC.

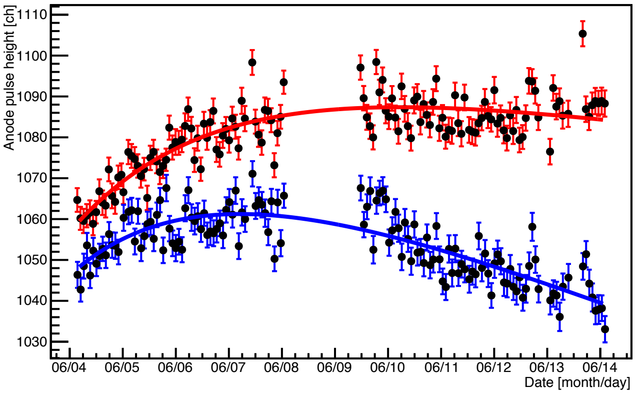

Figure 3.26: Transition of pulse height. The calibration source was positioned at $y = 75$ mm (red) and $y = -75$ mm (blue).

3.8 TPC performance

Multiple gain

To measure the multiple gain, the checking source was placed just above the MWPC. In such a setup, ionized particles were detected without drifting in the TPC. Assuming W-value of ^{4}He (42 eV), multiplication gain was calculated to be 4×10^4. Because we have developed TPC with such a high gain, low level threshold equivalent to 0.2 keV is applicable.

Drift velocity

Drift velocity is estimated by using cosmic ray events. If we require a series of hits in anode wires and the track to be penetrated in y direction, the absolute y position of the ionized particles can be determined with a certain accuracy because the angle of cosmic ray can be restricted by the number of hit wires. Assuming that there are hits with two anode wires, Fig. 3.27 shows the ideal case (left) and worse case (right) to calculate the drift velocity. Since actual drift length l_1 is equal to the height of TPC, the drift velocity can be calculated accurately. In the worse case, l_2 is shorter than the height of TPC and the time difference of hits also become shorter. Therefore, the drift velocity is mistaken as faster.

Consequently, the drift velocity is given as a function of number of hit wires and more accurate result can be obtained with larger number of hits. Standard velocity is calculated by extrapolation, resulted in about 1 cm/µs with 100 kPa operation (Fig. 3.28).

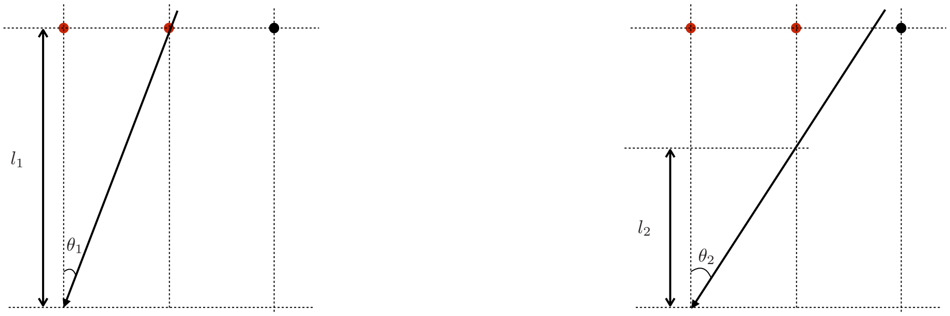

Figure 3.27: Ideal case (left) and worse case (right) to calculate the drift velocity by using cosmic ray. TPC is viewed in xy plane and hit anode wires are indicated with red.

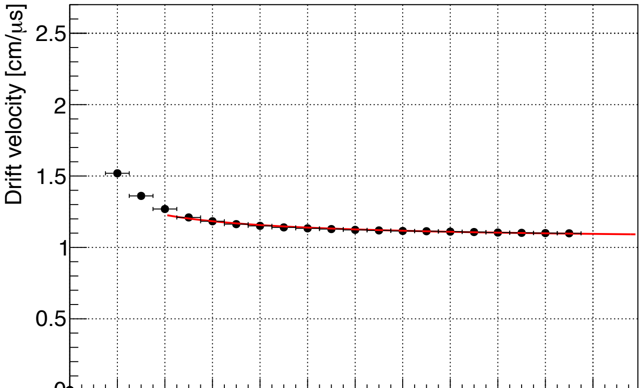

Figure 3.28: Drift velocity calculated with different number of hit anode wires.

Anode wire detection efficiency

In order to estimate the detection efficiencies of anode wires, cosmic ray events are triggered by veto counters and the track penetrating the TPC in y direction are selected. The efficiency of each anode wire was determined by the hit ratio of the events in which both side of wires have hits and we obtained the averaged wire efficiency to be more than 99 % at 100 kPa.

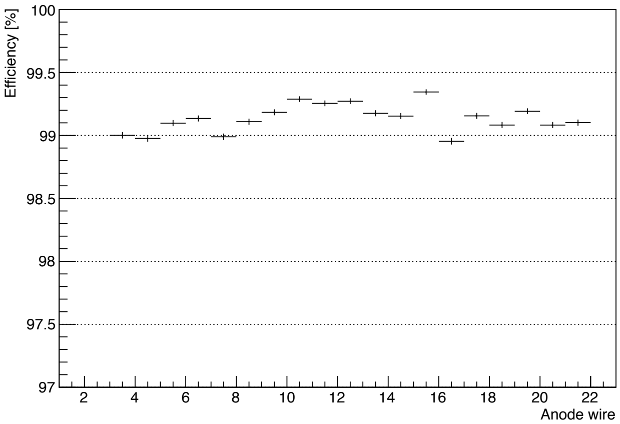

Figure 3.29: Detection efficiencies of anode wires.

Background rate

After the installation of veto counters and shields, the rate of environmental background is measured to be 7.7 cps. The environmental γ rays and cosmic rays account for 1.3 cps and 2.0 cps, respectively. The remaining backgrounds are derived from radioisotope inside TPC and vacuum vessel.

Stability of operation

Since the gas introduction, three things might be changed with elapsed time. One is temperature, that would rise to a few degree Celsius and gives uncertainties of number density of ^{3}He. Another thing is radioactivation around the TPC. The backgrounds correspond to neutron capture reactions would increase proportional to the beam flux. They are considered in Sec. 6.3.2.

The other is the deterioration of vacuum condition. Because the aluminum vessel have been sealed during the data acquisition, outgas will increase. Increasing amount of outgas lower the multiple gain and also reduce the accuracy of the energy calibration. This is one of the most significant problems affect the stability of operation. Hydrogen and oxygen are contained in the outgas and large electron affinities are given to them. The effect of attenuation appears in the difference of pulse height measured with the source fixed at different y position (Fig. 3.30).

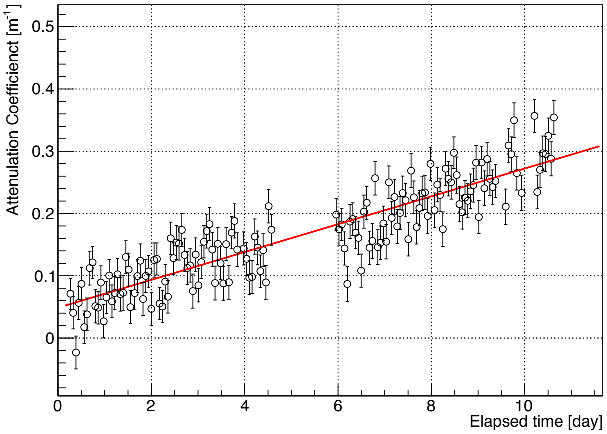

Figure 3.30: Transition of the attenuation coefficient. The operation was suspended in the blank space because of the maintenance of the accelerator.

The amount of outgas depends on the vacuuming before starting data acquisition. When gas introduction was started with the vacuum condition of 3.6×10^{-4} Pa, outgassing was measured to be 4.4 Pa/day. After 5 days of operation, the uncertainties in multiple gain and drift velocity were estimated to be 10 % and 1 %, respectively. In order to avoid the uncertainty in the energy calibration, continuous data cumulation is restricted to about 10 days at longest.

3.9 Readout electronics

Our readout system consist of a common pipelined platform for electronics readout (COPPER) with digitization daughter cards called FINESSE, front-end instrumentation entities for sub-detector specific electronics. Both of FINESSE and COPPER are products developed by KEK [37].

Readout system proceed as follows (Fig. 3.31). Trigger signal is emitted when any anode signal exceed the threshold. Firstly, waveforms from 128 channels are sent to flash ADC type FINESSE cards which digitizes waveforms with 20 MHz clock and 12 bit dynamic range. A FINESSE card have 8 channels so that there are 16 cards for ADC and two cards for TDC. A set of four FINESSE cards is on a COPPER board, and each card is consecutively read out with the transmission rate of 1 Gbps. In total, five COPPER boards are used. Finally, waveforms are recored from 30 μsec before to 70 μsec after the trigger signal with

2048 channel resolution. Synchronized with the readout of ADC, the time-of-flight (TOF) and the beam monitor count are also transmitted. The time difference between the collision of latest proton pulse on the mercury target and trigger signal is recorded by TDC which have 1.25 MHz clock and 16 bit dynamic range.

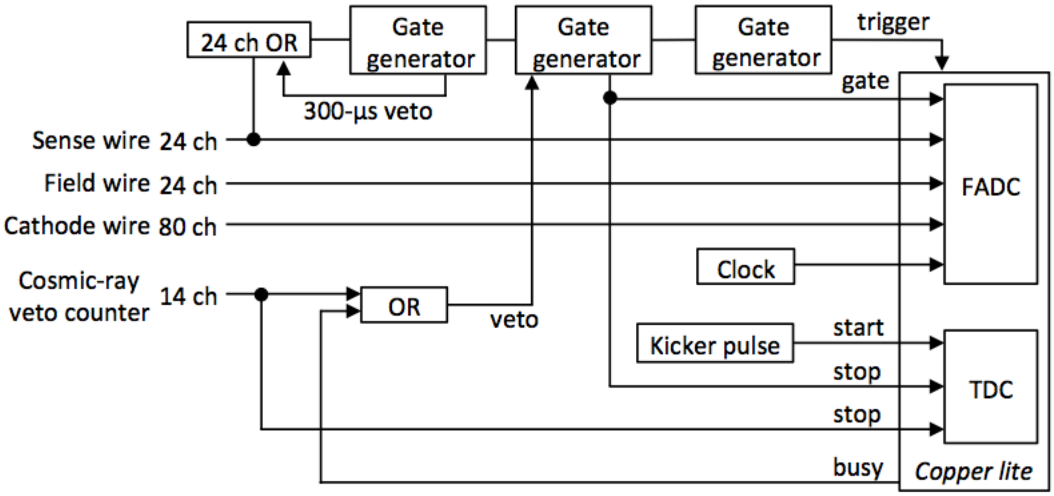

Figure 3.31: Block diagram of the readout electronics [31].

COPPER	
Number of boards	5
Number of FINESSE cards on a COPPER board	4
FINESSE 8 ch FADC	
Number of cards	16
Clock	1 ∼ 65 MHz
Dynamic range	100 µsec (12 bit)
Channel	8 ch
Data size	2 kbyte/ch
FINESSE 32 ch multi hit TDC V2	
Number of cards	2
Clock	1.25 MHz (16 bit)
Channel	32 ch

Table 3.14: Specification of readout system.

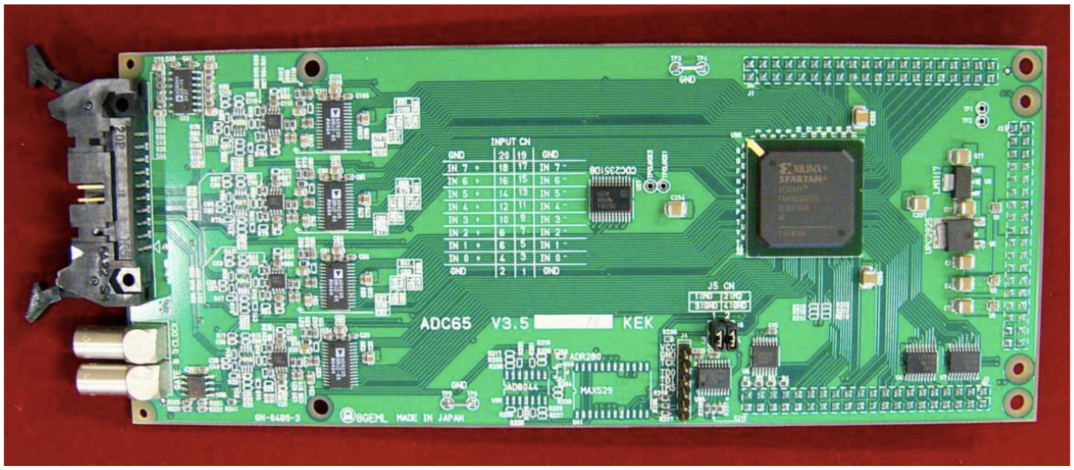

Figure 3.32: GNV-440 FINESSE 8ch ADC board (12bit/65MSPS).

Trigger selection

We conduct four kinds of measurements and trigger condition is selected depend on the purpose.

- Beam ON (LiF shutter open)
- Beam OFF (LiF shutter closed)
- Calibration
- Cosmic ray

In the measurement of cosmic ray, trigger signal is generated by the coincidence of scintillation counters. Otherwise, scintillation counters veto cosmic rays and the first fired anode wire creates the trigger signal.

Dead time

A veto signal is emitted if scintillation counters are triggered or TPC emit the trigger signal to record an event. The readout system is vetoed for 70 µs in the former case. According to vetoed time, dead time is calculated to correct the number of triggered events.

As it is shown in Fig. 3.31, we record the TOF of kicker pulse, veto start and veto stop. The number of times to take a certain TOF is counted by referring the kicker pulse, and that can be expressed as a step function of TOF, $A(t)$. While vetoed time $B(t)$ is defined as the

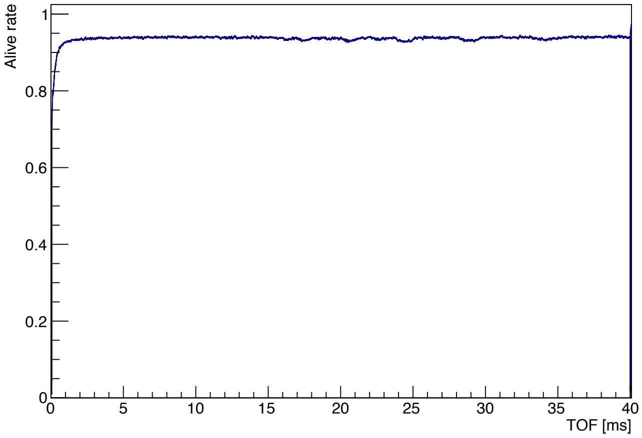

Figure 3.33: Alive rate vs. TOF.

period from veto start to veto stop. $B(t)$ is divided by $A(t)$ and we obtain the correction for dead time. Alive rate is calculated as the complement of dead time rate and that is shown in Fig. 3.33. When alive rate is equal to 1, that means no correction is required. A fluctuation of alive rate can be seen in the region of TOF $> 15\,\mathrm{ms}$, because of the increase of trigger signal caused by the arrival of neutron bunches.

3.10 Summary of the features of experimental setup

The features of experimental setup are summarized in Tab. 3.15, compared with the experiment by ILL-ISN-LAPP collaboration [6]. One of the points is the source of neutron. In the experiment described in [6], high flux neutron was provided from the research reactor and rotating chopper dram was used to make monochromatic neutrons. On the other hand, rapid-cycling synchrotron (RCS) at J-PARC delivers proton beam to targets producing the intense cold neutron. In the configuration shown in the table, the neutron decay rate is comparable.

Another point is the rate of backgrounds. We have reduced radiative sources by selecting the material inside TPC and possible backgrounds are taken into consideration with great care as described in the following chapter. The other distinctive features of our experiment are low gain operation and high detection efficiency which have been achieved by adopting the lower threshold. Low gain operation is possible for our TPC, that contribute to estimate neutron capture reactions in ^{14}N and ^{17}O. Further, operation with lower pressure is under investigation and it will help to reduce beam induced backgrounds.

	NOP	ILL-ISN-LAPP collaboration
Beam profile		
Source	Accelerator based	Reactor based
Repetition rate [Hz]	25	110
Pulse per repetition	5	1
Pulse length [cm]	40	23 ~ 25
Beam size [mm^2]	20 × 20	15 × 25
Beam divergence [mrad]	± 4.2	± 8.7
Neutron velocity [m/s]	500 ~ 1200	837
Duty factor for fiducial time (=F)	0.059	0.044
Neutron flux inside the TPC [1/s]	1.3×10^5	2.2×10^5
TPC		
Drift cage [mm^3]	290 × 295 × 960	190 × 190 × 700
MWPC cell size [mm^3]	12 × 12	10 × 10
Gas pressure [kPa]	100	95
Gas mixture [He : CO_2]	85 : 15	93 : 7
^{3}He abundance [ppm]	~ 1	0.7
Event rate		
Neutron decay rate [1/F·s]	0.092	0.10
Environmental background [1/s]	8	80
Neutron induced background [1/s]	2	20

Table 3.15: Comparison of setup between the experiment described in [6] and NOP experiment, assuming 220 kW beam power at J-PARC.

Chapter 4

Neutron interactions

Neutron interactions induce backgrounds and that have significant influence to the systematical errors in the neutron lifetime. This chapter introduce the neutron interactions and briefly sort out how to deal with the backgrounds. Categorization of signals and backgrounds are summarized in the end of this chapter.

4.1 (n, γ) reactions

Beam correlated backgrounds are dominated by (n, γ) reactions. Since possible energy of γ ray is a few MeV at most, the energy deposit of γ rays are detected as the result of photoelectric effect or compton scattering. The discrimination of γ rays is a serious problem to count the decay electrons and the backgrounds can be avoided by using material with low absorption cross section.

In our experimental setup, mainly four places are exposed to the neutron beam. One is the magnetic super mirror whose main component is ^{28}Si. The other three places are inside of TPC, the beam catcher and the LiF shutter at the entrance of TPC. These places are covered with the LiF tiles which consist of ^{6}Li, ^{7}Li, ^{12}C and ^{19}F. Also, it has to be taken into account that neutrons are absorbed by CO_2 gas. The characteristics of (n, γ) reactions whose short descriptions are given as below are linked with the analytic approach and that is detailed in chapter 6. Note that in most cases more than one γ ray will be emitted.

- ^{6}Li(n, γ) and ^{28}Si(n, γ)
  Only prompt γ rays are emitted from the absorption reactions in ^{6}Li and ^{28}Si. The time structure of neutron decay and that of prompt γ rays generated in the upstream are different from each other, so that the backgrounds are easily removed by TOF method. However, γ rays from LiF tiles are not discriminated by TOF method and they are corrected in Sec. 6.4.

- ^{7}Li(n, γ) and ^{19}F(n, γ)

As the results of neutron absorption reactions in ^{7}Li and ^{19}F, not only prompt γ rays but also the decay electrons are emitted after the long lifetime. Subtraction procedure is applicable to remove the background and that is described in Sec. 6.3.2.

- ^{12}C(n,γ) and ^{16}O(n,γ)
  Point-like backgrounds are generated by ^{12}C and ^{16}O which are derived from CO_2 gas. The reaction probabilities are about 3 times larger than that of neutron decay in our configuration of gas mixture. The energy deposit from γ rays are not always detected, though the kinetic energy of the recoil atoms are about 1 keV and that is sufficiently large to be triggered. Detailed description of analysis is given in Sec. 6.3.1.

4.2 (n,p) and (n,α) reactions

In the measurement of beam flux, main source of backgrounds are derived from neutron capture reactions. As for capture reactions of slow neutron, it is well known that the cross section is proportional to the inverse of the neutron velocity. In NOP experiment, the velocity of chopped neutrons are in the range between 500 m/s to 1200 m/s and they are sufficiently slow for satisfying the $1/v$ law. Following backgrounds are result from neutron capture reactions.

- ^{6}Li$(n,\alpha)^{3}$H
  This reaction have the order of magnitude larger cross section than that of (n,γ) reactions in the LiF tiles. Because of that, ^{6}Li is commonly used to prevent the generation of γ rays. However, large amount of ^{3}H is generated and that would produce another background, the decay electron. That is detailed in Sec. 4.4.

- ^{14}N$(n,p)^{14}$C
  ^{14}N is derived from the outgas and it gradually increases with the elapsed time. The common feature of ^{14}N$(n,p)^{14}$C and ^{3}He$(n,p)^{3}$H is that they have large and local energy deposit. Therefore, ^{14}N$(n,p)^{14}$C can not be separated from ^{3}He$(n,p)^{3}$H at usual operation. In order to evaluate the amount of ^{14}N, we insert the measurements with low gain operation. That is described in Sec. 6.4.1

- ^{17}O$(n,\alpha)^{14}$C
  ^{17}O is mainly coming from quenching gas. This reaction can not be distinguished from ^{3}He$(n,p)^{3}$H as it is the same with the capture reaction in ^{14}N. The number of ^{17}O$(n,\alpha)^{14}$C events will be estimated in Sec. 6.4.1.

4.3 Neutron scattering

Neutron scattering is often followed by (n, γ) reactions in the LiF tile. In order to separate signal and backgrounds, we make a demand for signal events not to include neutron scattering so that once neutron is scattered, it is treated as the background. From this definition, one of the significant features of signal is provided that the starting point of the track in signal events are limited to the on-axis region. Here we define the on-axis region as the cross section of the beam which correspond to $2 \times 2\,\mathrm{cm}^2$ in xy plane. Therefore, it is important to take scattering probabilities and kinematics under advisement. Since scattering itself can not be measured directly, the cross sections and momentum are calculated based on [38,39] and the theoretical treatment of neutron scattering caused by ^{4}He and CO_2 gases are considered.

In the cold neutron physics, the wavelength of neutron is long compared with the interval between atoms, that result in the neutron show a wave nature. For the accurate treatment of neutron scattering, the thermal motions and the structure of gas molecules have to be taken into account. To avoid enormous cost of calculation, semiclassical approximation was introduced in [38], where a neutron is represented by a wave and the molecule is replaced by a rigid system of point scatterers. The differential cross section of neutron scattering is derived from Eq. (4.1).

$$\sigma(\theta) = \frac{1}{4\pi}\left(\frac{M}{M+1}\right)^2 \sum_i \sum_j (\sigma_j \sigma_i)^{\frac{1}{2}} \frac{\sin x_{ij}}{x_{ij}}, \tag{4.1}$$

where θ is the scattering angle in the center of mass system, M is the ratio of the masses of the molecules and neutron, and σ_i is the total bound scattering cross section of the nucleus i if $i = j$, otherwise it is the coherent cross section. And x_{ij} is given by

$$x_{ij} = (4\pi r_{ij}/\lambda) \sin(\theta/2), \tag{4.2}$$

where r_{ij} is the distance between the atoms i and j, and λ is the wavelength. Note that this calculation is performed in the center of mass system and transformed to the laboratory system. The initial neutron velocities are derived from the standard velocity of neutrons in each bunch, while a maxwellian distribution at room temperature have been adopted to the relative velocity of the gas molecules.

The result of calculation is shown in Tab. 4.1. The scattering cross section of CO_2 is about 10 times larger compared with that of ^{4}He, though considering the number density of the gas moleclues, the probability of neutron scattering in each gas is comparable. Figure 4.1 shows relation between the neutron velocity after scattering and the scattered angle.

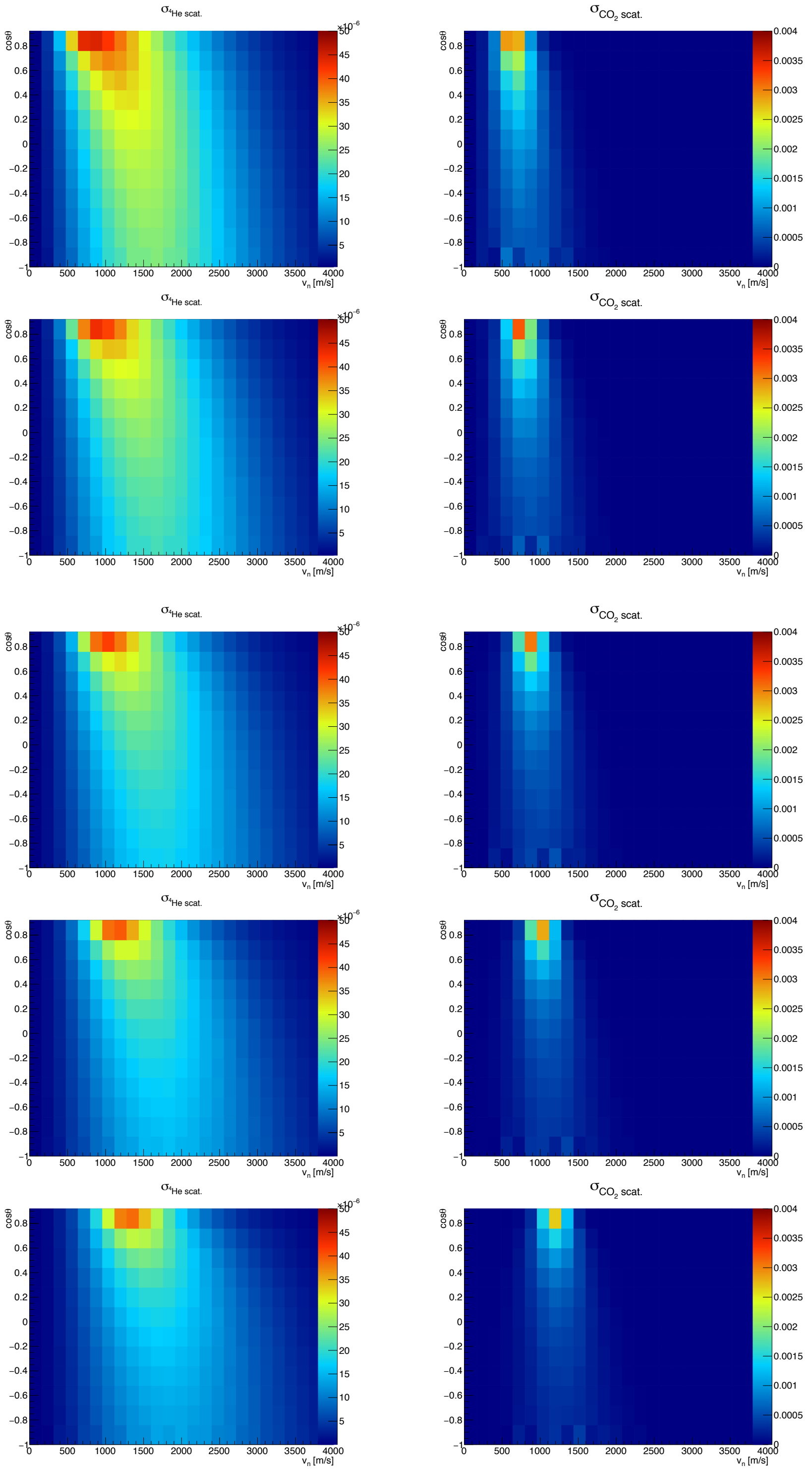

Figure 4.1: Cosine of scattered angle vs. neutron velocity after scattered by ^{4}He (left) and CO_2 (right). The standard neutron velocity in each bunch was assumed for the initial neutron velocity at 304 K. From the top, the initial velocity is 598, 709, 843, 997 and 1177 m/s.

v_n [m/s]	$\sigma_{^4\mathrm{He}}$ [barn]	σ_{CO_2} [barn]
598	1.97	16.6
709	1.71	18.7
843	1.51	21.2
997	1.34	24.0
1177	1.22	27.0

Table 4.1: Theoretically calculated neutron scattering cross sections at 304 K. Here, v_n is the initial neutron velocity.

4.4 ^{3}H decay

^{3}H decay is not a direct reaction of neutron but neutron is related to the production of ^{3}H via ^{6}Li$(n,\alpha)^3$H and ^{3}He$(n,p)^3$H reactions. ^{3}H decay is expressed as follows:

$$^3\mathrm{H} \to {}^3\mathrm{He} + e^- + \bar{\nu_e} + 18.6\,\mathrm{keV}. \tag{4.3}$$

Even though ^{3}H have long lifetime ($\tau = 12\,\mathrm{y}$), considerable amount of ^{3}H are generated because the LiF tiles are incessantly exposed to neutrons and the decay electron from ^{3}H can not be ignored. Some studies about the diffusion of ^{3}H from LiF are given in [40, 41].

By clarifying the following features, we have concluded the existence of the decay electron from ^{3}H. Firstly, point-like backgrounds have been detected across the TPC. Secondly, the rate of the background is proportional to the beam flux and it gradually increases with the amount of irradiation. When irradiation is interrupted, the rate also becomes constant. Thirdly, the source of the background is limited in the downstream of the Zn foil, and the lifetime of the background is more than one week. Fourthly, the rate of the background have been reset by the operation of a new gas filling.

The background can be extracted by applying a cut, where we introduce a parameter "ph/int" and the definition is described in Sec. 6.3.1. Figure 4.2 shows the energy deposit of the background. Although the sensitivity of the cut is limited to energy deposit less than 15 keV, due to saturation of pulse height. The broad distribution of energy deposit appears in the MC sample of ^{3}H decay as shown in Fig. 4.3, and that can not be explained by the interactions of other materials surrounding TPC. Consequently, the background is well suppressed by the cut as demonstrated in Fig. 4.4.

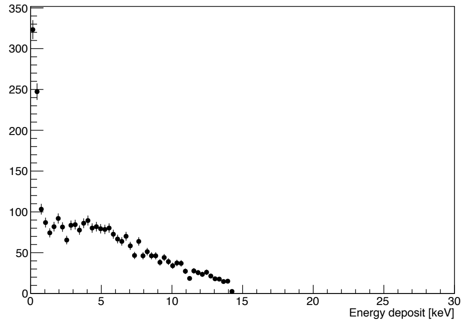

Figure 4.2: Energy deposit of the point-like background events extracted from data.

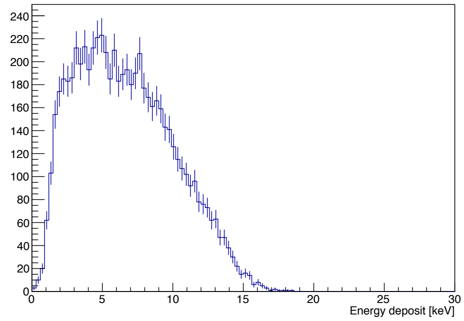

Figure 4.3: Energy deposit of the MC sample of ^{3}H decay.

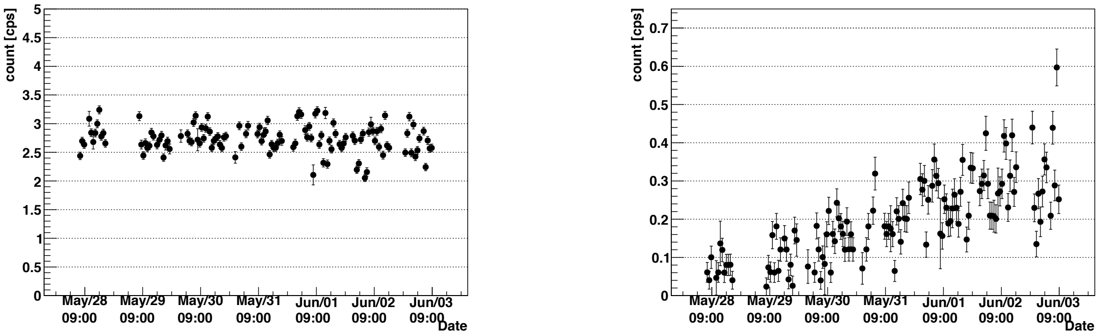

Figure 4.4: Transition of the count rate of neutron decay candidates with ^{3}H suppression cut (left) and the count rate of the background extracted by ^{3}H suppression cut (right). The accelerator was operated with constant beam power during the measurement.

Assuming that 100 % detection efficiency of the TPC at 150 kW operation, the generation of ^{3}H is expected to be 9×10^4 cps and it is estimated that 1/200 of them are released to be detected.

4.5 Categorization of signals and backgrounds

In the previous sections, we enumerated possible neutron interactions with materials surrounding TPC. Signals and backgrounds are categorized as summarized in Tab. 4.2. MC simulation of these reactions will be detailed in chapter 5. The analysis have been developed to adopt each background and that will be explained in chapter 6.

	Neutron decay	Beam flux
Signal	Neutron decay without scattering	^{3}He$(n,p)^3$H without scattering
Background	Neutron decay after scattering (n,γ) reactions ^{6}Li$(n,\alpha)^3$H	^{3}He$(n,p)^3$H after scattering ^{14}N$(n,p)^{14}$C ^{17}O$(n,\alpha)^{14}$C

Table 4.2: Categorization of signals and backgrounds.

Chapter 5

Simulation

Signal efficiency and the amount of neutron induced backgrounds are estimated by using MC simulation. The reproducibilities of the cut parameters are matters of critical importance.

5.1 Overview of simulation

The construction process is separated into two parts. In the former, the distribution of energy deposit inside the TPC is calculated based on GEANT4 simulation [42]. General physics process in gas detector such as diffusion, recombination and attenuation are considered in the latter. As the result of process, we obtain waveforms of all wires as it is the same with the measurement.

Part1 : Production of ionized particles

- Physics model and cross section
- Beam structure
- Energy spectrum of prompt γ ray
- Neutron polarization
- Ionization

Part2 : Statistics of ionized partilces

- Diffusion
- Recombination
- Attenuation

- Induced electrical field
- Space charge effect
- Production of waveform

5.1.1 List of the MC samples

The list of MC samples is tabulated as below. It is not efficient to trace all the tracks of neutrons because the probability of neutron decay is very low (10^{-6}) and the cost of calculation become too large. To avoid such situation, the position of neutron interactions were determined beforehand as described in Sec. 5.2.2. Then, GEANT4 simulation is started by tracing the reaction products. The statistics of MC sample is about 10 times larger than that of data.

Sample	Initial particles
Neutron decay (signal)	neutron
Neutron decay (background)	neutron
^{3}He$(n,p)^3$H (signal)	p and ^{3}H
^{3}He$(n,p)^3$H (background)	p and ^{3}H
LiF capture	photon
CO_2 capture	recoil atom and photon
Cosmic ray	$\mu^{\pm}$
^{55}Fe source	photon

Table 5.1: List of the MC samples.

5.2 Production of ionized particles

In the former part of the simulation, geometrical tracking was performed with consideration of the capture reactions and the inelastic reactions, based on GEANT4 physics model. Finally, whole energy deposit from the reaction products are recorded. Full structure of the detectors and shields have been implemented to the simulation.

5.2.1 GEANT4 physics model

In the GEANT4 simulation, it is possible to customize the library to optimize calculation according to particles and range of energy. We employ two kinds of physics lists called

"QGSP_BERT_HP" and "FTFP_BERT_PEN" where neutron capture reaction and inelastic interaction are taken into account.

QGSP_BERT_HP

The physics lists of this library use the "NeutronHP" model which dedicate to the neutron interactions in the energy range of below 20 MeV. The neutron capture reactions and the absorption reactions can be simulated. Note that this library was used only when we trace scattered neutrons and that is described in Sec. 5.2.3.

FTFP_BERT_PEN

FTFP_BERT_PEN is suitable for the calculation of low energy electrons and photons which are dominant particles produced in the ionization chamber. Most of our simulation is started with the generation of reaction products, and therefore FTFP_BERT_PEN was selected. It should be noted that the calculation concerned with the angular distribution of neutron decay products, the neutron scattering and the energy spectrum of prompt γ rays from the LiF tile were originally implemented to deal with the interactions of cold neutron in correct manner. As for the neutron decay described in G4NeutronBetaDecayChannel.hh, the decay products were incorrectly emitted on the same plane, so that we corrected the relative relationship of angles in the program. In the neutron scattering, G4NeutronHPElastic.hh deal with only the scattering by free atoms at a given temperature. For the proper treatment of low energy neutron scattering, thermal motion and structure of the gas molecules have to be considered. We calculated the scattering cross section on the basis of [38] and input to the simulation (see Sec. 4.3).

5.2.2 Beam structure

The reproduction of the beam structure is significant for the evaluation of those backgrounds induced from neutron scattering since the key features of signal are provided by identifying the starting point of the track. Three dimensional position is reproduced as following. The energy deposit of $^3\mathrm{He}(n,p)^3\mathrm{H}$ reaction is very localized so that it provides good information of the passage of neutrons as shown in Fig. 5.1, and the position in z direction versus TOF of $^3\mathrm{He}(n,p)^3\mathrm{H}$ reaction was input from data. While the xy distribution of the neutron was acquired from additional measurement which was arranged ahead of the physics data taking and the result was also input to the simulation (Fig. 5.2). The detail of measurement is described in appendix B.

In the passage of the decay volume (68 cm), the effect of diffusion in xy direction was measured to be not more than 1 mm and that is smaller than wire pitch (12 mm). In the simulation, it is assumed that the neutron pass along the z axis without changing the

xy distribution. In this way, three dimensional interaction points of neutron have been determined to generate the reaction products.

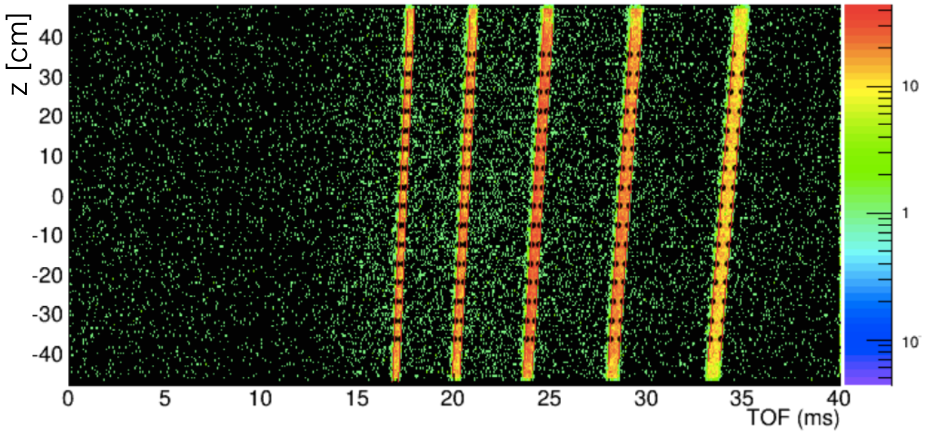

Figure 5.1: The center of energy deposit in z direction vs TOF, provided by extracting ^{3}He$(n,p)^3$H events.

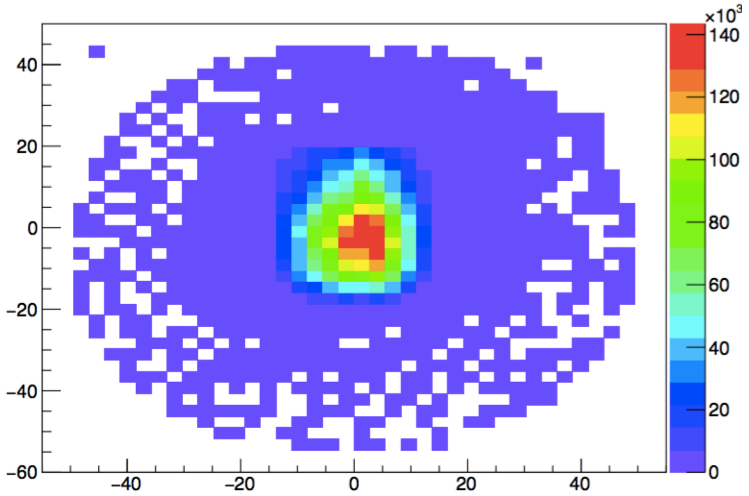

Figure 5.2: Beam distribution in the xy plane, measured with RPMT.

5.2.3 Capture reactions of scattered neutron

In order to simulate the reactions result from neutron scattering, we have to figure out the position of neutron scattering and that of capture reactions. The simulation was processed in two steps. Firstly, the position of scattering was determined. According to the mean free path, which was obtained from the cross section (see Sec. 4.3), scattering position in z direction can be calculated. To beware that xy distribution of the scattering coincide with Fig. 5.2. The momentum distribution of the scattered neutron is acquired from Fig.4.1 and the preparation to simulate the track of scattered neutron have done.

Secondly, another simulation was carried out to calculate the position of neutron capture reactions. Based on previously calculated momentum and the position of scattering, scattered neutron was emitted and then ${}^{6}\mathrm{Li}(n,\alpha){}^{3}\mathrm{H}$ and ${}^{3}\mathrm{He}(n,p){}^{3}\mathrm{H}$ events were identified by tagging both of physics process and the reaction products. In this way, the position of capture reaction was projected into two kinds of maps, one for the capture reaction in the LiF tiles and another for ${}^{3}\mathrm{He}(n,p){}^{3}\mathrm{H}$ reaction. The maps are shown in Fig. 5.3. Because of the long mean free path of the neutron decay and ${}^{3}\mathrm{He}(n,p){}^{3}\mathrm{H}$ reaction compared with the decay volume, it is assumed that position of these two reactions have similar distribution.

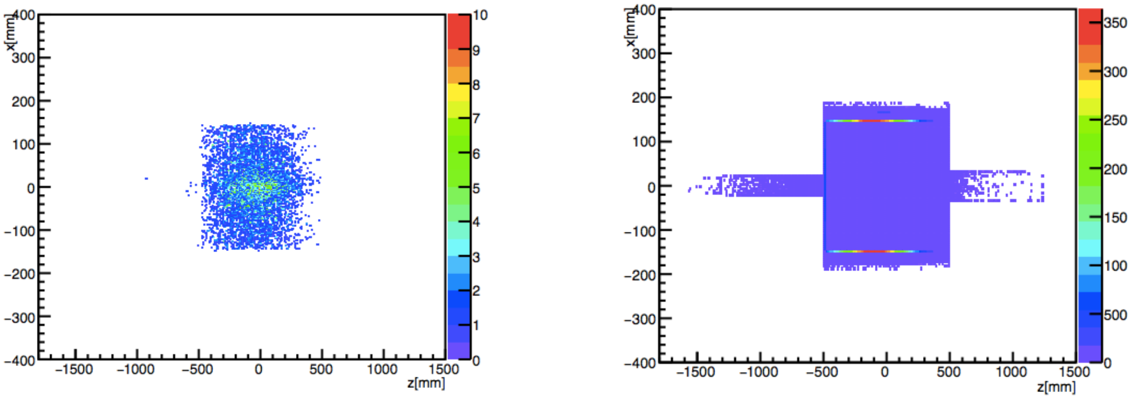

Figure 5.3: Position of ${}^{3}\mathrm{He}(n,p){}^{3}\mathrm{H}$ reaction after neutron scattering (left) and that of ${}^{6}\mathrm{Li}(n,\alpha){}^{3}\mathrm{H}$ reaction (right), shown in xz plane.

5.2.4 Energy spectrum of prompt γ rays from the LiF tile

The energy spectrum of prompt γ rays from the LiF tile depend on the component of LiF tile and neutron velocity, so that it is preferable to obtain the spectrum from data. The measurement was conducted with the cooperation of the neighboring beamline, BL04 [54–56]. The LiF tile which have been used in the NOP experiment was brought to the BL04 and irradiated to measure the energy spectrum. The γ rays were detected by a set of germanium photon detectors and the intensity of γ rays was reconstructed as shown in Fig. 5.4. The detail of measurement is given in appendix C.

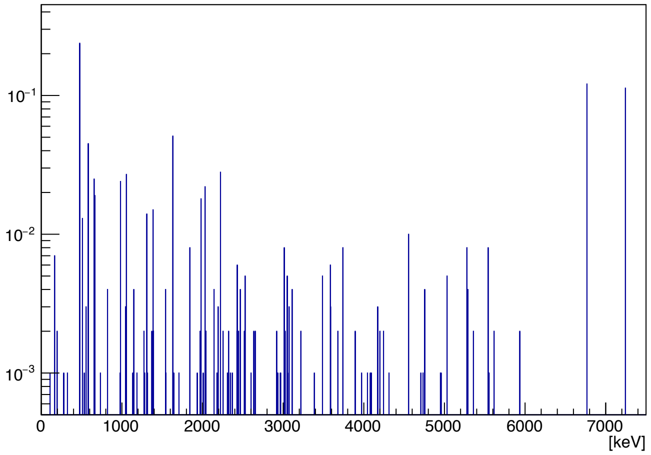

Figure 5.4: Energy spectrum of γ rays emitted from the LiF tile. Intense peaks found at 477 keV, 6768 keV and 7245 keV are derived from ^{6}Li.

5.2.5 Neutron polarization

The angular distribution of the decay electron depend on the polarization of neutron and it may slightly contribute to the detection efficiency. The probability to emit the electron with an angle θ with respect to the neutron spin is written as follows [8].

$$W(E_e, \theta) \propto 1 + \beta P A \cos\theta, \tag{5.1}$$

where A is the angular correction between the neutron spin and the electron, and A has been measured to be -0.1184(10) [5]. β is the speed of the electron relative to the speed of light, P is the neutron polarization and E_e is the energy of the electron.

Although polarized neutron beam is provided in the upstream, the magnetic field is required to keep the polarization and that is limited to around SFC. The neutron spin might be affected by the geomagnetism, and therefore the polarization is not sure. However, it should be noted that our TPC is able to detect ionization tracks in a 4π geometry. For these reasons, the effect of polarization is considered to be very small and we deal with depolarized neutron in the simulation. The uncertainty in the detection efficiency was estimated with the MC sample of polarized neutron decay, which was prepared only for this estimation, resulted in 0.13 %.

5.2.6 Ionization

Charged particle leave the trace of passage when it passes through a gas chamber. This is the result of ionization that ionized particles are left by the collision between the charged particles and gas molecules. Ionized particles drift toward to MWPC according to the electric field, and the energy deposit which is proportional to original ionization is detected after amplification. The amount of ionized particles depend on W-value which is the effective average energy for the production and differs by the gas molecule as shown in Tab. 5.2. W_β of ^{4}He and CO_2 were weighted based on the partial pressure, and we apply 40.9 eV in the simulation.

Gas	W_α [eV]	W_β [eV]	I [eV]
^{4}He	46.0	42.3	24.58
CO_2	34.3	32.8	13.81

Table 5.2: W-value of TPC gas [44]. W_α and W_β are average energy required to produce an α particle and an electron, respectively. I is the minimum ionization potential.

For a charged particle with low energy, it is known that W-value is increased and therefore the energy deposit of the proton in the neutron decay might be overestimated in the simulation. The lower limit of the detection efficiency can be estimated by simulating the situation that only the energy deposit from the decay electron could be detected. The uncertainty was calculated to be 0.35 %. The same thing can be said about $^{12}C(n,\gamma)^{13}C$ reaction and $^{16}C(n,\gamma)^{17}O$ reaction, because only small portion of energy is shared with the recoil atom ($E_{^{13}C} = 1.01\,\mathrm{keV}$ and $E_{^{17}O} = 0.54\,\mathrm{keV}$) [45]. Although the energy deposit of ^{13}C and that of ^{17}O would be slightly enlarged and they are more likely to be detected in our simulation, 99.9 % of them are discriminated by applying a cut.

5.3 Statistics of ionized partilces

In this section, the latter half of the simulation is detailed. After ionized particles have been traced, they will be converted into waveforms and the main point of this section is to calculate the gain and the attenuation of charges as they drift toward MWPC.

5.3.1 Diffusion

During the drift in the electric field, electrons are diffused by collisions with gas molecules. The proportion of the electrons in the dx is given by Eq. (5.2).

$$\frac{dN}{N} = \frac{1}{\sqrt{4\pi Dt}} \exp\Big(-\frac{x^2}{4Dt}\Big) dx, \tag{5.2}$$

$$\sigma_x = \sqrt{2Dt}, \tag{5.3}$$

where x denote the distance from the origin after time t, D is diffusion coefficient which is determined to reproduced the measurement, and σ_x is the diffusion width. In the simulation, t is calculated by the y positions of the ionized particles and eventually primary electrons are diffused at a distance of σ_x.

5.3.2 Recombination

Recombination affect to diminish the ion pairs. There are some possibilities for a positive ion and an electron to be neutralized. For example, one would be recombined with ionized particles or extracting an electron at the walls. While stronger electric field help to suppress these effect, the electric field of 300 V/cm have been applied in our experiment and the measurement of the probability of recombination resulted in 12 %. The detail is studied in [44]. The effect of recombination is implemented in the simulation as the expression confirming poisson distribution, where the mean value is proportional to the number of original ion pairs.

5.3.3 Attenuation

The electrons are attached to gas molecules, result in the reduction of detected electrons. This influence of attenuation depends on the number of collisions with gas molecules. Therefore, as it is empirically tested that attenuation is enhanced by the amount of outgas, slower drift velocity, higher gas pressure and longer drift length (Fig. 3.30). The effect of attenuation can be expressed by poisson distribution in which the mean value is proportional to the drift length.

$$\Delta N = N(1 - e^{-\frac{\Delta y}{\lambda}}) \sim N\frac{\Delta y}{\lambda}, \tag{5.4}$$

where ΔN is the amount of reduced charge, N is the number of original ion pairs, Δy is drift length and λ is the inverse of attenuation coefficient.

5.3.4 Amplification and avalanche-induced electric field

In the basic operation of proportional wire, electrical field is expressed as

$$E = \frac{q}{2\pi\epsilon_0}\frac{1}{r}, \tag{5.5}$$

where q is the charge density, ϵ_0 is the dielectric constant for the gas and r is the distance from center of the wire. Electric field is rapidly increased as an electron approaches to anode wires and it will obtain enough energy to induce secondary ionization. In this way, avalanche is started and detected energy is proportional to the amount of collected electrons.

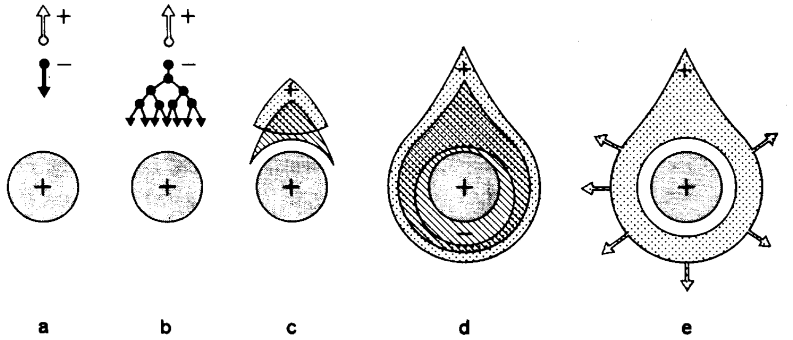

Figure 5.5: Time development of an avalanche in a proportional counter [35]. A pair of ionized particle is created (a). Secondary ionization is induced on the way toward to the anode wire (b) and laterally diffused (c). As the development of an avalanche, the wire is surrounded by electrons (d). The electrons are rapidly collected and positive ions are attracted to the cathode wire (e).

With continuous development of avalanche, it induces electric field. The effect is not limited in the single wire but also extend to neighboring wires and inverse pulses are produced. The avalanche-induced electric field was simulated by using ANSYS ver 15.0 [46] and Garfield [47]. First, three dimensional electric field was calculated based on the finite element method (FEM) by using ANSYS. To reduce the calculation costs, the repeat structure of the wires was simplified to unit structure. The result was input to Garfield and multiplication of charge was simulated. Based on the Shockley-Ramo theorem [49], the current which is induced by the movement of charge is expressed as follows.

$$i = qvE_v, \tag{5.6}$$

here v is the velocity of charged particle and E_v is the magnitude of electric field parallel to v. There is no difference in the time structure between the induced current and the original current. Consequently, the effect can be taken into account by calculating the ratio of the induced current and scale factor was introduced to the simulation.

5.3.5 Space charge effect

The influence of space charge effect is observed when high density of positive charge cover the wire. It can be seen in $^3\text{He}(n,p)^3\text{H}$ reaction because the energy deposit of the proton is large and localized. The wire is surrounded by positive ions, result in the decline of the electric field. It means that the wire is not maintaining the proportionality and the energy deposit will be underestimated. The electric field will recovered after all ions are collected in the cathode wire and it takes about a few µs. This effect is taken into account by applying following model of saturation [36].

$$s = \frac{\log\left(1 + f(\phi)\Delta E G_0\right)}{f(\phi)\Delta E G_0}, \tag{5.7}$$

where $f(\phi)$ represent the amplitude of saturation, ϕ is the angle of the track to x axis, ΔE is deposited energy in the wire, G_0 is multiplication factor for the condition without space charge effect. The reduction of s means the suppression of the amplification. Figure 5.6 shows the saturation factor s measured by using ^{241}Am source. Data was fitted by arbitrary scale to obtain the parameter f and ΔE.

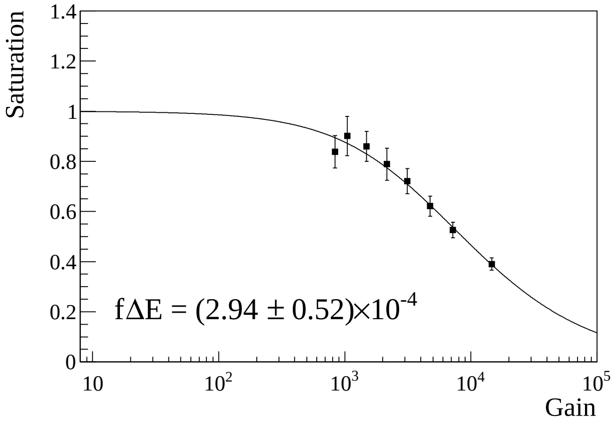

Figure 5.6: Measurement of the saturation factor s as a function of gain by using ^{241}Am source [36]. The vertical scale was normalized to $s(G_0 = 0) \to 1$.

5.3.6 Production of waveform

In the previous section, we considered when and how many charges have been collected in each wire and we obtained the charge density which is formulated as a function of time. Besides, the template waveform was measured with the checking source (Fig. 5.7).

A waveform is produced by convoluting the charge density function with the template waveform:

$$F(t) = \begin{cases} 0 & (0 \leq t \leq 298) \\ \int_0^{t-299} N_e(\tau) T(t-\tau) d\tau & (299 \leq t \leq 1000) \end{cases}, \tag{5.8}$$

where $F(t)$ is the produced waveform at time t, $N_e(t)$ is the function of charge density, $T(t)$ is the template waveform. Finally, the pedestal noise is added to obtain the detected waveform.

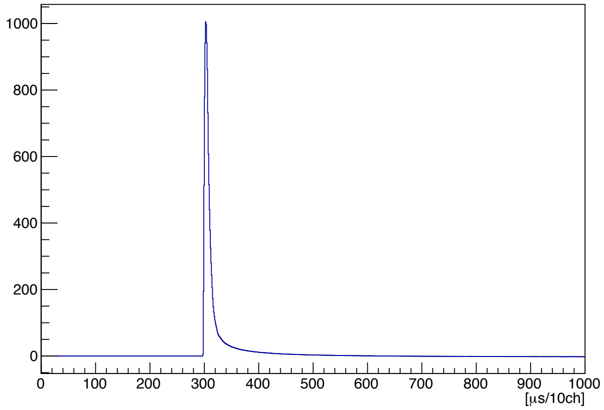

Figure 5.7: Template waveform measured by using the X-ray source.

Part III

Analysis

Chapter 6

Signal estimation

In this chapter, the evaluation of number of signal events are described. Our basic concept of signal estimation is that the backgrounds are removed from all events rather than extracting the signal events. By this means, we have to solve three issues to count the neutron decay and the ^{3}He$(n,p)^3$H reaction.

- Separate neutron decay and ^{3}He$(n,p)^3$H reaction.
- Remove backgrounds as many as possible.
- Correct remaining backgrounds.

The critical points in the analysis are the improvement of signal-to-noise ratio and correct treatment of the uncertainties.

6.1 Overview of the analysis

We will follow the procedure shown in Fig. 6.1 to evaluate signal events. The first process of the analysis is to separate all events into the neutron decay candidates and the ^{3}He$(n,p)^3$H candidates. A parameter is defined to discriminate signal events as detailed in Sec. 6.2.

Next is to remove the backgrounds. The methods of background reduction significantly affect both of statistical and systematical errors. The backgrounds are removed from the signal candidates depending on their features, step by step. This process is described in Sec. 6.3. Finally, some corrections are applied to estimate remaining backgrounds which can not be measured directory. These are performed by using MC simulation as demonstrated in Sec. 6.4.

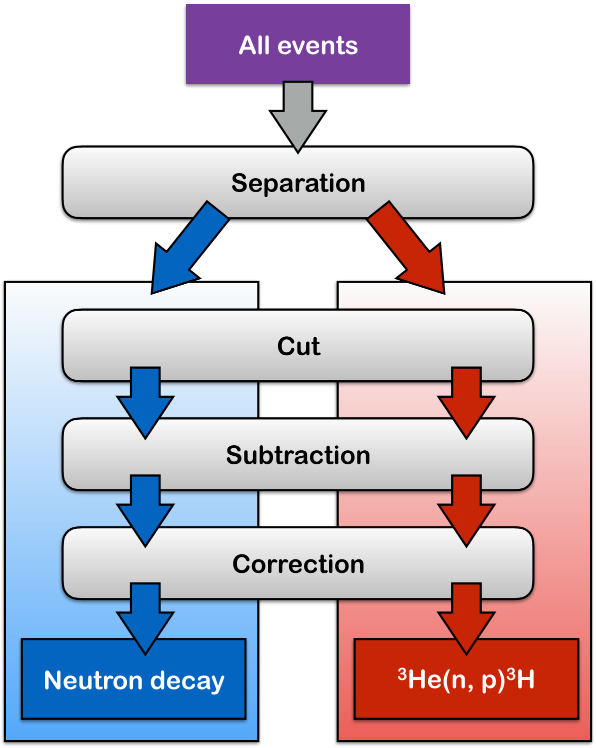

Figure 6.1: Analysis flow of the signal evaluation.

Data set

The configurations of engineering data and physics data are summarized in Tab. 6.1. The accumulated data correspond to 12 days of beam time.

Series	Beam power [kW]	DAQ [day]	^{3}He density [$\times 10^{19}$ atom/m^3]
1 (May 2014)	240	1.4	2.24(1)
2 (Apr. 2015)	430	0.7	1.867(5)
3 (Apr. 2016)	170	0.8	2.127(7)
4 (Apr. 2016)	170	3.0	3.96(1)
5 (May 2016)	170	2.8	0.993(4)
6 (Jun. 2016)	160	3.0	2.089(7)

Table 6.1: Acquired data set.

Data have been accumulated with following cycle, basically with high gain operation ((a)∼(d)). In order to estimate the amount of ^{14}N derived from the outgas, low gain measurement ((e), (f)) was inserted about four times per gas filling.

(a) Beam ON

(b) Beam OFF

(c) ^{55}Fe source

(d) Cosmic ray

(e) Beam ON with low gain operation

(f) Beam OFF with low gain operation

6.2 Separation of neutron decay and $^{3}\mathrm{He}(n,p)^{3}\mathrm{H}$ reaction

At first, we have to separate the neutron decay candidates and the $^{3}\mathrm{He}(n,p)^{3}\mathrm{H}$ candidates because both reactions are measured in the same volume of detector. The characteristic of the neutron decay is long track of the electron starting from the on-axis region. On the other hand, large and local energy deposit of the proton is detected in the $^{3}\mathrm{He}(n,p)^{3}\mathrm{H}$ reaction. Therefore, the different ionization power provide the discrimination with good performance.

The waveforms of anode wires and cathode wires were recorded in the experiment by ILL-ISN-LAPP collaboration, while the field wires are also read out in our experiment and that help to increase the accuracy of separation. Here, we define the maximum single pulse height among all field wires as the parameter to separate the candidates. This parameter is able to reflect the amount of energy deposit and its reach. The performance is demonstrated in Fig. 6.2.

There are two kinds of uncertainties arise from this procedure. One is $^{3}\mathrm{He}(n,p)^{3}\mathrm{H}$ contamination in the neutron decay candidates. That is more serious than reverse contamination since the identification of the neutron decay is more complex. Furthermore, the probability of $^{3}\mathrm{He}(n,p)^{3}\mathrm{H}$ reaction with the ^{3}He admixture of 1 ppm at atmospheric pressure is about 25 times larger than that of the neutron decay. For these reasons, the threshold of 25 keV was adopted to minimize $^{3}\mathrm{He}(n,p)^{3}\mathrm{H}$ contamination. The detail discussion is given in Sec. 6.4.

Another uncertainty comes up to the signal efficiency due to the ambiguity of the parameter and that is estimated in chapter 7.

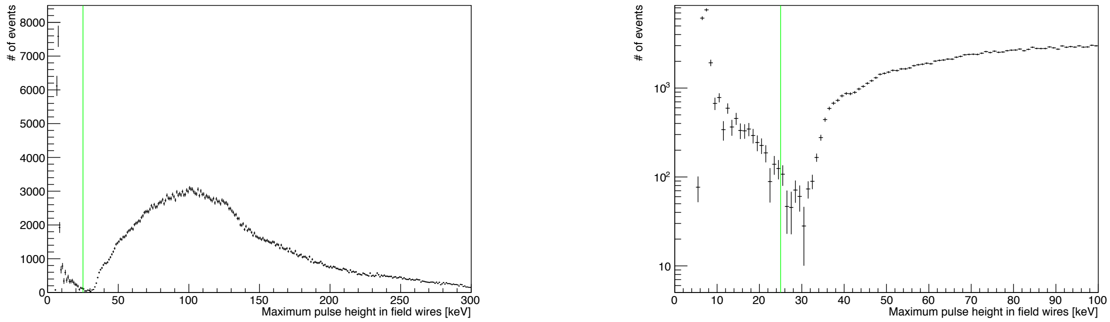

Figure 6.2: Maximum pulse height in the field wires. Left : Signal candidates are separated at 25 keV, which is indicated with green line. Right : Enlarged view of the left figure with logarithmic scale.

6.3 Background reduction

The backgrounds should be removed or corrected, otherwise the number of signal events would be overestimated. Although we can rely on a statistical subtraction of the residual backgrounds, we should not depend on it too much because it is not effective way to reduce statistical error, and therefore some cuts are applied before the subtraction. In the following, we will categorize the backgrounds and then focus on the practical approach.

Categorization of the backgrounds

The backgrounds can be separated based on the time structure and its sources (Figs. 6.3∼6.5). Firstly, the backgrounds are categorized into ones which are induced from neutron reactions and others. The ratio of latter backgrounds can be estimated by comparing "Beam ON" and "Beam OFF".

- Beam ON
  This measurement have been operated with the LiF shutter open and the neutrons beam pass through the TPC.
- Beam OFF
  The LiF shutter is closed, and neutrons are shut out by $^6\mathrm{Li}(n,\alpha)^3\mathrm{H}$ reaction.

Secondly, the backgrounds with different TOF structure are removed by subtracting "Sideband" from "Fiducial".

- Fiducial
  Fiducial time is defined as the time when a bunch is completely contained within 14 cm inner side than the edge of the drift cage. Because SFC is adjusted to shape bunches

with the interval of 3.2 m, next bunch is not yet formed in the upstream during the fiducial time.

- Sideband
  Sideband region is decided not to include the neutron bunches inside TPC, nor the events which are generated at the moment that proton beam hit the mercury target.

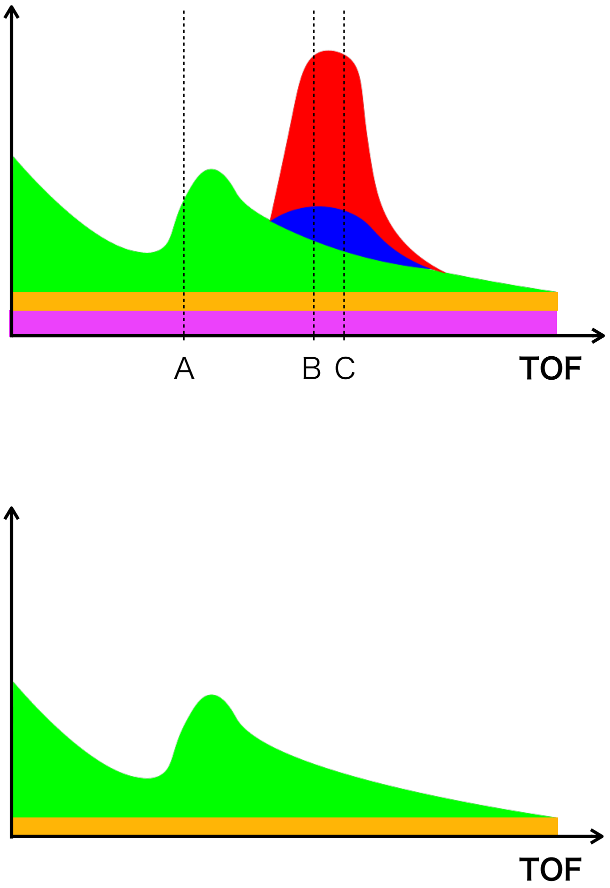

Figure 6.3: Drawing of TOF spectra of Beam ON (top) and Beam OFF (bottom). Signal events (red), the beam induced background (blue), the prompt γ rays from upstream (green), the environmental backgrounds (orange) and the radioactivation backgrounds (magenta) are illustrated. The time range from B to C roughly indicate the fiducial time.

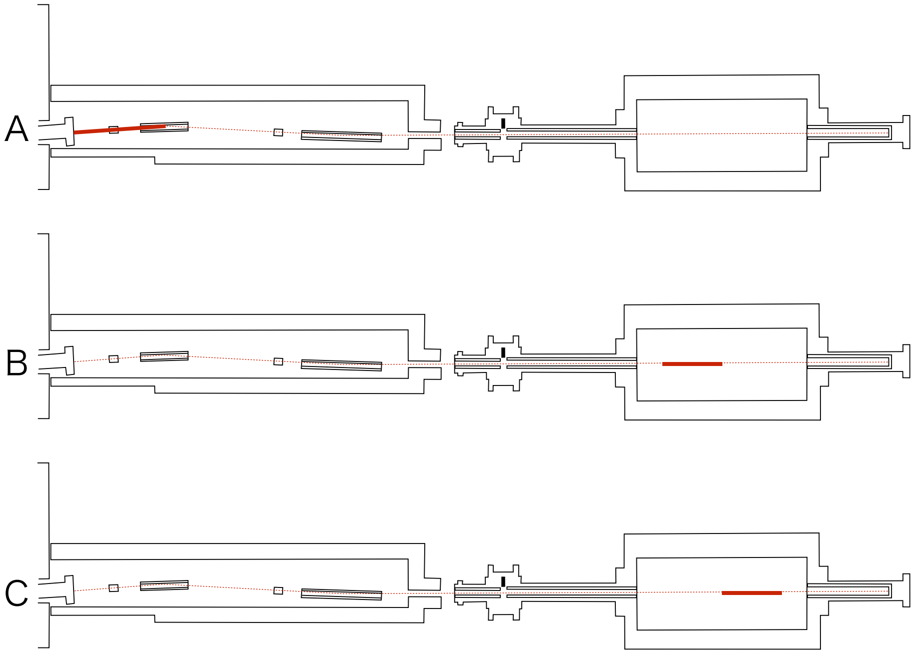

Figure 6.4: Passage of the neutron beam, which is indicated with red line, at a certain TOF of Beam ON. A, B and C are indicated in Fig. 6.3. The intense beam is emphasized with bold red line.

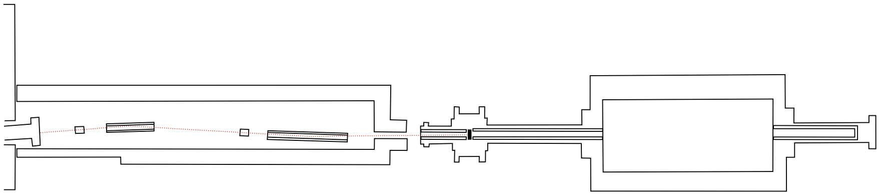

Figure 6.5: Passage of the neutron beam of Beam OFF. The neutrons are intercepted by the LiF shutter.

The definitions of Beam ON, Beam OFF, Fiducial and Sideband are represented by Fig. 6.6. Red and black histograms correspond to Beam ON and Beam OFF. Fiducial and Sideband are defined as shown with yellow bands and a green band, respectively. Beam OFF is subtracted from Beam ON, that result in the blue histogram with five peaks. The number of peaks indicate the number of bunches. Before the arrival of bunches, other five peaks are found in red and black histograms. These are caused by prompt γ rays and effectively removed by subtraction.

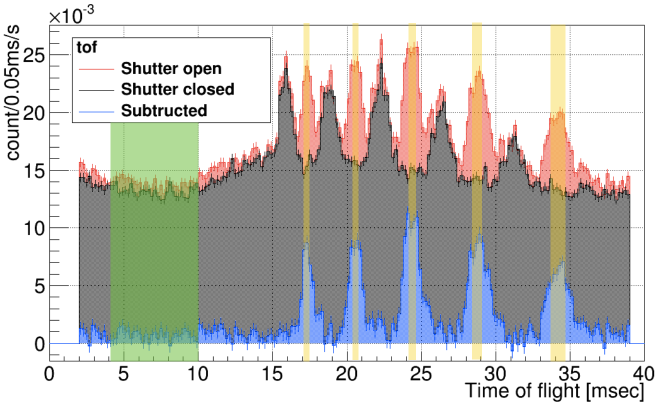

Figure 6.6: TOF of Beam ON (red), Beam OFF (black), and Beam OFF subtracted by Beam ON (blue).

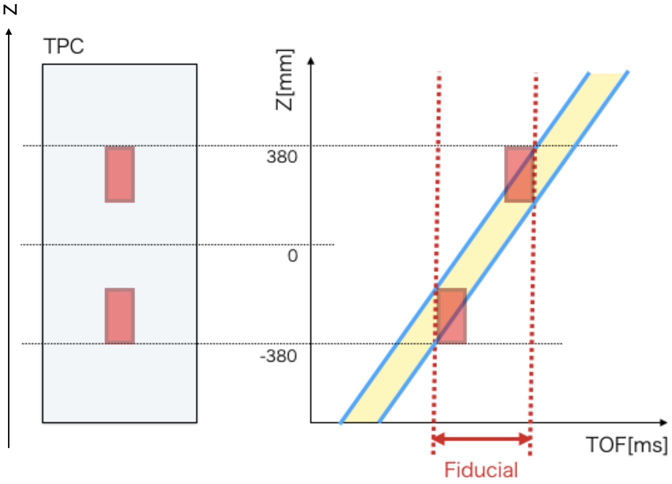

Figure 6.7: Definition of the fiducial time.

The passage of neutron bunch in the TPC is indicated in the center of energy deposit in z direction versus TOF (Fig. 5.1), and the fiducial region is determined as illustrated in Fig. 6.7. Although the fiducial time per kicker pulse corresponds to only about 2.3 ms, it much increases the signal-to-noise ratio. On the other hand, we have 6 ms of sideband per kicker pulse. Note that the slow neutrons, which have been generated by previous kicker pulse, continuously distribute in the outside of bunches due to the failure performance of SFC.

In this way, all events are categorized into ⓐ (Beam ON, Fiducial), ⓑ (Beam ON, Sideband), ⓒ (Beam OFF, Fiducial), ⓓ (Beam OFF, Sideband) and ⓔ others. ⓔ is not taken into account in the analysis. The backgrounds which are independent from the neutron interactions can be removed by Eq. (6.1).

$$(\textcircled{a} - \textcircled{b}) - (\textcircled{c} - \textcircled{d}) \tag{6.1}$$

Before we perform the subtraction, Beam OFF and sideband events are normalized to compensate the difference of beam flux and time width. After that, the remaining neutron induced backgrounds are corrected in Sec. 6.4.

6.3.1 Cut

Efficient reduction of backgrounds is achieved by introducing parameters to reflect their differentiation. Some parameters are described in the following. At first, a reference time is defined as the time when the first anode wire exceed the threshold. Then, the time window

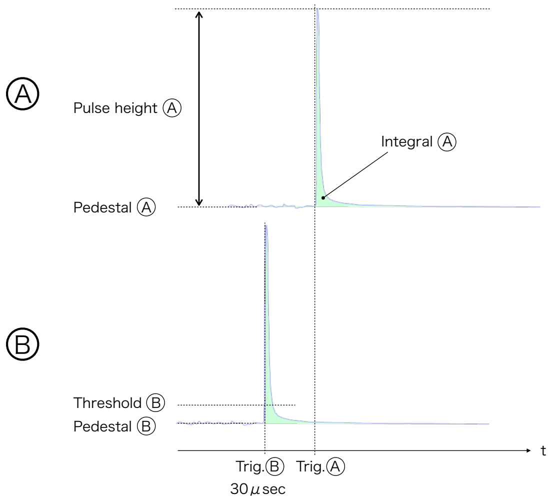

Figure 6.8: Definition of parameters. First and second triggered channels are illustrated.

with a width of 100 µsec is adjusted to set the reference time to be 30 µsec. Pedestal is calculated from the average of the pulse height within the range from 0 to 28 µsec, and it is employed as the reference point of the pulse height. The energy deposit is obtained by integrating the pulse height after 30 µsec. By using the X-ray events (5.9 keV) as the standard of the energy calibration, both of pulse height and integral are converted into energy.

Following cuts are applied to improve the purity of the neutron decay candidates.

- Fiducial TOF Cut
  The prompt γ rays from the magnetic super mirrors are greatly suppressed by limiting the TOF.

- Drift length $\leq 190\,\mathrm{mm}$
  Cosmic rays are not completely rejected by the veto scintillators because some of them pass through the gap between scintillators. Characterized by the long track goes through the TPC, the cosmic rays penetrate in y direction are well discriminated by adopting this cut. Drift length is calculated by the maximum time difference among triggered anode wires and the drift velocity.

- Energy deposit in the anode wires $> 5\,\mathrm{keV}$
  Point-like energy deposit are detected along with the beam axis, due to the neutron capture reactions in CO_2 gas. These events are discriminated by requiring the energy deposit to be more than 5 keV.

- ph/int < 0.8
  The ^{3}H decay background is removed by introducing the parameter "ph/int" which reflect the waveform features. ph/int is defined as the ratio of the maximum single pulse height to total energy deposit. When low energy deposit is detected, the pulse height will fit within the dynamic range of ADC. In this case, the waveform keep the same shape with the template (Fig. 5.7) and its height is proportional to the energy deposit. These events distribute ph/int of around 1.0 and this is just the case of the ^{3}H background. As for the neutron decay, ph/int is likely to be small because the electrons trigger many anode wires and the energy deposit come to large compared with the maximum pulse height. Although the background with the energy more than 15 keV are not removed by this cut due to saturation of ADC, they are able to be subtracted.

The performance of each cut is shown in Figs. 6.9 ∼ 6.14. For example, Fig. 6.9 shows the drift length of data. The red histogram is "Beam ON, Fiducial" and that includes signal events. Other histograms are "Beam ON, Sideband" (magenta), "Beam OFF, Fiducial" (blue) and "Beam OFF, Sideband" (cyan), where histograms are normalized by the beam monitor counts and TOF. The thresholds are indicated by green lines. All of four histograms are perfectly overlapping in the one side of the threshold. Obviously, this cut serve to reduce the background and also it is indicated that subtraction can fulfill its role. The remaining cosmic ray will be subtracted in Sec. 6.3.2.

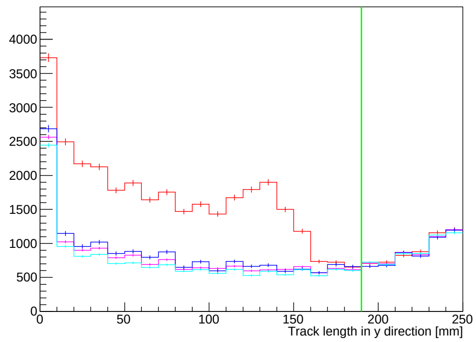

Figure 6.9: Comparison of the drift length among data before subtraction. Histograms are normalized by the beam monitor counts and TOF.

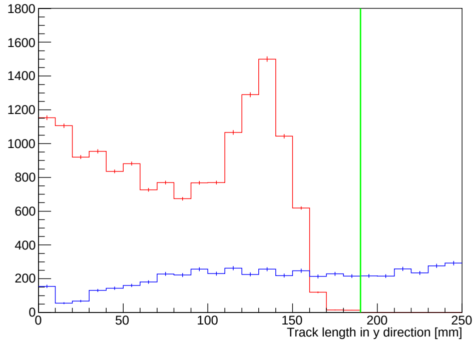

Figure 6.10: Comparison of the drift length between arbitrary scaled MC samples of the neutron decay (red) and cosmic ray (blue).

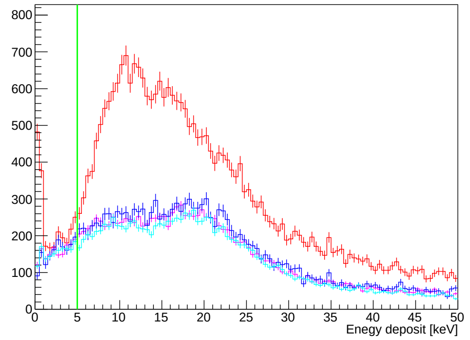

Figure 6.11: Comparison of the energy deposit among data before subtraction. Histograms are normalized by the beam monitor counts and TOF.

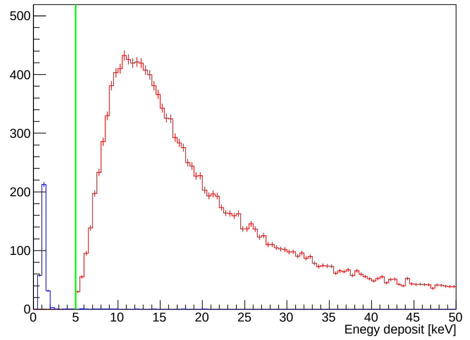

Figure 6.12: Comparison of the energy deposit between arbitrary scaled MC samples of the neutron decay (red) and the neutron capture reaction in CO_2 (blue).

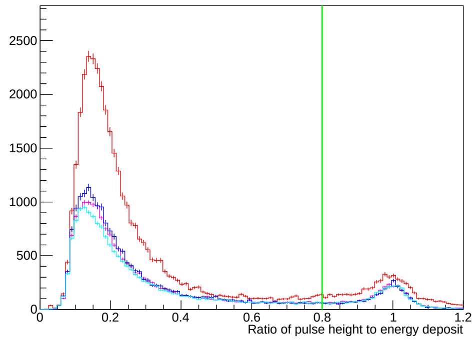

Figure 6.13: Comparison of ph/int among data before subtraction. Histograms are normalized by the beam monitor counts and TOF.

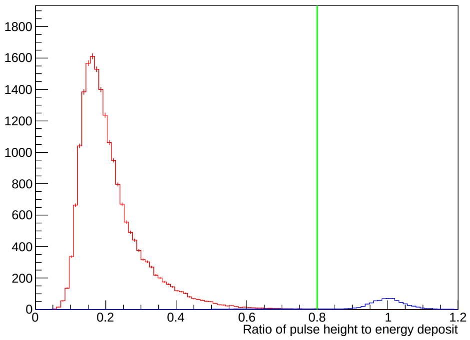

Figure 6.14: Comparison of ph/int between arbitrary scaled MC samples of the neutron decay (red) and the ^{3}H decay (blue).

6.3.2 Subtraction

The backgrounds with following characteristics are removed by the subtraction, “Fiducial - Sideband” and “Beam ON - Beam OFF”.

- Constant in time structure
- Not related to neutron reactions

Ones of former are the radioactivation backgrounds, such as ^{20}F decay ($\tau = 11.07\,\mathrm{s}$) and ^{8}Li decay ($\tau = 839.9\,\mathrm{ms}$), result from (n, γ) reactions:

$$\begin{aligned} {}^{20}\mathrm{F} &\rightarrow {}^{20}\mathrm{Ne} + e^- + \bar{\nu_e} + 7.02\,\mathrm{MeV}, && (6.2) \\ {}^{8}\mathrm{Li} &\rightarrow {}^{8}\mathrm{Be} + e^- + \bar{\nu_e} + 16.0\,\mathrm{MeV}. && (6.3) \end{aligned}$$

The rate can be consider to constant in time because they have long lifetime compared with the cycle of kicker pulse (40 ms). These backgrounds are removed by subtracting Sideband from Fiducial.

The other backgrounds are cosmic ray and the ^{3}H decay. Though some of them would be left behind due to the inefficiency of the cuts, they are well removed by subtracting Beam OFF from Beam ON. Figures 6.15 ∼ 6.17 show the results of subtraction and the simulation is normalized by the statistics of data. Compared with Figs. 6.9, 6.11 and 6.13, it is clear that the neutron decay is hardly eliminated and cuts are appropriate to increase the signal-to-noise ratio.

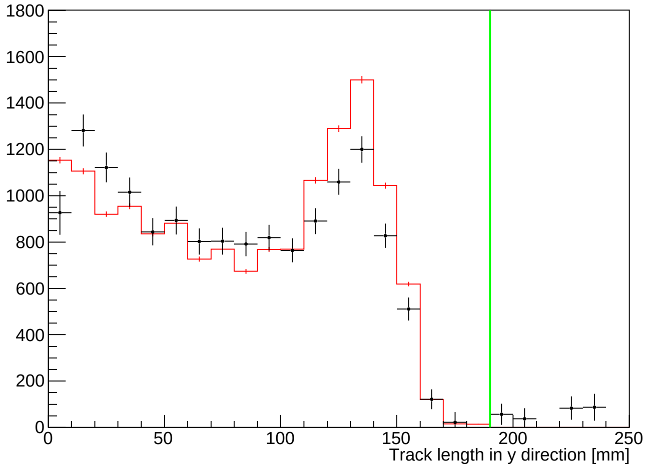

Figure 6.15: Comparison of the drift length between data after subtraction (black) and MC sample of the neutron decay (red) which is normalized by the statistics of data.

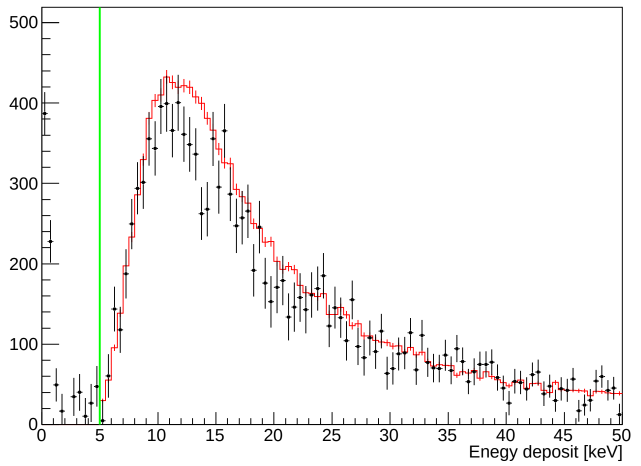

Figure 6.16: Comparison of the energy deposit between data after subtraction (black) and MC sample of the neutron decay(red) which is normalized by the statistics of data.

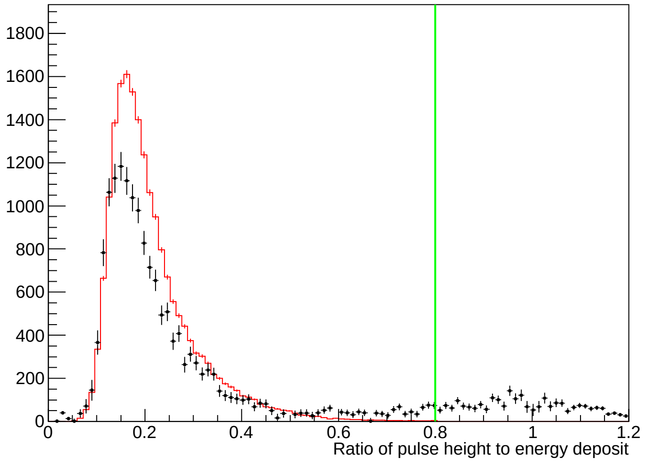

Figure 6.17: Comparison of ph/int between data after subtraction (black) and MC sample of the neutron decay (red) which is normalized by the statistics of data.

There would be an uncertainty arise from different LiF shutter condition of Beam ON and Beam OFF. When the shutter is open, more γ rays could pass through the shutter compared with the case of Beam OFF, and the γ rays might remain in the neutron decay candidates after the subtraction. The remaining γ rays are estimated by using Particle and Heavy Ion Transport code System (PHITS) [48] and GEANT simulation, and the uncertainty are included in the neutron lifetime.

6.4 Corrections

The remaining backgrounds are derived from the neutron interactions as described in chapter 4. We will enumerate possible backgrounds and make a correction respectively.

6.4.1 Corrections for the ^{3}He$(n,p)^{3}$H candidates

^{3}He$(n,p)^{3}$H candidates include followings.

- ^{3}He$(n,p)^{3}$H without neutron scattering (signal)
- ^{3}He$(n,p)^{3}$H after neutron scattering (background)
- ^{14}N$(n,p)^{14}$C

- $^{17}\mathrm{O}(n,\alpha)^{14}\mathrm{C}$
- Neutron decay
- Pileup of events

$^{3}\mathbf{He}(n,p)^{3}\mathbf{H}$ after neutron scattering

We will remove $^{3}\mathrm{He}(n,p)^{3}\mathrm{H}$ events which accompanied with neutron scattering. Note that $^{14}\mathrm{N}(n,p)^{14}\mathrm{C}$ and $^{17}\mathrm{O}(n,\alpha)^{14}\mathrm{C}$ reactions are not distinguishable from $^{3}\mathrm{He}(n,p)^{3}\mathrm{H}$ in high gain operation and they are not yet separated from signal events at this point. The key feature of the signal events is that the starting point of the track is concentrated in the on-axis region. In other words, only the backgrounds are distributed in the off-axis region.

The origin of the proton from $^{3}\mathrm{He}(n,p)^{3}\mathrm{H}$ is suitably reconstructed by a parameter "fce" which is defined as the center of energy deposit in the field wires as shown in Fig. 6.18. Where a single unit of fce corresponds to 12 mm. The MC sample of the background is scaled so as to offset the number of events in the off-axis region of the data, and the total number of background events have been estimated. In this estimation, the on-axis region is defined as $7\leq$fce<16 and it sufficiently covers the beam cross section. While the off-axis region is the complement of the on-axis region. Consequently, signal candidates are evaluated by subtracting the background from data.

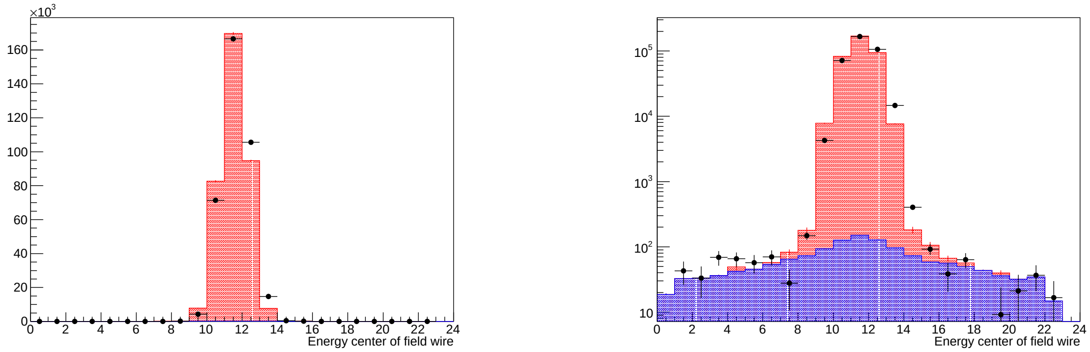

Figure 6.18: The center of energy deposit in the field wires, displayed with linear (logarithmic) scale in the left (right). Red and blue histograms correspond to the MC samples of signal events and neutron scattering background events. The center of TPC in x direction is fce = 11.5.

It is important to note that the number of backgrounds in the on-axis region was not derived from data driven approach. It just relies on the MC simulation resulted from theoretically calculated cross section, however the systematical uncertainty arise from the reproducibility of the MC sample of the background is not taken into account in this thesis. With advanced understanding of the backgrounds, the problem would be eliminated by including the scattered events as the signal. The probability of the neutron scattering is estimated from the ratio of the number of background events to that of signal.

Neutron decay

In the separation of signal candidates explained in Sec. 6.2, a certain percentage of the neutron decay events exceed the threshold and mistaken as $^3\mathrm{He}(n,p)^3\mathrm{H}$ candidates (Fig. 6.19). The ratio of leakage is calculated by applying the $^3\mathrm{He}(n,p)^3\mathrm{H}$ selection cuts to the MC sample of neutron decay. By combining with the measured neutron decay events, the neutron decay contamination can be evaluated. The correction is inversely proportional to the amount of ^{3}He.

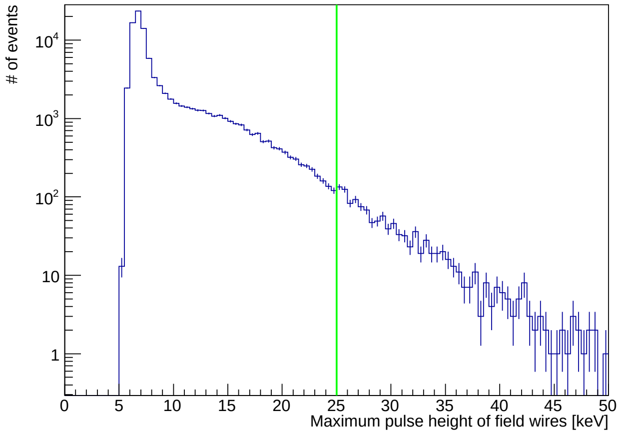

Figure 6.19: Maximum pulse heigh of the field wires in the neutron decay. The cut threshold is indicated with green line.

Pileup

A single event is recorded by TDC with the time window of 100 µsec, and multiple reactions would be detected by a certain probability. Since we calculate the dead time based on the number of triggers, signal events have to be counted similarly. For that reason, we define that when multiple reactions are detected in a single event, only the first one is counted. In this definition, we have to correct the events which were not triggered by $^3\mathrm{He}(n,p)^3\mathrm{H}$ reaction, and the possible combinations of the reactions are categorized as below.

(a) A background event followed by the $^3\mathrm{He}(n,p)^3\mathrm{H}$ reaction.

(b) Pileup of high energy backgrounds.

(c) Combinations of a high energy background and a neutron decay candidate.

The high energy backgrounds include ^{3}He$(n,p)^3$H reaction after neutron scattering and a portion of cosmic rays. (b) and (c) do not contain signal events and therefore account for only 0.0003 % of the ^{3}He$(n,p)^3$H candidates. Some of them might have been removed by previous procedures. Eventually, the correction is dominated by (a), result in about 0.07 % of the candidates.

^{14}N$(n,p)^{14}$C reaction

The measurements with low gain operation were conducted to estimate the contamination of ^{14}N. Low gain measurements were inserted about 4 times in each gas mixture. Figure 6.20 shows the energy deposit of the low gain measurement. The peak of ^{3}He (764 keV) and that of ^{14}N (626 keV) are fitted by double-gaussian function (blue), while another peak can be found in higher energy region, that includes ^{17}O$(n,\alpha)^{14}$C reaction and pileup of ^{3}He$(n,p)^3$H (red). Compared with ^{3}He, the amount of ^{14}N is obtained by using the ratio of the number of events and the capture cross sections. As shown in Fig. 6.21, the amount of ^{14}N at a certain time is calculated by interpolating the transition of the ratio. The contamination of ^{14}N$(n,p)^{14}$C reaction result in about a few percent of the ^{3}He$(n,p)^3$H candidates. Note that what affect to the uncertainty of the lifetime is the overlap of two peaks, that is taken as the statistical uncertainty of ^{14}N and not more than 0.1 %.

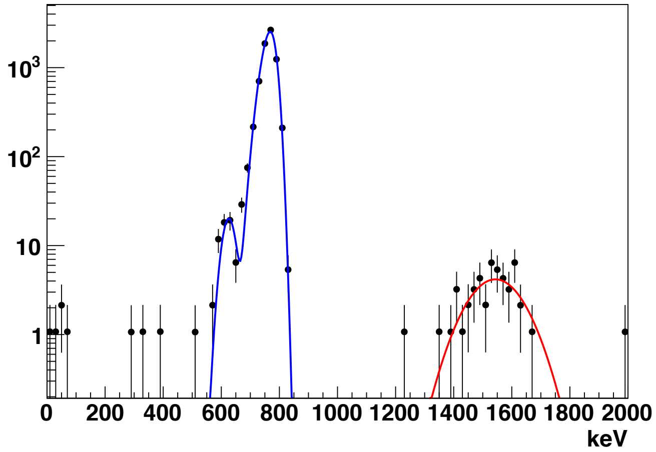

Figure 6.20: Energy deposit of the low gain measurement.

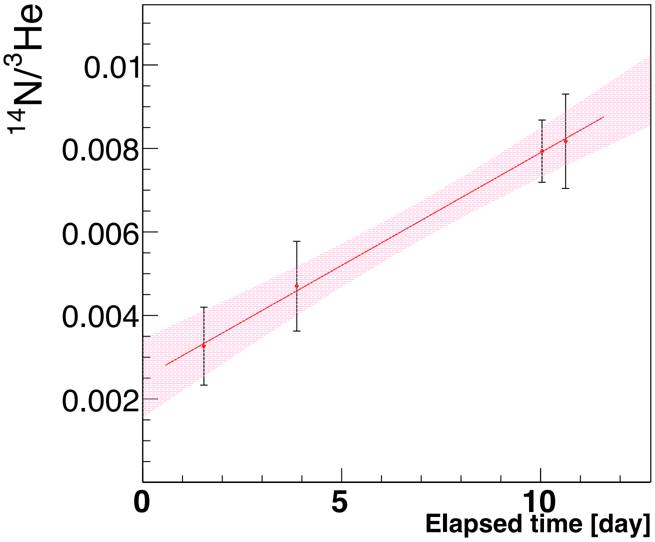

Figure 6.21: Transition of the ratio of neutron capture events, $^{14}N/^{3}He$.

$^{17}O(n,\alpha)^{14}C$ reaction

As it is indicated in Fig. 6.20, $^{17}O(n,\alpha)^{14}C$ reaction was observed with low gain operation. The energy deposit of the capture reaction is 1844 keV, that is about twice the energy deposit of $^{3}He(n,p)^{3}H$ reaction. We identified single tracks with such a high energy deposit and its rate agreed with the expectation. Thus we concluded the existence of $^{17}O(n,\alpha)^{14}C$ contamination and they were corrected by using the capture cross section (0.236 barn) and the natural abundance of ^{17}O in CO_2 gas (0.038 %). Under the condition of ^{4}He 85 kPa + CO_2 15 kPa, the partial pressure of ^{17}O is to be 11.4 Pa. The contribution of the correction accounts for about 0.5 %.

6.4.2 Corrections for the neutron decay candidates

The neutron decay candidates include followings.

- Neutron decay without neutron scattering (signal)
- Neutron decay after neutron scattering (background)
- (n, γ) reactions from the LiF tiles
- $^{3}He(n,p)^{3}H$
- Pileup of events

Gas induced backgrounds

Here we will deal with the backgrounds derived from neutron scattering. As mentioned in the previous section, the off-axis region is occupied by the backgrounds so that the identification of the starting point is also essential to count the neutron decay, and we introduce two parameters. One works as to separate the backgrounds and another indicates the starting point of the track. The former parameter, "XValue" is defined as the distance between the nearest hit anode wire to the beam axis. If a neutron was scattered to the off-axis region and its energy deposit was limited to there, it is easily eliminated by requiring XValue to be less than 3.

The latter parameter, "DC" is defined as the distance between the beam axis to the edge of the track which is closer to the beam axis. The definition of DC is illustrated in Fig. 6.22, viewing the xy plane of the TPC. The neutrons go through the center of TPC and three arrows indicate the electron tracks which start from red points. The center of TPC in x direction is shown as green dotted line. DC corresponds to the distance between the red point to the green line. The backgrounds are dominated by the ones derived from LiF tiles and they are more likely to take larger value of DC. Therefore, the signal-to-noise ratio can be improved by applying DC to be less than 3 (Fig.6.23). Since a unit length of XValue is made to be 12 mm and that is the same with DC, both of the regions, "XValue≤3" and "DC≤3", fully cover the beam cross section.

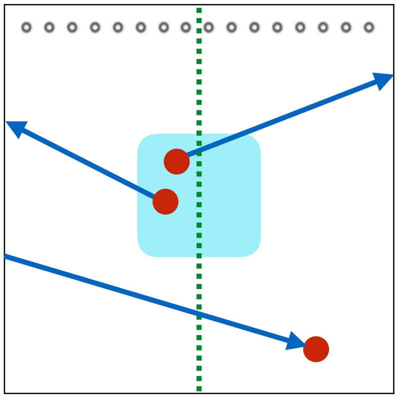

Figure 6.22: Drawing of the definition of DC. The TPC is viewed in xy plane and the electron tracks are illustrated as blue arrows. The red points and the green dotted line indicate the origin of the tracks and the beam axis.

The number of signal events have been estimated by using three kinds of MC samples, the signal neutron decay, the background neutron decay and the prompt γ rays from LiF tiles. Each MC sample is scaled so as to satisfy the following constraints.

- The total number of events of all MC samples are equal to that of data.
- In XValue>3, the sum of two background samples is equal to data.
- The ratio of the background neutron decay to the signal neutron decay is equal to the probability of scattering.

The probability of the neutron scattering have been calculated in the previous section. After subtracting the backgrounds from data, the number of signal events is obtained by applying the cut, DC$\leq$3.

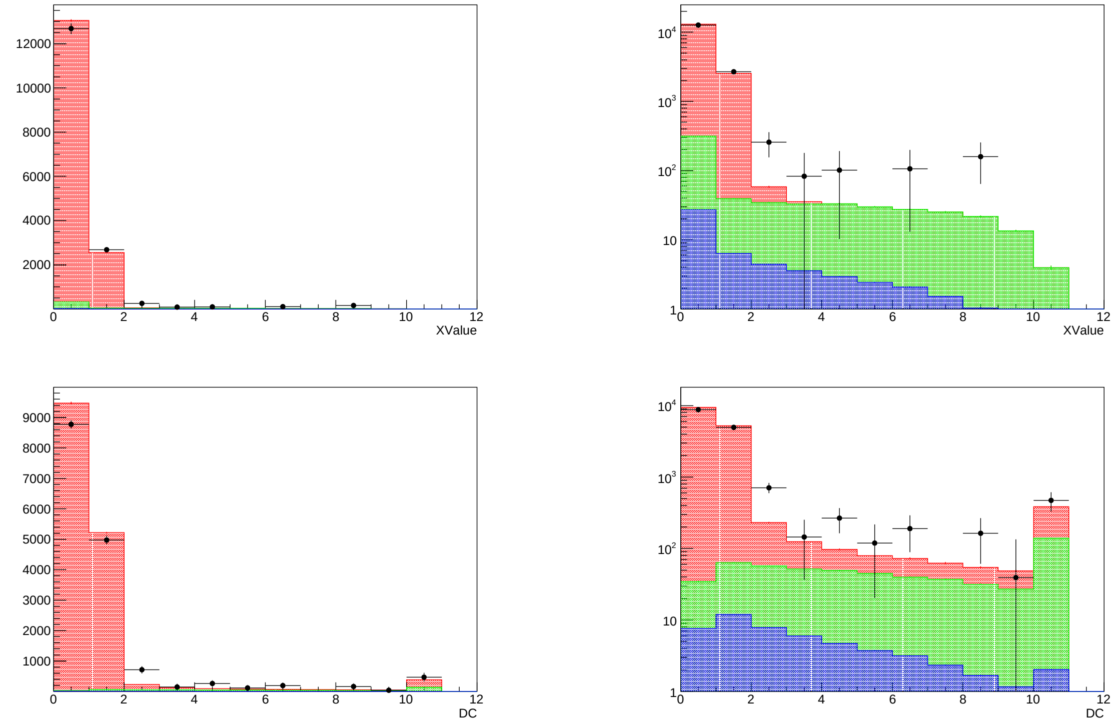

Figure 6.23: XValue (top) and DC (bottom) of the data and the MC samples. Red, green and blue histograms correspond to MC samples of the signal neutron decay, (n, γ) background and the neutron decay background followed with scattering. Each parameter is displayed with linear and logarithmic scale on the left and right.

^{3}He$(n,p)^3$H reaction

^{3}He$(n,p)^3$H reaction is rarely mistaken as neutron decay because we have adjusted the threshold to minimize the contamination and almost no correction is required. Figure 6.24 shows the distribution of the separation parameter.

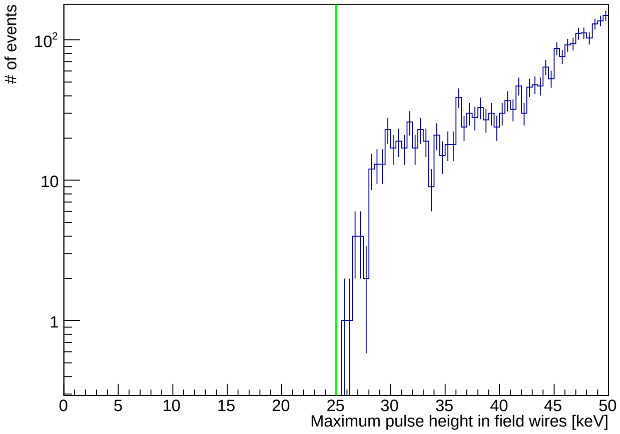

Figure 6.24: Maximum pulse heigh of the field wires in ^{3}He$(n,p)^3$H reaction. The cut threshold is indicated with green line.

Pileup

As it is the same with ^{3}He$(n,p)^3$H candidates, only the event which was triggered by the neutron decay have to be counted. Followings are the combinations of events to be corrected.

(A) A low energy background followed by signal neutron decay.

(B) Pileup of low energy backgrounds.

(C) Signal neutron decay followed by a ^{3}He$(n,p)^3$H candidate.

Low energy backgrounds are the events such as neutron decay after scattering, (n,γ) backgrounds in the LiF tiles, the neutron capture in CO_2 and cosmic ray. (C) should be counted as the neutron decay but previously categorized as ^{3}He$(n,p)^3$H candidates and have been removed in Sec. 6.4.1. That account for 0.2 % of the neutron decay candidates. In the case of (A), CO_2 is important background since it has high rate and less likely to be eliminated by detected with neutron decay. (B) have negligible influence, and finally correction of pileup result in 0.08 % of the neutron decay candidates.

6.5 Summary of the number of signal events

We have started first physics data taking in 2016. Combined with engineering data, we prepared six gas mixtures and accumulated 6.37×10^4 events of neutron decay (Tab. 6.2). The uncertainties of number of signal events were evaluated as summarized in Tabs. 6.3 and 6.4. The precision of the number of signal events is restricted by statistics of neutron decay. The systematical uncertainties of the neutron decay events have significance influence and mainly they are related with γ ray backgrounds, the neutron capture reaction in CO_2 and pileup of events.

Series	N_β	N_n
1	$8.5(3)\times10^3$	$2.436(6)\times10^5$
2	$8.5(2)\times10^3$	$2.003(6)\times10^5$
3	$3.6(2)\times10^3$	$9.47(3)\times10^4$
4	$1.49(4)\times10^4$	$6.92(1)\times10^5$
5	$1.38(4)\times10^4$	$1.810(5)\times10^5$
6	$1.44(4)\times10^4$	$3.580(7)\times10^5$
Total	$6.37(8)\times10^4$	$1.770(3)\times10^6$

Table 6.2: Number of signal events.

Series	1	2	3	4	5	6
Systematical errors						
Neutron decay contamination	0.03	0.05	0.03	0.02	0.08	0.05
Pileup	0.08	0.11	0.07	0.07	0.07	0.07
$^{14}N(n,p)^{14}C$ contamination	0.047	0.066	0.076	0.019	0.12	0.060
$^{17}O(n,\alpha)^{14}C$ contamination	0.025	0.028	0.026	0.014	0.050	0.026
Subtotal	0.10	0.14	0.11	0.08	0.16	0.11
Statistical error of data	0.21	0.24	0.34	0.13	0.25	0.18
Total	0.23	0.28	0.36	0.15	0.30	0.21

Table 6.3: Uncertainties of the number of $^3He(n,p)^3H$ events in percentage.

Series	1	2	3	4	5	6
Systematical errors						
LiF shutter condition	1.3	0.12	0.12	0.59	0.43	0.33
γ spectrum of LiF tile	0.23	0.024	0.22	0.065	0.16	0.037
Pileup	0.29	0.45	0.19	0.35	0.10	0.18
CO_2 contamination	0.27	0.25	0.30	0.23	0.30	0.27
^{3}He contamination	0.06	0.05	0.00	0.00	0.01	0.00
S/N of SFC	0.020	0.016	0.026	0.051	0.017	0.022
Subtotal	1.3	0.5	0.4	0.7	0.6	0.5
Statistical error of data	2.7	2.2	5.1	2.5	2.6	2.6
Total	3.0	2.2	5.1	2.6	2.7	2.6

Table 6.4: Uncertainties of the number of neutron decay events in percentage.

Chapter 7

Efficiency

7.1 Evaluation of signal efficiency

Signal efficiency is evaluated by applying the cuts to the MC samples. In this process, we have to take care of followings.

- The uncertainty of each cut parameter has to be estimated correctly.
- Considering the uncertainty of the parameter, threshold should be set within small fluctuation of efficiency to keep the precision of evaluation.
- Suppression of the statistical error is also critical role of the cuts.

Followings are the cuts introduced in chapter 6.

Cut	Source of uncertainty
Noise suppression	Negligible
Fiducial TOF	Negligible
Signal separation	Energy calibration
Cosmic ray suppression	Drift velocity
Discrimination of energy deposit	Energy calibration
^{3}H suppression	Deviation of ph/int
On-axis track selection	Beam distribution

Table 7.1: Cuts for the neutron decay.

Cut	Source of uncertainty
Noise suppression	Negligible
Fiducial TOF	Negligible
Signal separation	Energy calibration

Table 7.2: Cuts for the ${}^3\text{He}(n,p){}^3\text{H}$ reaction.

7.2 Uncertainties of the cut parameters

At first, we will deal with the sources of uncertainties in cut parameters, these are the drift velocity, the energy calibration, deviation of ph/int and reproducibility of beam distribution.

Drift velocity

It was found out that the drift velocity depends on the position in y direction. That would be caused by non-uniformity of the electrical field, and generate large uncertainty of drift length. In order to measure the position dependence, the absolute y positions of the ionized particles were determined as it is explained in Sec. 3.8, and the result is shown in Fig. 7.1. The velocity standard is equal to the velocity at the center of TPC, and the maximum deviation is given when ionized particles drift from distant position. The uncertainty of drift velocity was estimated to be less than 10 %. Therefore, the loose threshold was applied to suppress the ambiguity in the cut efficiency.

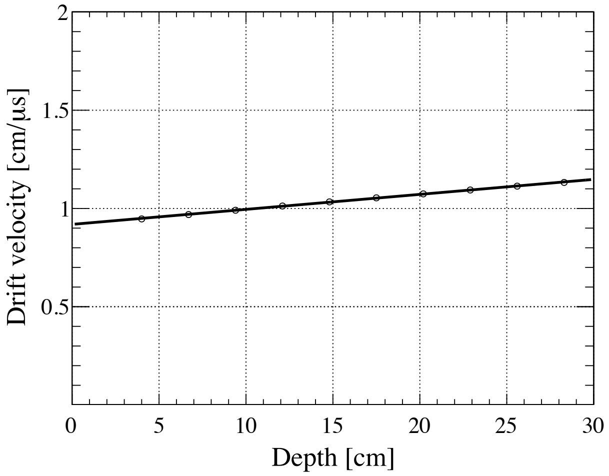

Figure 7.1: Drift velocity vs. y position, measured with cosmic ray events.

Energy calibration

As it is explained in Sec. 3.7, energy deposit is calibrated by using the X-ray source. There are two possible reasons which lower the precision of calibration. One is the position of energy deposit. If ionized particles have been generated in a distant place from standard y position, the uncertainty of the energy calibration would be enlarged. Another thing is the transition of the gain due to increasing of outgas. If the vacuum condition is bad, the gain will be immediately lowered and outgas enhance the position dependence of energy calibration over time. The reproducibility of energy calibration is estimated by comparing data and the MC sample of cosmic ray for the most probable value of energy deposit (Fig. 7.2). The uncertainty of energy calibration resulted in $5\sim9\,\%$.

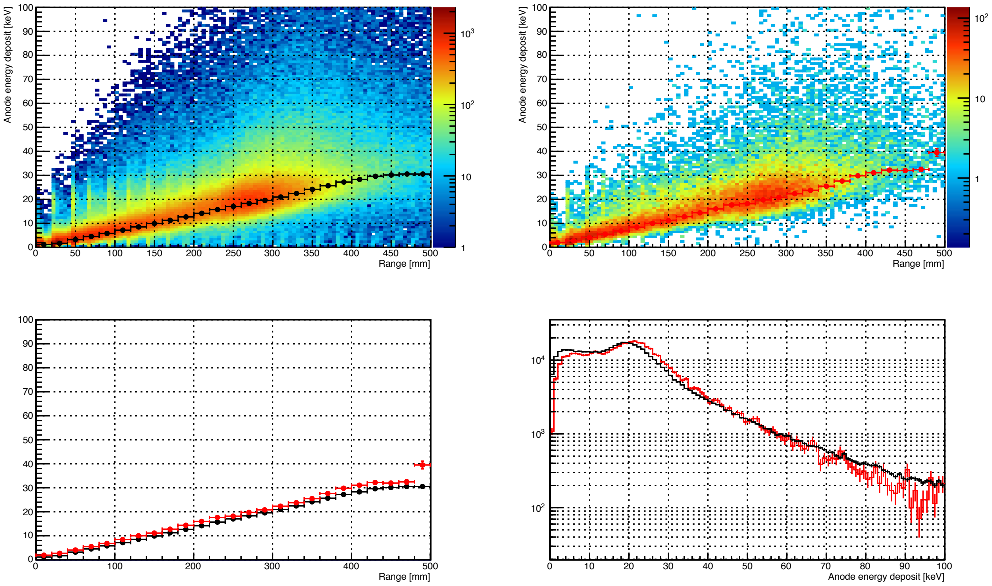

Figure 7.2: Comparison of data and MC sample of cosmic ray. Energy deposit vs. track length of data (top left) and that of MC sample (top right). The track length of data (black) and MC sample (red) are shown in bottom left, and the energy deposit of data (black) and MC sample (red) are shown in bottom right.

Deviation of ph/int

The ph/int works to remove the event which have low energy deposit ($< 15\,\mathrm{keV}$) and the waveform is similar to the template. In the case of photoelectric events generated by X-ray from the calibration source, the energy deposit is 5.9 keV and they are suitable for evaluating the ambiguity of ph/int. The uncertainty of ph/int was evaluated from the standard deviation of the X-ray events, resulted in 0.033 which correspond to 4 % of the uncertainty of the threshold.

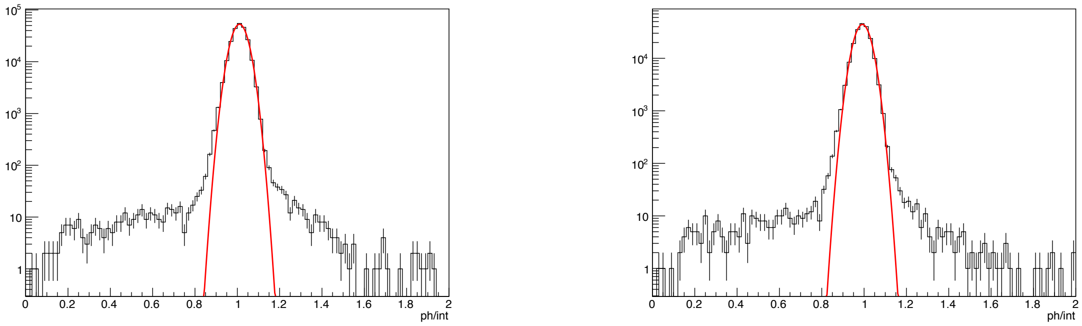

Figure 7.3: Deviation of ph/int measured with the X-ray source positioned $y = 75\,\mathrm{mm}$ (left) and $y = \text{-}75\,\mathrm{mm}$ (right).

Reproducibility of the beam distribution

To reproduce the beam distribution, another measurement was conducted and the data was input to the MC simulation (see appendix B). We consider two possible sources of uncertainties, one is the resolution of detector and another is the precision of detector alignment. Each uncertainty is estimated to be 1 mm in x direction and we concluded that the irreproducibility of the beam distribution is not more than 2 mm.

7.3 Uncertainties of cut efficiencies

Based on the ambiguities of parameters, the thresholds were determined to minimize the statistical errors and the systematical errors. Except for the parameter "DC", the systematical errors arise from cuts are estimated by the fluctuation of the cut efficiencies. The performance of the cuts are shown in Figs 7.4 $\sim$ 7.9. The uncertainties of the parameters are indicated with yellow bands and the thresholds are shown with green lines.

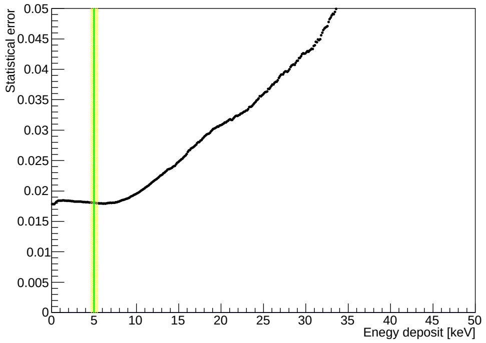

Figure 7.4: Statistical error vs. Anode energy deposit.

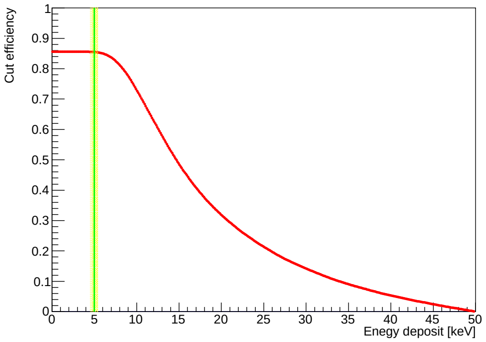

Figure 7.5: Cut efficiency vs. Anode energy deposit.

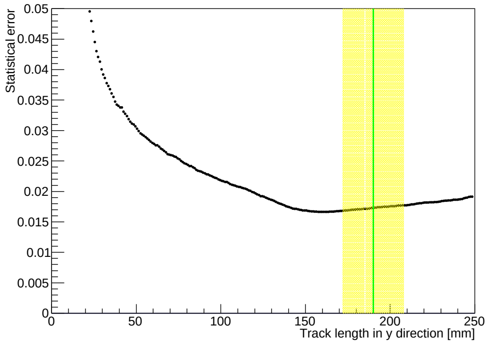

Figure 7.6: Statistical error vs. Drift length.

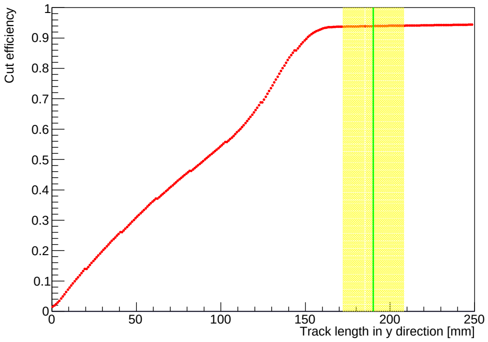

Figure 7.7: Cut efficiency vs. Drift length.

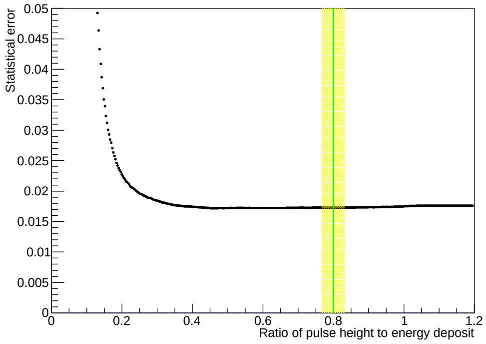

Figure 7.8: Statistical error vs. ph/int.

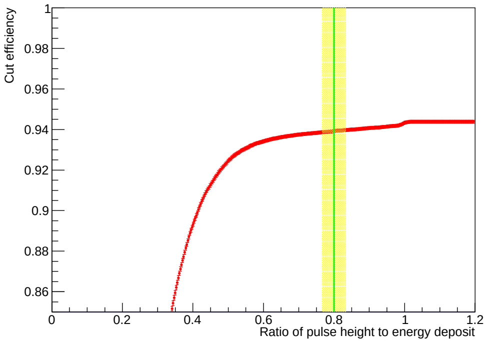

Figure 7.9: Cut efficiency vs. ph/int.

In order to estimate the uncertainty derived from DC, MC simulation was re-weighted to shift the beam distribution in x direction by 2 mm (Fig.7.10). We calculate the neutron decay candidates with and without shifting the beam distribution and the uncertainty of cut efficiency is obtained by the difference of the number of candidates. The threshold of DC is sufficiently outside of the beam crossing, therefore the uncertainty of the cut efficiency resulted in not more than 0.03 %.

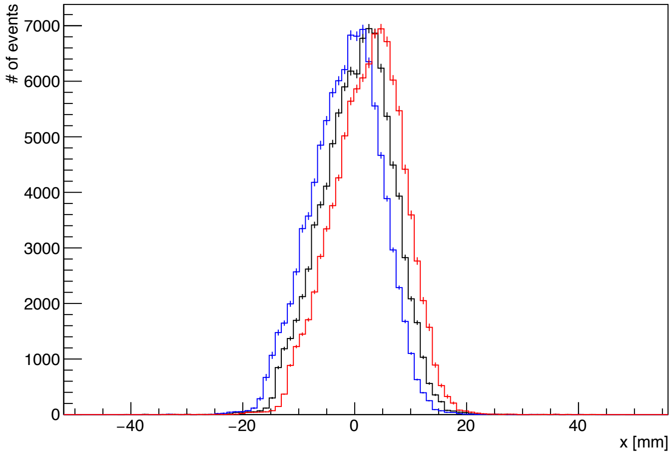

Figure 7.10: Beam distribution in x direction. Each histogram represents the original distribution (black), shifted by +2 mm (red) and shifted by -2 mm (blue).

7.4 Summary of efficiency

The uncertainties of efficiency is summarized in Tabs. 7.4 and 7.5. In addition to the uncertainties explained in the previous section, the effect of neutron polarization and W-value are included. The largest error is generated by the separation of neutron decay and $^3\mathrm{He}(n,p)^3\mathrm{H}$ reaction. The amount of energy deposit is the only parameter used to separate the candidates, therefore the systematical error is originated from energy calibration. The separation could be improved by adopting additional parameters such as length or shape of the track.

The estimation of number of signal events depends on the identification of the origin of the track, the ambiguity of efficiency is avoided by loose threshold. Further, lower limit of the energy deposit is set to suppress the neutron capture reactions in CO_2, and the uncertainty is not remarkable because the threshold is set within small fluctuation of the efficiency. As for the evaluation of $^3\mathrm{He}(n,p)^3\mathrm{H}$ reaction, we have achieved high efficiency of almost 100 %, besides its uncertainty is less than 0.01 %.

Series	ϵ_β [%]	ϵ_n [%]
1	94.1(6)	99.986(4)
2	94.2(5)	99.997(4)
3	94.3(5)	99.978(6)
4	94.0(6)	99.987(4)
5	94.1(9)	99.995(13)
6	93.9(8)	99.999(8)

Table 7.3: Efficiencies of signals.

Series	1	2	3	4	5	6
Statistic of MC	0.08	0.08	0.08	0.08	0.08	0.08
Signal separation	0.45	0.31	0.88	0.57	0.88	0.74
Cosmic ray suppresion	0.18	0.18	0.19	0.18	0.20	0.17
Discrimination of energy deposit	0.07	0.07	0.16	0.12	0.18	0.16
^{3}H suppression	0.05	0.05	0.07	0.05	0.05	0.06
On-axis track selection	0.09	0.02	0.12	0.04	0.02	0.03
Neutron polarization	0.13	0.13	0.13	0.13	0.13	0.13
W-value	0.35	0.35	0.35	0.35	0.35	0.35
Total	0.63	0.53	1.00	0.72	0.97	0.87

Table 7.4: Uncertainties of the efficiency of neutron decay in percentage.

Series	1	2	3	4	5	6
Statistic of MC	0.004	0.002	0.005	0.004	0.002	0.001
Signal separation	0.000	0.004	0.004	0.000	0.013	0.008
Total	0.004	0.004	0.006	0.004	0.013	0.008

Table 7.5: Uncertainties of the efficiency of ^{3}He$(n,p)^3$H reaction in percentage.

Part IV

Conclusion

Chapter 8

Conclusion and future prospects

Precise measurement of the neutron lifetime is the key to increase the accuracy of the prediction of Big Bang cosmology and the light nuclei production in the early universe, since the neutron lifetime has direct influence to determine the relative abundance of primordial helium and also the time scale of thermal equilibrium of the weak interactions.

We measured the neutron lifetime with accelerator based neutron beam at J-PARC. A distinctive feature of our experiment is the low level background condition that have been achieved by originally developed TPC and SFC. Radioactive backgrounds and neutron correlated backgrounds are mitigated with material selection of the drift cage. SFC is the new optical device to switch the neutron beam and is able to adjust the length of neutron bunches, that much contribute to discriminate prompt γ rays produced in the upstream. In addition, our approach is different from the bottle experiments in the point of view of systematical uncertainty since neutron decay is counted by detecting the electron.

In 2014 and 2015, engineering data was taken so as to establish the analytic method. Our first physics data have been taken in 2016, and the blind analysis was performed to avoid the possibility of biasing. Physics data is combined with engineering data and accumulated data correspond to 12 days of data acquisition at averaged beam power of 170 kW. We present our first result of measurement as below.

$$\tau_n = 899 \pm 10\,(\text{stat.}) \pm^{9}_{11}\,(\text{syst.})\,\text{sec} \;\; (\text{Combined})$$

Series	Beam power [kW]	DAQ [day]	τ_n [sec]
1 (May 2014)	240	1.4	$952 \pm 26\,(\text{stat.}) \pm^{15}_{15}\,(\text{syst.})$
2 (Apr. 2015)	430	0.7	$908 \pm 20\,(\text{stat.}) \pm^{8}_{7}\,(\text{syst.})$
3 (Apr. 2016)	170	0.8	$901 \pm 46\,(\text{stat.}) \pm^{8}_{11}\,(\text{syst.})$
4 (Apr. 2016)	170	3.0	$890 \pm 22\,(\text{stat.}) \pm^{9}_{10}\,(\text{syst.})$
5 (May 2016)	170	2.8	$881 \pm 24\,(\text{stat.}) \pm^{9}_{12}\,(\text{syst.})$
6 (Jun. 2016)	160	3.0	$870 \pm 23\,(\text{stat.}) \pm^{8}_{10}\,(\text{syst.})$

Table 8.1: Summary of the results of the neutron lifetime measurement.

The backgrounds originated from neutron interactions were studied in detail and they were removed by data driven approach, as much as possible. MC simulation was used to estimate the efficiency and the backgrounds induced by neutron scattering. In order to reconstruct the measurement, we conducted additional measurements as described in appendix B and C, and the results were input to the simulation. In addition, uncertainties in cut efficiency were avoided by applying the loose threshold.

Statistical and systematical errors account for about 1 % respectively, and systematical errors are summarized in Tab. 8.2. It is practically possible to improve the statistical accuracy by long-term operation at 500 kW. Besides, we have plans to upgrade the setup and that is explained in the latter part of this chapter.

Systematical errors can be classified into (a) ones that can be reduced by increasing the statistics of data, (b) another would be decreased by statistics of simulation, (c) others have to be measured more precisely, and (d) the others are improved by making advances on analytic methods. In the following, we explain how to reduce systematical errors with examples.

(a) Statistics of data
In the estimation of number of signal events, uncertainties are derived from the backgrounds, such as $^{14}\mathrm{N}(n,p)^{14}\mathrm{C}$ and pileup. The uncertainties in these corrections are governed by the measurement of event rate, therefore they can be reduced when statistics are increased. We have the upgrade plan to increase the beam flux.

(b) Statistics of simulation
Important uncertainties are derived from γ ray and are dominated by the statistics of simulation, because γ ray have low probability of interaction. The uncertainties would be reduced by increasing the statistics of simulation and improvement in analysis is also substantial.

(c) Cross sections of neutron capture reactions
Since the number of neutron capture reactions in ^{3}He and $\mathrm{CO_2}$ were calculated by

using the capture cross sections, the uncertainties were determined by the precision of cross sections and they have to be measured more precisely.

(d) Methods of analyses
There are still room for improvement in analytic methods. For example, the largest influence to the uncertainty of cut efficiency is generated by the separation of the neutron decay and $^3\mathrm{He}(n,p)^3\mathrm{H}$ reaction. Separation is performed by using only the energy deposit and that would be improved by introducing a parameter to enhance topological differences of the tracks. The other important uncertainties are originated from γ rays and they would be effectively discriminated by identifying the starting point of the decay electron in z direction.

Series	1	2	3	4	5	6
N_β	1.3	0.5	0.4	0.7	0.6	0.5
N_n	0.10	0.14	0.11	0.08	0.16	0.11
ϵ_β	0.63	0.53	1.00	0.72	0.97	0.87
ϵ_n	0.004	0.004	0.006	0.004	0.013	0.008
ρ	0.6	0.5	0.4	0.5	0.7	0.5
σ_0	0.13	0.13	0.13	0.13	0.13	0.13

Table 8.2: Systematical errors of the neutron lifetime in percentage.

8.1 Upgrade plans

As the future prospects, we have plans to improve the precision of measurement. One is to operate with lower gas pressure, that is effective for reducing the neutron induced backgrounds, and another is the enlargement of the setup to increase the beam flux.

Operation of TPC with lower gas pressure to reduce neutron induced backgrounds

Some of the backgrounds were caused by neutron scattering and the contamination account for a few percent of the neutron decay events. In order to avoid the ambiguity of simulation and to perform the measurement with data driven approach, the probability of scattering has to be reduced and we have been studying the performance of TPC operated with decreased pressure. While we have reported the measurement with 100 kPa in this thesis, another configuration of 50 kPa have been demonstrated and the measured probability of scattering is roughly proportional to the gas pressure.

For the practical operation, mainly we have two problems to be solved. One is heat generation of the preamplifiers, that would locally increase the temperature around the preamplifiers. As the result, the uncertainty would be generated by the non-uniformity of ^{3}He gas density. We have been developing a new preamplifier with higher gain and lower heat generation. Another problem is the reduction of detection efficiency, since MWPC has to be operated with lower voltage to avoid an electric discharge. On the other hand, we observed the reduction of the effect of attenuation. The drift velocity become 1.5 times faster and that contribute to reduce chances of interactions with gases. Besides, that might help to conduct longer operation with a gas filling.

Modification of SFC and collimators to increase the neutron beam intensity

In the present experimental setup, we can achieve the statistical accuracy of below 0.1 % by accumulating data correspond to 100 days at 1 MW operation, while the upgrade of the setup is planed to move forward. Firstly, larger collimaters and larger mirrors of SFC are designed to expand the beam cross section, because there are losses of neutron due to small acceptance of the setup. Secondly, TPC is also enlarged to adopt the larger beam cross section.

	Present	Upgrade plan
Collimater		
B_4C collimater size [mm^2]	40 × 40	100 × 30
LiF collimater size [mm^2]	25 × 20	100 × 30
Mirror		
Mirror size [mm^3]	140 × 30 × 0.7	200 × 100 × 0.3
Number of 1st and 2nd mirrors	5	8
Number of 3rd mirror	5	10

Table 8.3: Upgrade plans of the setup. B_4C collimater and LiF collimater are positioned 1185 mm and 1570 mm downstream of the target.

The improvement of the beam flux have been estimated by using PHITS simulation, and the result is shown in Tab. 8.4 and Fig. 8.1. When enlarged collimaters and mirrors are adopted, we expect to obtain 23.5 times higher beam flux and the statistical accuracy of on order of 0.1 % will be achieved by 5 days of DAQ time at the 500 kW operation.

	Beam flux [neutron/s·MW]
Present	$5.96(29) \times 10^6$
Enlarged mirrors	$1.49(05) \times 10^7$
Enlarged mirrors and collimaters	$1.40(02) \times 10^8$

Table 8.4: Upgrade plans and expected beam flux.

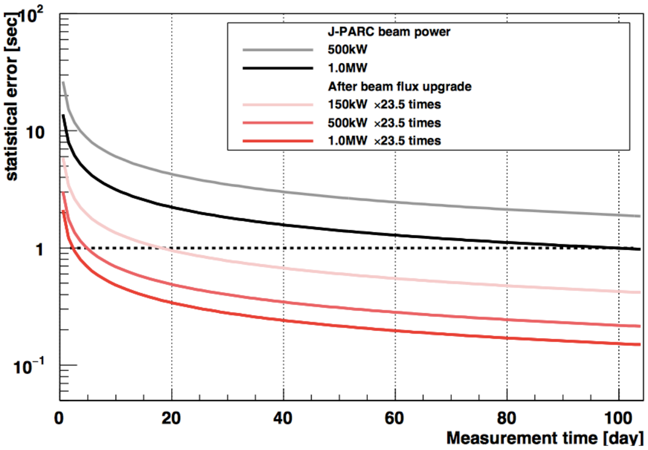

Figure 8.1: Improvement of the statistical error.

Appendix A

Radiative neutron decay

Radiative neutron decay shares second largest branching ratio among the decay modes of neutron. Depend on the way of bremsstrahlung, three kinds of Feynman diagrams are possible as shown in Fig. A.1.

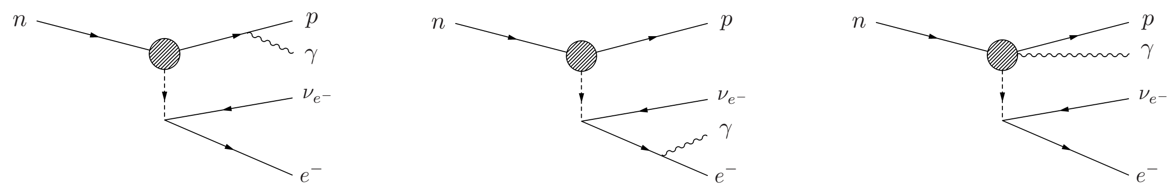

Figure A.1: Feynman diagrams of radiative neutron decay. The electron bremsstrahlung (left), the proton bremsstrahlung (center) and bremsstrahlung from weak vertex (right).

Each branching ratio is determined by the photon energy, in other words, the ratio is determined by the energy of the electron and that of the proton. The leading order is the electron bremsstrahlung and the proton bremsstrahlung, while the former is dominant because of the mass difference ($m_e \ll m_p$). The influence of radiative decay appears in the radiative correction of the CKM matrix element, V_{ud}.

Appendix B

Beam structure

To reconstruct beam structure is an important issue because our estimation of the number of signal events rely on finding the origin of the track. We conducted the measurement of the beam structure by using RPMT, which is a two dimensional detector and also possible to measure the TOF. And the efficiency of RPMT was measured at the low-divergence beam branch.

B.1 RPMT

A helium filled beam monitor is widely used to measure the neutron flux since it has high detection efficiency of neutron but lack of position sensitively. In the measurement of beam structure, RPMT is used to obtain positional resolution, while the beam monitor is used to refer the beam flux. RPMT consists of a position-sensitive PMT (PSPMT), a neutron scintillator and readout system. The schematic of setup is illustrated in Fig. B.1. The scintillator was put on the PSPMT without using grease between the optical contact of the PMT and the scintillator. Because the scintillator includes ^{6}Li, the α particle is emitted as the result of $^6\mathrm{Li}(n,\alpha)^3\mathrm{H}$ reaction. Besides, the scintillator contains ZnS so that scintillation light is generated by α particle and that is detected after amplified with a 12-stage dynode.

Anode wires are crossed in x and y directions and the current is read out from both ends of wires. The current of each anode wire is divided into I_1 and I_2 by resisters. Eventually, four signal lines of X_1, X_2, Y_1 and Y_2 are read out and the position of incident neutron is reconstructed by the ratio of current, $I_1/(I_1 + I_2)$.

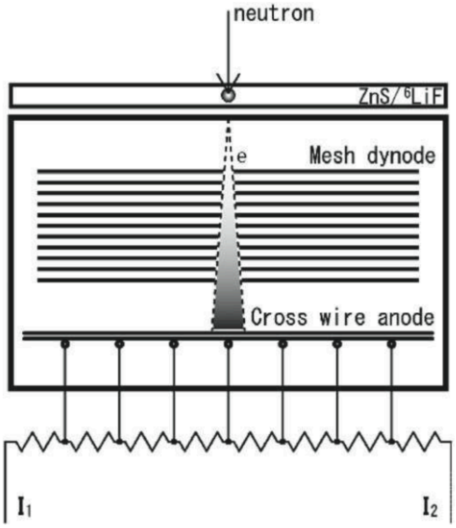

Figure B.1: Schematic diagram of RPMT [52].

PSPMT	
Diameter [mm]	127
Spacial resolution [mm]	0.5 ∼ 0.8
Effective area [mm^2]	60 × 60
Scintillator	
Material	ZnS(Ag)/^{6}LiF
Thickness [mm]	0.25
Light yield [photons/n]	$> 10^4$

Table B.1: Specification of the RPMT [52, 53].

B.2 Measurement of the efficiency of RPMT

The position dependence of detection efficiency was measured at the low-divergence beam branch. The setup is shown in Figs. B.2 and B.3. The beam monitor was fixed at the exit of the low-divergence beam branch and the neutron beam was collimated by using $2 \times 2\,\mathrm{mm}^2$ cadmium foil to avoid saturation of RPMT. Just behind the slit, the RPMT was fixed on the XY stage and the stage was moved so as to scan the RPMT surface. The alignment of RPMT and beam monitor is better than 1 mm and that is small enough compared with the spacing of the anode wires of MWPC. Although, the detection efficiency depend on position of hit and the neutron velocity, it was not yet corrected in the Fig. 5.2.

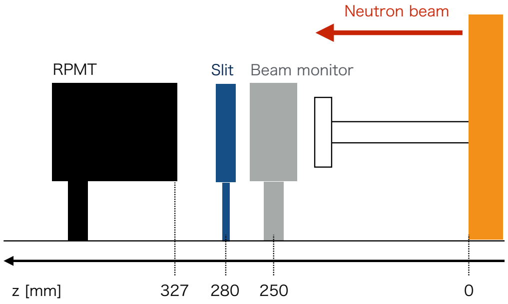

Figure B.2: Illustration of the side view of the setup for the measurement of RPMT efficiency.

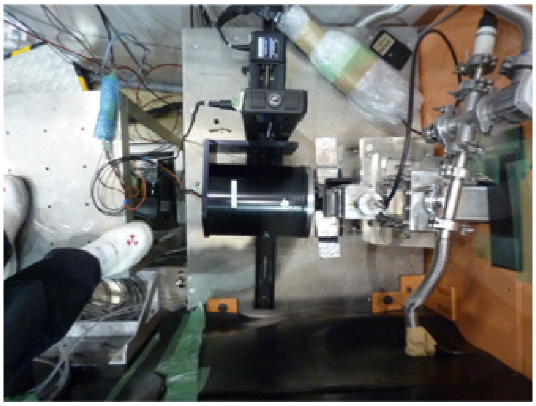

Figure B.3: Top view of the setup for the measurement of RPMT efficiency.

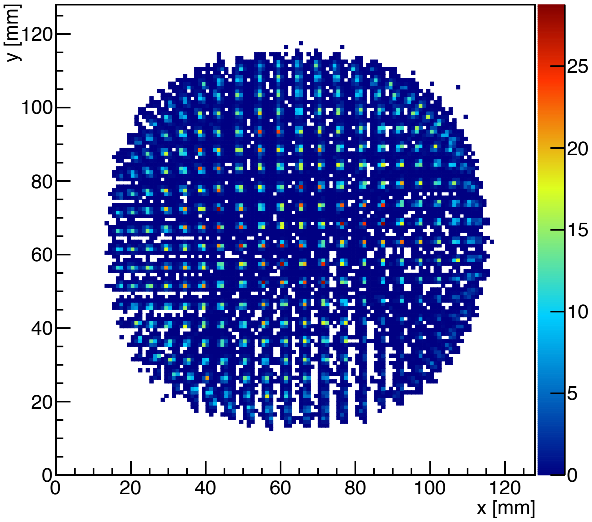

Figure B.4: Efficiency of the RPMT.

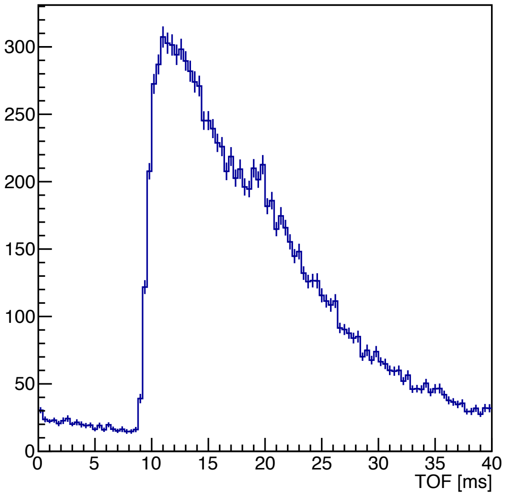

Figure B.5: TOF spectrum measured with the RPMT.

B.3 Measurement of the beam structure

In the measurement of the beam structure, the RPMT was moved to the polarization beam branch and set inside the aluminum vessel (Fig. B.6). It should be noted that measurement was performed without vacuuming because the RPMT can not be used in such a condition. The light receiving face of the RPMT was positioned 8.5 cm downstream from the edge of TPC. In this measurement, the RPMT was not moved but the slit was moved with XY stage to scan whole surface of the exit of SFC. The result of measurement is given in Fig. 5.2.

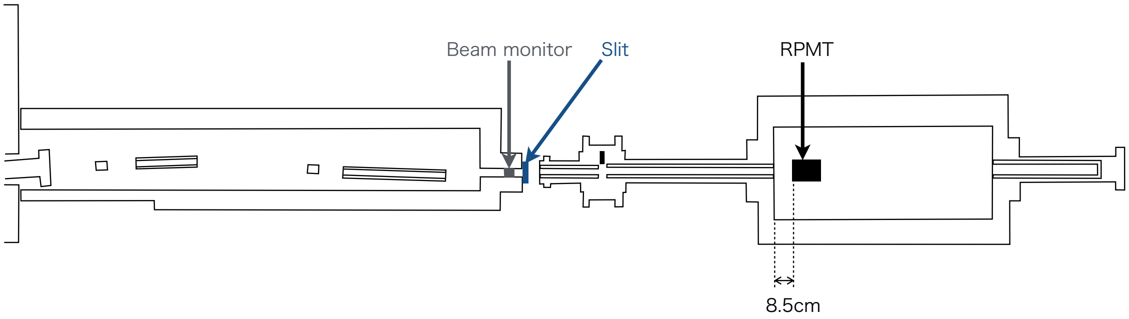

Figure B.6: Setup of the measurement of the beam structure.

Appendix C

γ ray spectrum of LiF tile

The energy spectrum of γ rays from the LiF tile was measured at beamline 04 (ANNRI). The measurement was conducted to reconstruct (n, γ) events and the result was input to MC simulation.

C.1 Measurement of γ ray spectrum

ANNRI is the experimental facility with Ge detector array and is possible to measure neutron capture cross section accurately. The detail of experiment can be found in [54–56]. The schematic view of the setup is given in Figs. C.1 and C.2. The neutrons are moderated with coupled hydrogen moderator and go through the T0 chopper, neutron filter, disk choppers and collimators. The sample and Ge spectrometer are placed at 21.5 m downstream of the moderator.

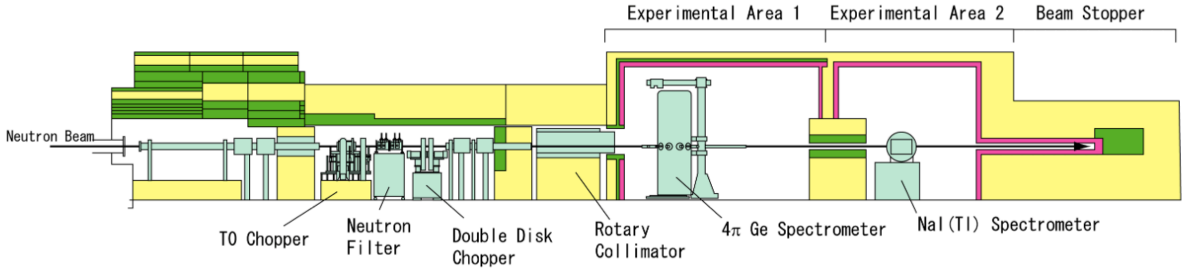

Figure C.1: Size view of the beamline 04 [56]. The neutron beam goes through the T0 chopper, neutron filter, disk choppers and collimators.

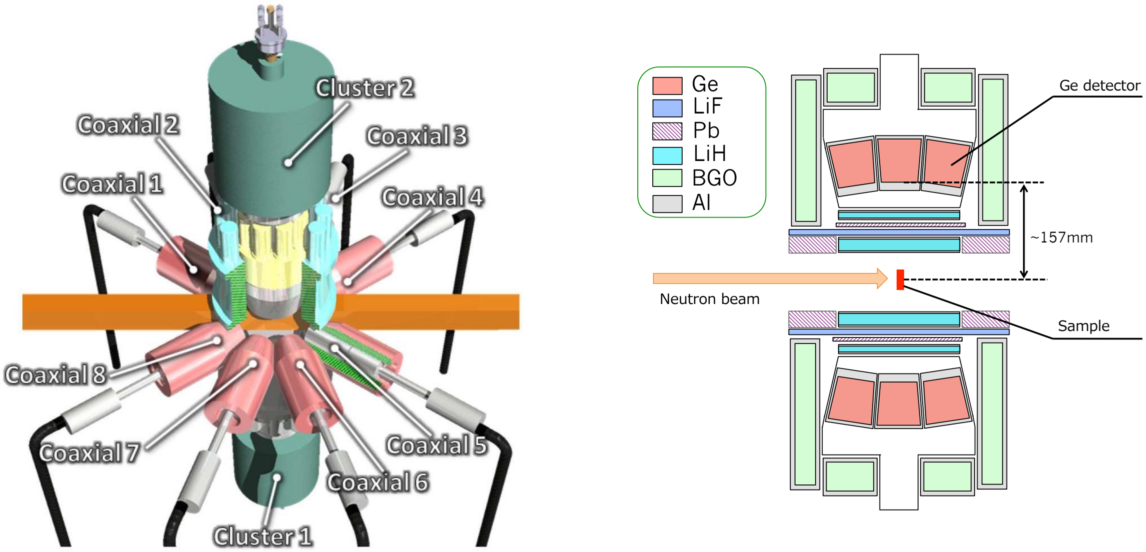

Figure C.2: Schematic diagram of Ge spectrometer [56]. A sample is set in the center of the Ge detectors. Coaxial-Ge detectors are shown in red and cluster-Ge detectors are shown in light blue.

The LiF tile which is actually installed to our TPC was brought to ANNRI and the tile was irradiated with the neutron beam. The energy spectrum of γ rays was measured by cluster-Ge detectors which were viewing the tile from top and bottom. TOF was also obtained in the measurement. There are coaxial-Ge detectors surrounding the sample but they were not used in the measurement. The specification of Ge detector is given in Tab. C.1.

Cluster-Ge detector	2×7 ch
Coaxial-Ge detector	8 ch
Energy resolution (at 1.33 MeV)	2.5 keV
Peak efficiency (at 1.33 MeV)	3.64×0.11 %

Table C.1: Specification of the Ge detector.

C.2 Reconstruction of the intensity of γ rays

The measurements were performed with and without setting the LiF tile, and the observed γ ray spectra are shown in Fig. C.3. In the reconstruction of the γ ray energy spectrum, the MC samples which include detector energy resolution were used. At first, the spectrum which was measured without the LiF tile was subtracted from the one measured with the LiF tile. Then, we estimated the intensity of each peak from one with higher energy. Each MC sample was scaled to conform the area of the peak with $5\,\sigma$, and removed from data. This procedure was repeated until all peaks were to be subtracted. In $^{19}\mathrm{F}(n,\gamma)$ reaction, some peaks were too small to estimate so that the relative intensity was calculated based on the reference value, and one of the intense peak of 1387 keV was employed as the standard. The detected spectrum was reconstructed as shown in Fig. C.4. Finally, we obtained intensity of γ rays emitted from the LiF tile, that is given in Fig. 5.4.

It should be noted that there were two unexpected peaks found at 140 keV and 198 keV. According to the level of scheme, the γ ray with such energy would not be emitted from the component of the LiF tile. In the case of peak with 198 keV, the lifetime was estimated to be about 20.4 ms and we concluded that the γ ray was derived from ^{71}Ge. On the other hand, we also analyzed the TOF of another peak and found that it was not prompt γ ray. Because the time structure of the background is different from that of signal events, the background does not matter to the evaluation of signal events.

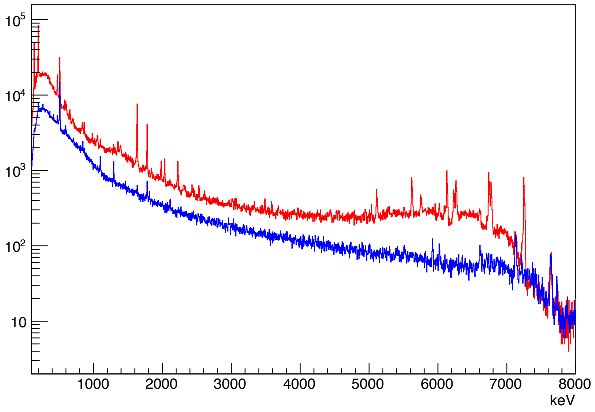

Figure C.3: Energy spectrum of γ rays measured with LiF tile (red) and without LiF tile (blue).

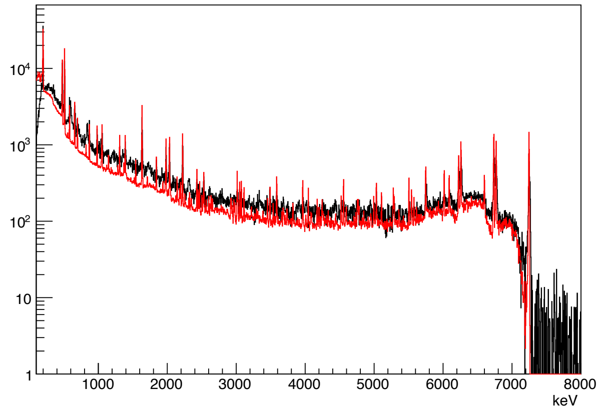

Figure C.4: Energy spectrum of γ rays of the data after subtracting the background (black) and the reconstructed spectrum by using MC samples (red).

Appendix D

Mass spectrometry

We use G1He gas which is the commercial product by Tomoe shokai Co., Ltd. and mainly consist of ^{4}He. In order to determine ^{3}He density precisely, we have to take into account the isotopic contamination of ^{3}He in G1He. The helium isotopic ratio (^{3}He/^{4}He) was measured by using mass spectrometry and the total amount of ^{3}He introduced to the TPC was corrected.

D.1 Noble gas analyzing system

After data acquisition have been finished, the TPC gas was sampled from the valve at the downstream of aluminum vessel and the measurement of ^{3}He/^{4}He ratio with mass spectrometry was conducted with cooperation of isotope geochemistry and cosmochemistry laboratory, at the University of Tokyo. The mass spectrometer has double collector system and it can determine the ^{3}He/^{4}He ratio with a precision of $\pm$ 10 % under the condition of partial pressure of ^{3}He in the range of 0.5 to 5×10^{-14} Torr.

The noble gas analyzing system consist of gas extraction part, gas purification part, separation part and mass spectrometry part. The measurement is performed as below. Firstly, the gas sample is introduced from the left side of the Fig. D.1 and purification proceed by using Ti-Zr getters (Ti1 and Ti2) and charcoal traps (CH1 and CH2). In this process, released noble gases such as argon, krypton and xenon are adsorbed by CH1. While helium and neon are purified with Ti2, CH2 and a SORB-AC getter pump. Then, neon is separated by a cryogenically cooled trap (Cryo-trap) and helium is guided into the modified-VG(5400) to measure the ^{3}He/^{4}He ratio.

In the mass spectrometry part, both of ^{3}He beam and ^{4}He beam are measured simultaneously. Figure D.2 shows the picture of the setup. The ion beams are bended in the passage of the magnetic field, where the radius of curvature depend on the mass to charge ratio. Finally, ^{3}He beam and ^{4}He beam are detected by the ion-counting system and the High-Faraday cup, seperately.

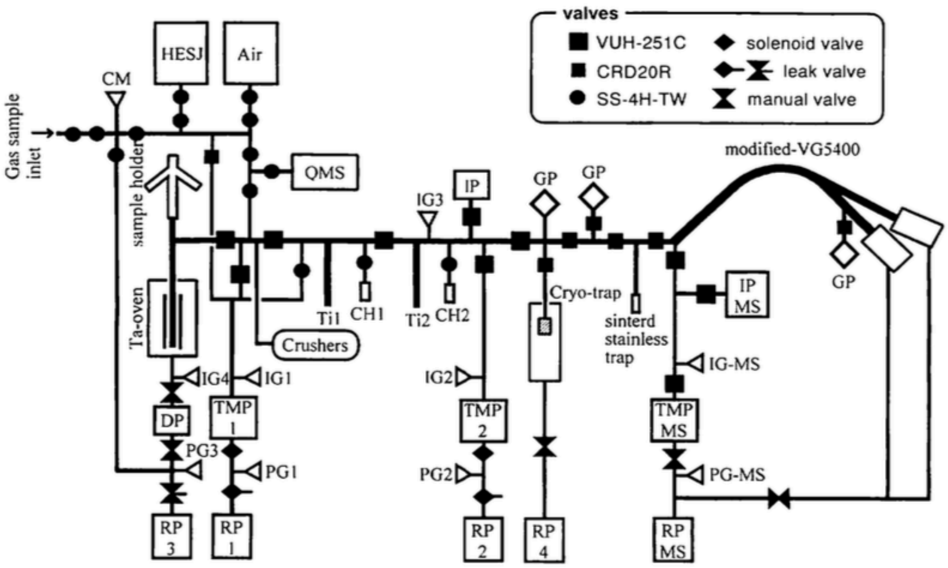

Figure D.1: Schematic diagram of the noble gas analyzing system [57].

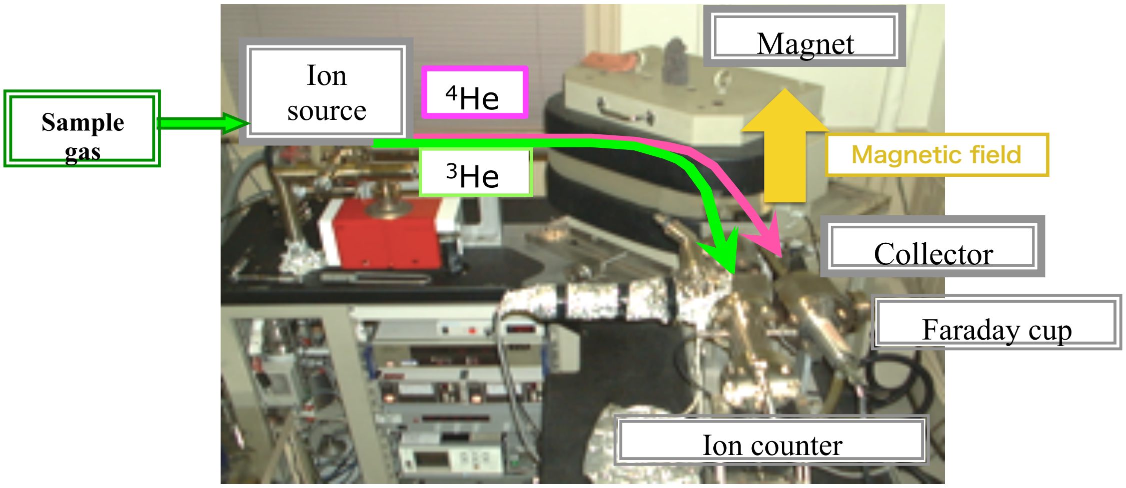

Figure D.2: Setup of the mass spectrometry.

In order to determine the absolute ratio of ^{3}He/^{4}He, a standard helium gas with well known isotopic ratio is needed. Historically, atmospheric helium has been used as a primary standard but it is not preferable because its ^{3}He/^{4}He ratio would be changed, and large amount of gas have to be introduced to the measurement system due to low density of ^{3}He in the air.

An artificial gas mixture named HESJ (He Standard of Japan) was prepared to be used as an internal standard of ^{3}He/^{4}He ratio and we adopted HESJ in the measurement [58]. The sample gas and HESJ were measured alternately. Finally, the ^{3}He/^{4}He ratio of the sample was determined as it is summarized in Tab. D.1. According to the result, ^{3}He density was corrected in Sec. 3.5.1.

Bottle#	Series	G1He/HESJ ($\times 10^{-3}$)
6	1	3.21(7)
7	2, 3, 4	4.05(6)
8	5, 6	3.70(11)

Table D.1: Ratio of ^{3}He/^{4}He of G1He to that of HESJ.

Acknowledgements

I would like to thank all the people who supported me throughout the years of after graduated. This work could not be accomplished without anyone's help.

First of all, I wish to express great appreciation to my supervisor, Satoru Yamashita, who always give me critical advices and initiate the way to find the issues to be addressed. I think I could have been working on because he kindly respected my opinion and increase my eagerness to study more. Many things that I have learned from him were not limited in experimental physics and that really help me in my daily life. I am glad to be a member of Yamashita group.

I would like to thank Kenji Mishima, for the great contribution to practical work and informative discussions. He have been engaging in not only the conduction of the experiment but also data analysis, therefore our experiment would not progress without him. It is hard to conclude the discussions even if our collaboration is not so large, and I would like to thank Masaaki Kitaguchi who encourage active and approachable discussions. When I suggested new things, he always discussed with patience to reach the best conclusions.

I would like take this opportunity to express my sincere gratitude to Hirohiko M. Shimizu, Takashi Ino, Hirochika Sumino, Yoshihisa Iwashita, Tamaki Yoshioka, Katsuya Hirota, Tatsusi Shima, Daiichiro Sekiba, Kaoru Taketani, Yoshichika Seki, and all those who have continuously supported for the construction of apparatuses, commissioning and all of works to conduct NOP experiment.

I would like to send many thanks to Takahito Yamada who has substantial contribution to the development of data acquisition system. He gave me a lot of knowledge concerning computing and gas chamber physics, and enthusiastically guided me. During the work in Tokai, I worked with many colleagues and I often worked with Tatsuhiko Tomita. Since I was the later student to join NOP experiment, he politely answers my questions and helped me with conducting the measurement. Besides, I thank him for his friendly atmosphere that relieve me so much. I would like to thank Ryuunosuke Kitahara who taught me about SPC and the analysis of ^{14}N background in detail. I am grateful to Naoki Nagakura and Naoyuki Sumi. I learned many things from fruitful discussions and I believe each of them will play a vital role in the next measurement. Concerning with the upgrade of the setup, Mami Yokohashi and Aya Morishita played important roles. They made strenuous efforts in the designing of the setup and simulation studies, and that encouraged me a lot. I also

worked with Jun Koga and Hideaki Uehara, who are thoughtful and attentive students. It was very fun to have dinner together and I hope to work with them in the future.

I especially would like to thank the member of Yamashita group, Tomohiko Tanabe, Masakazu Kurata, Takuro Murase, Ryo Katayama, Nao Higashi, Harumichi Yokoyama, Takuaki Mori, Kento Kasuya, Shohei Fujikura, Yu Kato and Kazuki Fujii. And also, I really appreciate Hidetoshi Otono and Hideyuki Oide who have been great mentors to me. Their contributions are indispensable for not only this work but also the development of the basis of another work. Although they had already graduated when I joined Yamashita group, they gave me a lot of advices from far away and my framework of studying have been constructed based on their previous works.

I would like to express appreciation to ICEPP secretaries and the members of the user's office at J-PARC, who supported me with managements.

Special thanks are to all of those whose names are not written but enriched my life in various aspects and shared precious time outside the laboratory.

Finally, I really thank my parents, my sister and my brothers.

List of Figures

List of Tables

Bibliography

[1] J. Chadwick, Proc. Roy. Soc. A, 136, (1932) 692-708

[2] J. Chadwick and M. Goldhaber, Nature 134, (1934) 237

[3] R. L. Cooper *et al.*, Phys. Rev. C 81, (2010) 035503

[4] NIST, Neutron scattering lengths and cross sections, `https://www.ncnr.nist.gov/resources/n-lengths/`

[5] Particle Data Group, `http://pdg.lbl.gov`

[6] R. Kossakowski *et al.*, Nucl. Phys. A503 (1989) 473-500

[7] K. Schreckenbach and W. Mampe, J. Phys. G, Nucl. and Part. Phys., Vol. 18, (1992) 1-34

[8] J. S. Nico *et al.*, J. Phys. G, Nucl. Part. Phys. 36 (2009) 104001

[9] S. Burles *et al.*, Phys. Rev. Lett. Vol. 82, (1999) 4176-4179

[10] R. E. Lopez *et al.*, Phys. Rev. D, Vol. 59, (1999) 103502

[11] Stephan Paul, The Puzzle of Neutron Lifetime and How to Solve It, `https://www.ill.eu/fileadmin/users_files/documents/news_and_events/workshops_events/slow_neutron/pdf_2008/20080529_1_1_Paul.pdf`

[12] Hartmut Abele and Daniela Mund, Mattes-Verlag, Heidelberg, (2003) arXiv:hep-ph/0312124

[13] J. Nico, "Neutron Lifetime Measurement", `http://neutron.physics.ncsu.edu/SummerSchool/Nico.pdf`

[14] I. S. Towner and J. C. Hardy, J. Phys. G., Nucl. Part. Phys. 29 (2003) 197-211

[15] P. K. Kabir, Phys. Lett. Vol. 24B, (1967) 601-602

[16] E. Fermi and L. Marshall, Phys. Rev. Vol. 71, No.10, (1947) 666-677

[17] C. D. Keith, Phys. Rev. C 69, (2004) 034005

[18] J. S. Nico *et al.*, Phys. Rev. C 71, (2005) 055502

[19] G. Steinhauser *et al.*, Performance and comparison of gold-based neutron flux monitors, Gold Bulletin, Vol. 45, (2012) 17-22

[20] A. Serebrov *et al.*, Phys. Rev. C 78, (2008) 035505

[21] F. Anton *et al.*, Nucl. Instr. Meth. in Phys. Research A 284, (1989) 101-107

[22] K. J. Kugler *et al.*, Nucl. Instr. Meth. in Phys. Research 228 (1985) 240-258

[23] W. Mampe *et al.*, JETP Lett., Vol. 57, No. 2, (1993) 82-87

[24] J. Byrne *et al.*, Europhysics Letters, Vol. 33, No. 3, (1996)

[25] A. Serebrov *et al.*, Phys. Lett. B 605, (2005) 72

[26] A. T. Yue *et al.*, Phys. Rev. Lett. 111, (2013) 222501

[27] A. Pichlmaier *et al.*, Phys. Lett. B 693, (2010) 221

[28] A. Steyerl *et al.*, Phys. Rev. C 85, (2012) 065503

[29] S. Arzumanov *et al.*, Phys. Lett. B 745, (2015) 79-89

[30] J-PARC, `http://j-parc.jp/index-e.html`

[31] Y. Arimoto *et al.*, Prog. Theor. Exp. Phys., (2012) 02B007

[32] T. Ino *et al.*, J. Phys. Conference Series 528 (2014) 012039

[33] T. Ino *et al.*, Physica B 406 (2011) 2424-2428

[34] Y. Seki *et al.*, J. Phys. Soc. Jpn. 79, (2010) 124201

[35] F. Sauli, Principles of Operation of Multiwire Proportional and Drift Chambers, CERN-77-09 (1977)

[36] Y. Arimoto *et al.*, Nucl. Instr. Meth. A 799 (2015) 187

[37] Y. Igarashi *et al.*, IEEE Trans. Nucl. Sci. 52 (2005) 2866-2871

[38] N. Z. Alcock *et al.*, Phys. Rev. 83 (1951) 1100

[39] N. Z. Alcock and D. G. Hurst. Neutron diffraction by gases. Phys. Rev., 75:1609-1610, May 1949.

[40] H. Cohen and W. S.Diethorn, phys. stat. sol. 9, (1965) 251

[41] Hj. Matzke, phys. stat. sol. 18, (1966) 317

[42] S. Agostinelli *et al.*, Nucl. Instr. and Meth. A 506 (2003) 250-303

[43] D. Mancusi *et al.*, Phys. Rev. C 90 (2014) 054602

[44] H. Otono, New detector system for the precise neutron lifetime measurement using pulsed cold neutron beams, University of Tokyo, 2011, Ph.D. thesis.

[45] E. Waibel and B. Grosswendt, Nucl. Instr. Meth. in Phys. Research B53 (1991) 239-250

[46] ANSYS, Theory reference,
`http://research.me.udel.edu/~lwang/teaching/MEx81/ansys56manual.pdf`

[47] Rob Veenhof, Garfield - simulation of gaseous detectors,
`http://garfield.web.cern.ch/garfield`

[48] PHITS, `https://phits.jaea.go.jp/indexj.html`

[49] W. Shockley, Currents to conductors induced by a moving point charge, Journal of Applied Physics, Vol. 9, (1938) 635-636

[50] Yasojima Proceed Co., Ltd., Properties of PEEK,
`http://www.yasojima.co.jp/en/zairyo/peek/pdf/peek.pdf`

[51] B. W. Sleaford *et al.*, Journal of the Korean Physical Society, Vol. 59, No.2, (2011) pp. 1473-1478

[52] Katsuya Hirota *et al.*, Phys. Chem. Chem. Phys. 7, (2005) 1836-1838

[53] Hamamatsu Photonics K.K.,
`http://www.hamamatsu.com/resources/pdf/etd/R2486_TPMH1206E.pdf`

[54] M. Igashira *et al.*, Nucl. Instr. Meth. A 600 (2009) 332-334

[55] K. Kino *et al.*, Nucl. Instr. Meth. A 626-627, (2011) 56-66

[56] A. Kimura *et al.*, J. Nucl. Science and Technology, Vol. 49, No. 7, (2012) 708-724

[57] H. Sumino *et al.*, J. Mass Spectrom. Soc. Jpn., Vol. 49, No.2, (2001) 61-68

[58] J. Matsuda *et al.*, Geochemical J., Vol. 36, (2002) 191-195